

2013

# Domain coarsening and interface kinetics in the Ising model

---

<https://hdl.handle.net/2144/16815>

*Downloaded from DSpace Repository, DSpace Institution's institutional repository*

BOSTON UNIVERSITY  
GRADUATE SCHOOL OF ARTS AND SCIENCES

Dissertation

**DOMAIN COARSENING AND INTERFACE KINETICS  
IN THE ISING MODEL**

by

**JASON WILLIAM OLEJARZ**

B.S., University of Massachusetts at Dartmouth, 2008

M.A., Boston University, 2011

Submitted in partial fulfillment of the  
requirements for the degree of  
Doctor of Philosophy

2013

© 2013 by  
Jason William Olejarz  
All rights reserved

Approved by

First Reader

---

Sidney Redner, Ph.D.  
Professor of Physics

Second Reader

---

Anders Sandvik, Ph.D.  
Professor of Physics

*For My Father*

# Acknowledgments

I'd like to thank my thesis advisor, Sid Redner, for creating a phenomenal research environment, for allowing me great freedom in developing my dissertation project, and for providing insightful advice and outstanding training along the way. I'm also appreciative of my close collaborator, Paul Krapivsky, for many stimulating discussions, for fascinating research ideas, and for constant encouragement.

I am indebted to Boston University and to UMass Dartmouth for giving me a chance to develop as a physicist. I am also grateful to the National Science Foundation for financially supporting this work.

Most importantly, I thank my family and friends. Without their strong help and unwavering support, this work would not have been possible.

**DOMAIN COARSENING AND INTERFACE KINETICS**  
**IN THE ISING MODEL**

(Order No.                      )

**JASON WILLIAM OLEJARZ**

Boston University Graduate School of Arts and Sciences, 2013

Major Professor: Sidney Redner, Professor of Physics

**ABSTRACT**

In this thesis, I investigate in detail two basic problems in nonequilibrium statistical mechanics. First, if a spin system such as a kinetic Ising model or a kinetic Potts model is quenched from supercritical temperature to subcritical temperature, how does the system coarsen, and what complexities arise as the system descends in energy toward one of its equilibrium states? Second, if a kinetic Ising model is evolved from a deterministic initial condition at zero temperature, how do the domain interfaces evolve in time?

I first study the nonconserved coarsening of the kinetic spin systems mentioned above. The coarsening of a  $2d$  ferromagnet can be described exactly by an intriguing connection with continuum critical percolation. Furthermore, careful simulations of phase ordering in the  $3d$  Ising model at zero temperature reveal strange nonstatic final states and anomalously slow relaxation modes, which we explain in detail. I find similarly rich phenomena in the zero-temperature evolution of a kinetic Potts model in  $2d$ , where glassy behavior is again manifest. We also find large-scale avalanches in which clusters merge and dramatically expand beyond their original convex hulls at late times in the dynamics.

Next, I study the geometrically simpler problem of the evolution of a single corner interface in the Ising model. We extend prior work by investigating the Ising Hamiltonian with longer interaction range. We solve exactly the limiting shapes of the corner interface in  $2d$  for several interaction ranges. In  $3d$ , where analytical treatments are notoriously

difficult, we develop novel methods for studying corner interface growth. I conjecture a growth equation for the interface that agrees quite well with simulation data, and I discuss the interface's surprising geometrical features.

In the summary, I discuss the broader implications of our findings and offer some thoughts on possible directions for future work.



# Contents

<b>1</b>	<b>Introduction</b>	<b>1</b>
1.1	Phase-Ordering Kinetics . . . . .	2
1.2	Kinetic Ising Model and its Variants . . . . .	2
1.3	Time-Dependent Ginzburg-Landau Theory . . . . .	6
1.4	Current Research . . . . .	9
<b>2</b>	<b>Universality of Two-Dimensional Curvature-Driven Coarsening</b>	<b>13</b>
2.1	Predictions from Percolation Theory . . . . .	14
2.2	Stripe States in Models that Exhibit Nonconserved Coarsening . . . . .	16
2.2.1	Simulation Results . . . . .	20
2.3	Stability of Topologies . . . . .	21
2.4	Discussion . . . . .	24
<b>3</b>	<b>Freezing in Three-Dimensional Ising Ferromagnets</b>	<b>26</b>
3.1	Quench of a Three-Dimensional Kinetic Ising Model to $T = 0$ . . . . .	28
3.1.1	Final State Geometry . . . . .	30
3.1.2	Blinker States . . . . .	36
3.1.3	Ultra-Slow Relaxation . . . . .	38
3.1.4	Effects of the Initial Condition . . . . .	44
3.1.5	Non-Cubic Geometries . . . . .	45
3.2	Quench of a Three-Dimensional Kinetic Ising Model to $T > 0$ : The Approach to Equilibrium . . . . .	45

3.2.1	Stage I: Coarsening . . . . .	47
3.2.2	Stage II: Plumber’s Nightmare . . . . .	48
3.2.3	Stage III: Slab State . . . . .	50
3.2.4	Stage IV: Equilibrium . . . . .	51
3.3	Time-Dependent Ginzburg-Landau Coarsening in Three Dimensions . . . . .	52
3.4	Discussion . . . . .	54
<b>4</b>	<b>Zero-Temperature Freezing in the Two-Dimensional Potts Model</b>	<b>56</b>
4.1	Nonsymmetric Initial Condition . . . . .	58
4.2	The Long-Time State . . . . .	60
4.2.1	Blinker States . . . . .	64
4.2.2	Pseudo-Blinker States . . . . .	65
4.2.3	Cluster “Avalanches” at Late Times . . . . .	66
4.3	Reaching the Ground State . . . . .	70
4.4	A Time-Dependent Ginzburg-Landau Description of Multi-State Coarsening	72
4.5	Discussion . . . . .	76
<b>5</b>	<b>Two-Dimensional Interface Growth with Nearest-Neighbor and Longer-Range Ising Interactions</b>	<b>78</b>
5.1	Standard Ising Interactions . . . . .	79
5.2	Long-Range Ising Interactions . . . . .	81
5.3	Biased Motion . . . . .	85
5.4	Discussion . . . . .	91
<b>6</b>	<b>Three-Dimensional Interface Growth Inside a Corner</b>	<b>92</b>
6.1	The Model . . . . .	92
6.2	Conjectural Governing Equation for Growth in Three Dimensions . . . . .	94
6.2.1	Simulation Results . . . . .	96
6.3	Alternate Evolution Equations and Extensions to Higher Dimensions . . . . .	104

6.4	Geometrical Characteristics of the Interface . . . . .	109
6.5	Discussion . . . . .	110
<b>7</b>	<b>Concluding Remarks</b>	<b>114</b>
	<b>Appendices</b>	<b>117</b>
<b>A</b>	<b>Acceleration Algorithm for the Zero-Temperature <math>3d</math> KIM</b>	<b>118</b>
<b>B</b>	<b>The <math>3d</math> KIM: Small Systems, Number of Clusters, Blinker States</b>	<b>120</b>
	<b>Bibliography</b>	<b>122</b>
	<b>Curriculum Vitae</b>	<b>134</b>

# List of Tables

A.1	Average final energies $E_L$ for different cutoff times $\tau$ and system sizes $L$ . . .	119
B.1	The nine possible paths to the final state for an $L = 2$ system, starting from the antiferromagnetic state. . . . .	121
B.2	Probability of reaching a ground state $P_g$ , a frozen state $P_f$ , or a blinker state $P_b$ versus $L$ following a quench from the antiferromagnetic initial state.	121
B.3	Probability of reaching a state with one cluster, two clusters, three clusters, or greater than three clusters versus $L$ following a quench from the antiferromagnetic initial state. . . . .	121

# List of Figures

1.1	The one-dimensional Ising model. . . . .	3
1.2	Coarsening in the two-dimensional Ising model using single-spin-flip dynamics at zero temperature. The competition between the two phases leads to nontrivial long-time states. The system size is $L \times L$ , with $L = 256$ . . . . .	5
1.3	(a) A circular domain of one phase in a background of the opposite phase. (b) A wedge-shaped domain. . . . .	8
2.1	Formation of a (1,1) diagonal stripe (top) and a (2,1) diagonal stripe (bottom) in the $2d$ Ising model quenched to zero temperature. The system size is $L \times L$ , with $L = 1024$ . . . . .	19
2.2	Probabilities of coarsening into a (1,0) stripe on a square, a (1,1) stripe on a square, a (2,1) stripe on a square, and a (2,1) stripe on a rectangle with aspect ratio $r = 2$ (top to bottom). For each case, the probabilities for the Ising model with NN interactions (black circles), the Ising model with NNN interactions (red diamonds), and the TDGL equation (blue triangles) are shown. For simulations of the KIM, $3.2 \times 10^6$ realizations were used for $L = 16, 32, 64$ , and $128$ , and $3.2 \times 10^5$ realizations were used for $L = 256$ . For simulations of the TDGL equation, $10^6$ realizations were used for $L = 16, 32, 64$ , and $128$ , and $5 \times 10^5$ realizations were used for $L = 256$ . . . . .	22
2.3	Survival probability $S(t)$ for an $L = 64$ KIM with only NN interactions (solid/black, $10^5$ realizations) and for NN and NNN interactions (dashed/red, $10^6$ realizations). . . . .	23

3.1	Time dependence of the energy for a single realization of an $L = 20$ system quenched to $T = 0$ . While the system settles into its final state at $t \approx 41712$ , it features drops in energy at surprisingly late times (inset). Note that the abscissa of the inset is $\ln t$ . . . . .	31
3.2	Configuration average of the time $\Delta t_n$ between successive energy drops as a function of $t_n$ , the average time at which the $n^{\text{th}}$ such energy drop occurred, for 1024 realizations of a $10 \times 10 \times 10$ system. The data are smoothed over a 100-point range. . . . .	31
3.3	Examples of low-genus ( $g = 3$ ) and high-genus ( $g = 16$ ) domains on a $20^3$ lattice. . . . .	32
3.4	Simple examples of interfaces with genus $g = 2$ and $g = 3$ for a periodic $2 \times 2 \times 2$ system. . . . .	33
3.5	The final-state energy (a) and genus (b) distributions for $L = 54$ ( $\circ$ ), $L = 76$ ( $\triangle$ ), and $L = 90$ ( $\nabla$ ). . . . .	35
3.6	A sample portion of a domain interface showing vertices of degrees 3, 4, 5, and 6. . . . .	36
3.7	An $8^3$ blinker on a $20^3$ cubic lattice, showing the fully-deflated state (left), an intermediate state (middle), and the fully-inflated state (right). The bounding slabs wrap periodically in the three Cartesian directions. . . . .	37
3.8	Example of a blinker state on a $20^3$ lattice with periodic boundaries. The highlighted blocks indicate blinker spins. . . . .	39
3.9	(left image) Survival probability $S(t)$ versus time $t$ . Data is based on $10^7$ realizations for $L = 4, 6, 8$ , and $10$ , 10240 realizations for $L = 14, 20$ , and $30$ , and 2048 realizations for $L = 40$ (lower left to upper right). (right image) $S(t)$ vs. $\ln t$ for $L = 20, 30$ , and $40$ (lower left to upper right) on a double logarithmic scale. The data is reasonably fit by the inverse logarithmic dependence Eq. (3.4). . . . .	41

3.10	First-passage time for a fully-deflated blinker to reach the fully-inflated state in two ( $\circ$ ) and three ( $\Delta$ ) dimensions. The fit to the two-dimensional data is $\tau_2 = 1.40 \exp(1.33 \ell)$ . The curve overlaying the three-dimensional data, $\tau_3 = 3 \exp(0.8 \ell^2)$ , is a guide for the eye. . . . .	43
3.11	Two-dimensional analog of the blinker states in Fig. 3.7. . . . .	44
3.12	Schematic two-dimensional illustration of a blinker coalescence event. . . . .	44
3.13	The final-state magnetization (a) and energy (b) distributions for $L = 32$ using antiferromagnetic and random initial conditions. The two initial conditions seem to produce different distributions of observables, even in the $L \rightarrow \infty$ limit. . . . .	45
3.14	Example long-time states of a $32 \times 32 \times 8$ system (left), a $32 \times 32 \times 32$ system (center), and a $32 \times 8 \times 8$ system (right). . . . .	46
3.15	A genus $g = 10$ sponge-like topology at time $t = 1024$ for a quench of an $L = 32$ system to $T = T_C/8$ . We ran this realization until the energy first reached the numerically-measured equilibrium value of energy for this system size and temperature. This realization reached equilibrium at time $t \approx 10^5$ —roughly two orders of magnitude longer than the coarsening time. . . . .	48
3.16	Energy versus time for three independent realizations of a quench to $T = T_C/8$ for a $32^3$ system. Energy is scaled so that the antiferromagnetic state energy is equal to 1, and the ground state energy is equal to 0. . . . .	50
3.17	A two-arm state evaporating in the $3d$ KIM at finite temperature. . . . .	51
3.18	$N(t)$ , $S(t)$ , and $T(t)$ for a quench of a $32^3$ system to $T = T_C/8$ . The data are obtained by averaging over $10^4$ realizations. . . . .	52

3.19	(left) Example of two roughly $16 \times 32^2$ slabs on a $32^3$ lattice following a quench of a KIM to $T = T_C/8$ . (right) Probability of getting trapped in a slab state for the Ising-Glauber ( $\circ$ ) and TDGL ( $\triangle$ ) systems. The KIM data is based on $10^6$ realizations for $L = 16, 22$ , and $32$ , $5 \times 10^5$ realizations for $L = 46$ , and $10^5$ realizations for $L = 64$ . The TDGL data is based on 1576000 realizations for $L = 16$ , 424000 realizations for $L = 22$ , 287000 realizations for $L = 32$ , 67000 realizations for $L = 46$ , and 7040 realizations for $L = 64$ .	53
3.20	Examples of coarsening in two independent realizations of the evolution of the $3d$ TDGL equation. In both cases, the system size is $L = 32$ . . . . .	54
3.21	A honeycomb-shaped cluster on a hexagonal lattice that is trivially frozen at $T = 0$ . . . . .	55
4.1	Probability for a 3-state Potts model with two species initially in the majority to coarsen into a horizontal/vertical (left) or diagonal (right) stripe topology.	59
4.2	An $L = 768$ Potts model coarsening into a blue-green stripe state with red initially slightly in the minority ( $\epsilon = 1/96$ ). . . . .	59
4.3	Typical outcomes for the $q = 3$ (top), $q = 4$ (middle), and $q = 6$ (bottom) Potts models after being quenched to zero temperature. The number of clusters in the final state typically increases as $q$ increases. . . . .	61
4.4	A T-junction, where three spin domains meet at right angles, is stable at zero temperature. . . . .	62
4.5	Energy versus time for $q = 3, 4, 5$ , and $6$ . The energy was averaged over 4096 realizations for $q = 3$ and over 512 realizations for each $q = 4, 5$ , and $6$ . . . .	62



4.6	(a) The average energy per spin and (b) the average number of clusters for a $q$ -state Potts model after a quench, with $q = 3, 4, 5$ , and 6. (c) The probability for a Potts model to reach the ground state by time $t = 2L^2$ after a quench to zero temperature. Data are based on $2^{14}$ realizations for the largest two values of $L$ for $q = 3$ and for the largest value of $L$ for each $q = 4, 5$ , and 6. All other data points are based on $2^{17}$ realizations. Error bars are smaller than the size of the symbols. . . . .	63
4.7	Example of a blinker state in the $2d$ Potts model. . . . .	64
4.8	Blinkers tend to remain in their intermediate states (a), rather than in an inflated or a deflated state ((b) or (c)). . . . .	64
4.9	Example of a pseudo-blinker state and a late-time coalescence event in the $2d$ Potts model. The energy drops from $E = 188$ to $E = 185$ . . . . .	65
4.10	Survival probability for the 3-state (left) and 6-state (right) Potts models. The data for each curve is averaged over $10^4$ realizations. . . . .	67
4.11	Example of a late-time cluster avalanche in the 6-state Potts model on an $L = 192$ lattice. . . . .	68
4.12	An example of a cluster expanding beyond its original convex envelope during an avalanche. . . . .	69
4.13	Schematic showing the upward expansion of the convex hull of the “1” domain. . . . .	70
4.14	Examples of four different outcomes of the avalanche shown in Fig. 4.11. . . . .	70
4.15	Examples of two realizations (top and bottom) of the 6-state $L = 192$ Potts model coarsening rapidly into a ground state. . . . .	71
4.16	Examples of long-time states in 3-state TDGL (top) and in the 3-state Potts model (bottom). . . . .	74

4.17	Probability for a 3-state TDGL evolution to end in one of the ground states (a), an Ising-like vertical or horizontal stripe state (b), a state with three hexagons (c), or a state with four clusters (d), as a function of $1/L$ and for different initial conditions. The triangles represent simulations with an initial order parameter radius equal to $1/10$ . . . . .	75
4.18	A multi-colored stripe state (a) is stable in the Potts model but is unstable in multi-state TDGL (b-d). . . . .	76
5.1	The initial interface is the boundary of a quadrant (left). At a later time $t$ , the interface encloses an area $S_t$ (right). . . . .	79
5.2	Mapping of the corner growth model onto the simple exclusion process. . .	80
5.3	Plot of the two-dimensional corner interface with nearest-neighbor ( $k = 1$ ) and nearest- and next-nearest-neighbor ( $k = 2$ ) Ising interactions. (Note that the curves have been scaled to each have unit area.) . . . . .	84
5.4	The corner interface in the presence of a bias magnetic field and for $k = 1$ (upper curve) and $k = 2$ (lower curve). . . . .	90
6.1	3d crystal of volume 4. The next elemental cube can be deposited equiprobably at any one of the 6 inner corners. . . . .	93
6.2	(left) The growth process at time $t = 140$ . (right) The interface (6.7). . . .	99
6.3	The intersection of the interface with the plane $x = y$ . The simulated curves are shown for $t = 50, 400$ , and $20000$ , and the theoretical curve (6.8) is also plotted. . . . .	101
6.4	(left) The coefficient $w_2(t)$ . (right) The coefficient $w_3(t)$ . . . . .	103
6.5	(left) The coefficient $v_2(t)$ . (right) The coefficient $v_3(t)$ . . . . .	103
6.6	The ratio $N_-/N_+$ versus $t^{-0.77}$ . This quantity appears to exceed 1 as $t \rightarrow \infty$ . 110	

6.7	Illustration showing how the numbers of inner and outer corners can be unequal for a flat plane. (left) A flat interface with equal numbers of inner and outer corners. (right) A flat interface with three outer corners for every two inner corners. . . . .	111
6.8	A $3d$ cubic crystal eroding from a corner. . . . .	112

## List of Abbreviations

KIM	Kinetic Ising Model
NN	Nearest-Neighbor
NNN	Next-Nearest-Neighbor
TDGL	Time-Dependent Ginzburg-Landau

# Chapter 1

## Introduction

Physics is the most fundamental of the sciences. A physicist's aspiration is to reduce Nature to a minimal set of mathematical laws and general principles from which all natural phenomena may be understood. On a basic level, the theories of classical mechanics, quantum mechanics, relativity, and electromagnetism have produced a highly satisfactory description of practically all everyday phenomena in the natural world. Yet the vast majority of modern research has drifted toward applied science or engineering applications.

Statistical physics is a unique field: It is neither pure nor applied. Nonequilibrium natural phenomena generally do not all reduce to a simple fundamental description, such as Newton's laws of classical mechanics, Schrodinger's equation of quantum mechanics, or Maxwell's equations of classical electromagnetism. There is no well-defined starting point for the study of systems with enormously many degrees of freedom. A statistical physicist typically makes progress by carefully studying "toy" models that are believed to capture the essential behavior of a real physical, economic, or social system. Then, it is hoped that, through universality, results on highly simplified models will deliver valuable insights into far more complex real-world phenomena.

## 1.1 Phase-Ordering Kinetics

The subject of phase-ordering kinetics involves the growth of locally stable regions that all compete for the final state of a particular process. Examples of phase-ordering kinetics abound in nature: condensation of clouds, phase separation of binary alloys, motion of anti-phase boundaries in condensed matter systems, formation of opinions in social systems, etc..

One of the most important applications of the theory of phase-ordering kinetics is to the phenomenon of ferromagnetism. Ferromagnetic metals abound in Nature, the most familiar examples being iron, nickel, and cobalt. Above each material's Curie temperature, magnetic moments within the material are all randomly aligned. Below the Curie temperature, domains of well-defined magnetization form within the material as the microscopic magnetic moments align within each domain. Without any perturbing external fields, the material is typically unmagnetized since the ferromagnetic domains are randomly oriented with respect to each other. However, each of these materials at room temperature can be magnetized by application of an external magnetic field, which forces large numbers of ferromagnetic domains to align, giving the macroscopic material a nonzero magnetic moment. When the magnetic field is removed, a ferromagnetic material will remain magnetized, a property known as hysteresis.

## 1.2 Kinetic Ising Model and its Variants

At the start of the 20th century, the development of quantum mechanics proved instrumental in understanding the behavior of the chemical elements. Yet understanding the existence of ferromagnetism remained an important challenge in statistical mechanics. The Gibbs-Boltzmann measure accurately describes classical gases and materials at high temperature. But spontaneous symmetry breaking is observed at low temperature in many systems, and at the time, it was not clear if this phenomenon could be understood within the framework of the partition function. Physicists were seeking a physical understanding of how ferromagnetism emerges in some materials.

In 1920, physicist Wilhelm Lenz invented a simple statistical mechanical model that he hoped would shed light on some of these issues. The original version of Lenz’s model consists of a one-dimensional lattice of discrete variables that each assume one of two equivalent spin states (Fig. 1.1). A spin feels the influence of only its two nearest neighbors. Increasing the numbers of nearest-neighbor pairs of aligned spins lowers the energy of the model.



Figure 1.1: The one-dimensional Ising model.

Lenz posed the problem to his student Ernst Ising, after whom the Ising model is named. In 1925, Ising provided an analytic solution of the partition function of this  $1d$  interacting spin system [1]. The free energy of the  $1d$  model exhibits no singularities and thus there is no equilibrium phase transition in one dimension. Based on the  $1d$  solution, Ising incorrectly concluded that his model shows no phase behavior in any number of spatial dimensions. Shortly afterward in 1936, Rudolf Peierls proved mathematically that the two-dimensional version of the Lenz-Ising model exhibits ordering below some critical temperature [2]. Lars Onsager later provided the full analytic solution for the partition function of the  $2d$  Ising model [3], the first toy system in statistical mechanics to demonstrate spontaneous symmetry breaking. Subsequent work focused on understanding behavior of observables such as specific heat and magnetic susceptibility at temperatures close to the second-order phase transition temperature. The universality of various scaling exponents around the transition temperature and their observation in physical systems was a remarkable success for the highly simplified Ising model of ferromagnetism.

Yet an Ising model defined solely by a Hamiltonian function may only be mathematically studied in the equilibrium context. To model kinetic effects in ferromagnetism (for example, rapidly changing the temperature of a ferromagnetic material about its Curie point), one must additionally define a dynamics for the Ising spin system. Interestingly, the choice of dynamics is not unique. To guarantee that the Ising spin system reaches equilibrium at any

finite temperature, we make our choice of dynamics consistent with the detailed balance principle [4]. Mathematically,

$$p_i w_{i \rightarrow j} = p_j w_{j \rightarrow i}, \quad (1.1)$$

where  $p_i$  is the probability that the system is in state  $i$ , and  $w_{i \rightarrow j}$  is the transition rate from state  $i$  to state  $j$ . Physically, detailed balance demands that the net flux between any two microstates of the system be zero. Although the exact choice of dynamics is not unique, based on universality, different rules that all satisfy the detailed balance condition are believed to give qualitatively similar results.

More recently, the Ising model has been extended in many ways. One may employ nonuniform couplings  $J_{ij}$  between different spins in the lattice to mimic anisotropy in real materials. Changing some of the couplings to be antiferromagnetic leads to a slow approach to the equilibrium state. One may also extend the spin-spin coupling length to more distant neighboring spins, and perhaps modify the underlying graph determining how spins interact with each other.

In this work, I focus mainly on simple forms of the Ising model. My studies on a deep temperature quench of a three-dimensional Ising model involve only the simplest scenario with nearest-neighbor, uniform, ferromagnetic spin couplings. Even in two-dimensions, we use mostly this simplest form of the Ising model, occasionally making modifications to the interaction Hamiltonian for technical reasons. In all Ising model simulations, we use simple square ( $2d$ ) or cubic ( $3d$ ) lattices.

Below its second-order phase transition temperature  $T_C$ , the kinetic Ising model in dimension  $d > 1$  is globally ordered in equilibrium. But this raises the question: What happens if a kinetic Ising model is rapidly cooled from a high supercritical temperature to a low subcritical temperature. Does the system quickly equilibrate? On the surface, this may seem a trivial question, but in reality, the Ising system does not take a direct route to the equilibrium state.

To appreciate the complexities associated with coarsening in the simple Ising model, consider Figure 1.2. The two-dimensional spin system is initially prepared in a totally



uncorrelated random state, corresponding to initial temperature  $T_I = \infty$ . Starting at time  $t = 0$  the operating temperature is set to  $T_F = 0$ , and the Ising spin system evolves according to zero-temperature single-spin-flip dynamics. Physically, only energy-lowering spin flips are allowed to occur.

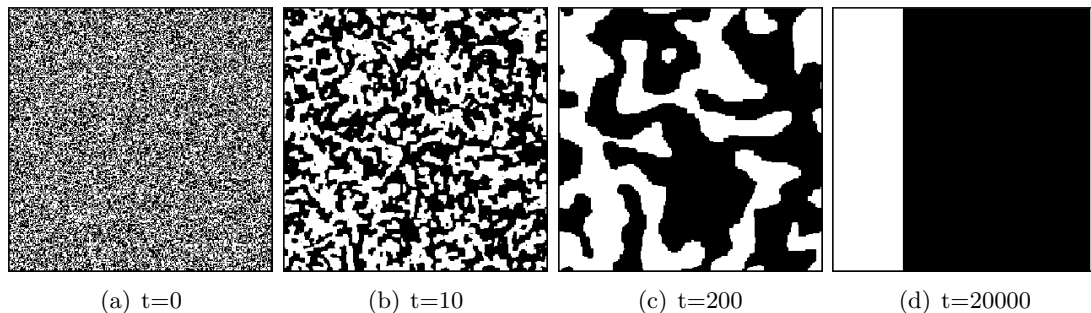


Figure 1.2: Coarsening in the two-dimensional Ising model using single-spin-flip dynamics at zero temperature. The competition between the two phases leads to nontrivial long-time states. The system size is  $L \times L$ , with  $L = 256$ .

With the supercritical initial state, the average initial magnetization is zero. However, stochasticity in the spatial distribution of up/down spins and in the first spin-flip events naturally cause some regions of the lattice to contain mostly up spins while other regions contain mostly down spins (Fig. 1.2). Spins within each small region of the lattice quickly equilibrate with their immediate neighbors, but spins in distant regions of the graph do not all drift toward the same equilibrium state. At intermediate times after the quench, a patchwork of equilibrium domains forms throughout the lattice, and neighboring domains compete to select the global equilibrium state. Early researchers noted that, at late times in the evolution, stochastic single spin-flip dynamics is effectively replaced by deterministic motion that only occurs on domain walls between clusters. This led to the development of simple deterministic descriptions of phase-ordering kinetics in the Ising model that are based on a coarse-grained order-parameter field representing the magnetization density in a local region of space.

### 1.3 Time-Dependent Ginzburg-Landau Theory

In statistical mechanics, complex, non-equilibrium, strongly-interacting systems are often incredibly difficult or impossible to understand rigorously. In our present case, a microscopic, fundamental analytical treatment of coarsening in spin systems is effectively hopeless. To make progress in understanding the long-time state of a kinetic Ising system following a deep temperature quench, it is helpful to set up a phenomenological description of coarsening. Phenomenological theories relate macroscopic physical observables in ways that are consistent with fundamental physics, but these theories are not derived from microscopic interactions.

For the case of the Ising model, we construct a coarse-grained order-parameter field  $\phi(\vec{x}, t)$  that will become the object of our attention. Intuitively, the field  $\phi(\vec{x}, t)$  represents, at time  $t$ , the average magnetization in a small region of space about  $\vec{x}$  whose length scale is large compared with the lattice spacing  $a$  but small compared with the system size  $L$ . In this limit,  $\phi(\vec{x}, t)$  varies continuously in  $\vec{x}$  and  $t$ .

To describe phase-ordering physics and to be of practical use, our constructed order parameter field must satisfy a simple equation of motion that respects fundamental thermodynamic principles. A suitable Landau free-energy functional to describe the Ising model dynamics is

$$F[\phi(\vec{x}, t)] = \int \frac{1}{2} \{ [\nabla\phi(\vec{x}, t)]^2 + [\phi(\vec{x}, t) - 1]^2 [\phi(\vec{x}, t) + 1]^2 \} d^d x \quad (1.2)$$

To obtain an equation of motion for a nonconserved order parameter field, we compute the functional derivative

$$\frac{\partial\phi}{\partial t} = -\frac{\delta F[\phi]}{\delta\phi} = \nabla^2\phi + 2\phi(1 - \phi^2) \quad (1.3)$$

This is the time-dependent Ginzburg-Landau (TDGL) equation for a nonconserved order parameter field [5, 4]. Intuitively, the local spin-spin interactions tend to favor all spins in a small neighborhood to be aligned ( $\phi = +1$  or  $\phi = -1$ ). This behavior is captured in the potential term in Eq. (1.3). Also, the order parameter field at a point  $\vec{x}$  drifts toward

the average magnetization of points in its neighborhood on the lattice. This is represented by the Laplacian term in Eq. (1.3). In the late stages of evolution, all activity occurs on the domain walls between ordered phases (Fig. 1.2(c-d)). Smooth domain walls move and straighten so as to minimize their surface tension.

If we choose to believe that this deterministic reaction-diffusion equation captures all essential physics of a deep temperature quench of a kinetic Ising model, then we should be able to extract information about the late-time statistics of the Ising quench by studying late-time solutions to Eq. 1.3. In numerical studies, we must average the TDGL evolution over many independent random initial conditions to obtain meaningful statistics. However, we can analytically extract useful information about scaling phenomena in nonconserved coarsening.

For simplicity, first consider a circular domain of magnetization  $\phi = +1$  in a background of magnetization  $\phi = -1$  (Fig. 1.3(a)). We expect

$$\phi(r, t) = f(r - R(t)), \quad (1.4)$$

where  $R(t)$  is the radius of the circular cluster at time  $t$ . Writing the TDGL equation in spherical coordinates and using the form (1.4), we obtain

$$0 = \frac{d^2 f}{dr^2} + \left( \frac{d-1}{r} + \frac{dR}{dt} \right) \frac{df}{dr} - \frac{dV}{df}$$

Multiplying this equation by  $df/dr$  and integrating through the interface gives

$$\frac{dR(t)}{dt} = -\frac{d-1}{R},$$

After integrating, we obtain  $R^2(t) = R^2(0) - 2(d-1)t$ . From this, we see that the time for a circular domain of initial radius  $R(0)$  to disappear scales as  $t \sim R^2(0)$ .

More generally, for an arbitrarily curved interface between spin domains, we identify that the gradient of the field  $\phi(\vec{x}, t)$  can be written as  $\nabla\phi = (\partial\phi/\partial n)_t \hat{n}$ , where  $\hat{n}$  is a unit vector normal to the domain wall between clusters. Then, plugging  $\nabla^2\phi = (\partial^2\phi/\partial n^2)_t +$

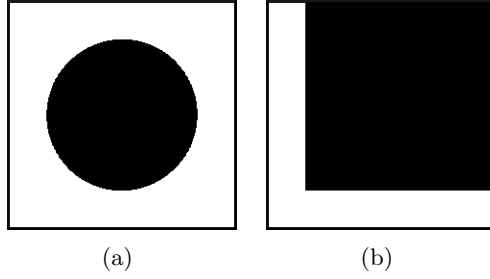


Figure 1.3: (a) A circular domain of one phase in a background of the opposite phase. (b) A wedge-shaped domain.

$(\partial\phi/\partial n)_t \nabla \cdot \hat{n}$  and  $(\partial\phi/\partial t)_n = -(\partial\phi/\partial n)_t (\partial\hat{n}/\partial t)_\phi$  into Eq. (1.3), we arrive at

$$v = -\nabla \cdot \hat{n} = -(d-1)\kappa, \quad (1.5)$$

where  $v$  is the interface velocity, and  $\kappa$  is the mean curvature of the interface. Eq. (1.5) is the Allen-Cahn equation, which describes domain wall motion in the late-time evolution of an order parameter field governed by the TDGL equation [6, 5].

From the general Allen-Cahn equation, we can understand on physical grounds the scaling result that the time for a domain of initial length scale  $L(0)$  to shrink to zero size scales as  $t^z$ , with dynamic exponent  $z = 1/2$ . We denote by  $[L]$  the characteristic length scale of a cluster and by  $[T]$  the characteristic time for the domain to collapse under its own surface tension. Since the mean curvature of an interface has dimension  $1/[L]$ , dimensional analysis on the Allen-Cahn equation (1.5) yields

$$\frac{d[L]}{d[T]} \sim \frac{1}{[L]},$$

and power counting gives  $[L]^2 \sim [T]$ .

If the order parameter is strictly conserved, as in phase separation of a binary alloy, then the Allen-Cahn equation does not apply, and the task of finding scaling relations becomes more complicated. In conserved coarsening processes, the general scaling result  $L(0) \sim t^z$  still holds, but now with dynamic exponent  $z = 1/3$  [5]. In this thesis, I focus exclusively

on dynamics that do not conserve the order parameter.

## 1.4 Current Research

Our analysis thus far may lead one to naively expect that nonconserved coarsening behaves as follows. Shortly after a quench to subcritical temperature, domains of plus and minus phase grow throughout the system and compete for the equilibrium state. Due to random fluctuations in microscopic domain ordering and due to the effects of correlations in the initial state, one of the two equilibrium phases will grow to occupy a larger fraction of the system. When the largest cluster’s length scale becomes of the order of the system size, the system has reached one of its two equilibrium states. This overly-simplistic view of coarsening may be called the “central dogma” of phase-ordering kinetics when the order parameter is not globally conserved.

The central dogma of nonconserved coarsening actually makes correct predictions for one-dimensional systems. For the one-dimensional Ising model, for example, the dynamics at zero temperature corresponds to each interface between spin domains (that is, each point where an up spin is adjacent to a down spin) performing a symmetric random walk. When two interfaces between spin domains meet, they annihilate each other, and the total number of spin clusters decreases by one. Since the domain length scale grows as  $\sqrt{t}$ , the time required for all domain walls to meet and annihilate in a finite system of length  $L$  scales as  $L^2$ . In a one-dimensional TDGL system, the only possible final state at zero temperature is similarly one of the two ground states, with the caveat that the time to reach one of the two ground states scales exponentially in the system size  $L$  [4].

However, in greater than one spatial dimension, systems with nonconserved, scalar order parameters tend to become trapped in long-lived metastable states, thereby complicating the approach to equilibrium. A two-dimensional kinetic Ising model, for example, may become trapped in a metastable “stripe” state following a deep temperature quench (Fig. 1.2). Notice that, since all spin clusters span the lattice, flipping any spin in Figure 1.2(d) results in an increase in the number of antialigned spin pairs, and hence raises the energy. At

very low temperatures, such energy-raising moves are strongly suppressed, and this system remains trapped in this metastable configuration. Similar, but much more complex, metastable long-time states appear in the quench of a three-dimensional Ising model, although in the  $3d$  setting metastable states appear much more ubiquitously. If the operating temperature is  $T = 0$ , then, depending on the model, a system that falls into one of these metastable configurations typically cannot reach the ground state, and the freezing becomes permanent. So while the central dogma of coarsening is morally correct by incorporating fundamental, qualitative physical behavior of out-of-equilibrium coarsening dynamics, it neglects important features of discrete spin models, and it is definitely not the last word in generically understanding phase-ordering kinetics.

Thus far, we have discussed the final outcome of a coarsening system starting from a high-temperature, random initial state. A complementary problem involves domain wall motion in a nonconserved coarsening system starting from a smooth, deterministic initial condition. As an example of the latter case, consider Figure 1.3(b). Starting from the macroscopically smooth “wedge” geometry in  $2d$ , the domain in the upper-right of the figure will deterministically shrink under the influence of its surface tension. Naively, one may hope that the equation of motion for the smooth domain interface in this example is given by the Allen-Cahn result, i.e., that interface motion is driven purely by local curvature of the interface.

In this thesis, I carefully study two connected problems:

- Starting from a random, high-temperature initial condition, how do spin domains form and evolve with dynamics that do not conserve the order parameter? Can the late-time outcome of a typical temperature quench be predicted from theory? Can the metastable states that form in two and higher spatial dimensions be reliably characterized? Specifically, what are the zero- and finite-temperature mechanisms responsible for slow late-time behavior in quenched ferromagnets? Additionally, how is late-time behavior modified if there are more than two competing equivalent spin states?

- Starting instead from a smooth, deterministic initial domain structure, and incorporating non-conserved order parameter dynamics, how do the interfaces between spin domains evolve? Does the Allen-Cahn result provide a faithful description of domain wall motion universally for all microscopic models that would be expected to obey curvature-driven coarsening in a macroscopic sense? If not, then how do lattice anisotropies and spin-spin interactions affect deterministic interfacial equations of motion? What is the role of the spatial dimension in constructing suitable equations of domain wall motion? Also, what are the limiting interface shapes that result from different interfacial equations of motion in both two and higher dimensions?

We begin by studying the quench of a kinetic spin system from high supercritical temperature to zero temperature. While freezing has been shown to occur [7], the myriad complexities that arise as a kinetic spin system approaches equilibrium have been mostly overlooked. A unifying theme in two-dimensional nonconserved coarsening, either of a kinetic spin system or of the TDGL equation, is a high degree of universality in the probabilities of a given system reaching any of an infinite number of metastable stripe states. Researchers in the past several years began observing an intriguing connection between domain patterns in coarsening  $2d$  ferromagnets and continuum critical percolation. In Chapter 2 of this thesis, I demonstrate, both analytically and numerically, that the connection between two-dimensional coarsening and percolation is much deeper than had previously been anticipated.

Three-dimensional coarsening of kinetic spin systems is far more complex. A pioneering, detailed numerical study on the quench of a three-dimensional kinetic Ising model to  $T = 0$  [7] revealed non-static final states and hinted at an anomalously slow relaxation of the energy. A major focal point of my thesis research involves characterizing the non-static behavior and understanding the slow energy relaxation of a three-dimensional zero-temperature kinetic Ising ferromagnet. Our new results on three-dimensional coarsening, together with our novel visualization and animation techniques, are presented in Chapter 3. Amazingly, the exotic features of three-dimensional coarsening of a kinetic spin system also appear in

the subcritical temperature quench of a two-dimensional kinetic Potts model. Chapter 4 focuses on details of a quench of a kinetic Potts model to zero temperature, and more generically on multi-state TDGL coarsening.

The remainder of this dissertation focuses on understanding curvature-driven domain wall motion with smooth, deterministic initial conditions. For microscopically discrete spin systems in two and three dimensions, we do not find a universal governing equation for interface motion. In Chapter 5, for each spin dynamics model that we consider in two dimensions, we establish the correct equations for interface motion. For interesting idealized initial geometries, we then solve our governing equations to obtain exact forms for the limiting interface shapes. Domain wall motion in three dimensions, examined in Chapter 6, is much more challenging. We use some novel analysis, incorporating limiting behavior, symmetries, and a little help from numerics, to conjecture an amazingly simple and elegant equation of motion for three-dimensional corner growth. We solve our growth equation analytically and find outstanding agreement with simulations of the corner growth process in three dimensions.



## Chapter 2

# Universality of Two-Dimensional Curvature-Driven Coarsening

In the first half of this dissertation, I consider the following question: How does phase-ordering proceed if an Ising model is instantaneously quenched from a random, infinite-temperature initial state to zero temperature? By instantaneously quenching the temperature, we avoid any complications due to the quenching protocol, and we can focus exclusively on the time scales associated with coarsening.

According to the standard picture from phase-ordering kinetics [5], shortly after the temperature quench, an intricate domain mosaic develops, and domain coarsening becomes a deterministic process driven by local domain wall curvature. Exact results in the theory of phase-ordering kinetics have proven difficult to achieve. Rare exactly soluble models include the Glauber model in one dimension and the  $n$ -vector model with  $n \rightarrow \infty$  [5]. To develop understanding for the vast majority of statistical systems that exhibit coarsening, physicists rely heavily on computer simulations and physical experiments, combined with only qualitative and approximate theoretical arguments. Despite the complexity of nonconserved coarsening, there exists a surprisingly high degree of universality in the two-dimensional setting. As we shall see, recent connections between coarsening in a two-fold degenerate system and percolation theory have opened a powerful route to understanding the beautiful intricacies of two-dimensional coarsening while providing precise predictions for various

coarsening outcomes.

## 2.1 Predictions from Percolation Theory

Percolation theory is the field of mathematics concerning the connectivity of clusters in random graphs [8]. Mathematically, one has a collection of nodes that are joined by bonds, and each bond may be active or inactive. A group of nodes that are all connected via a sequence of active bonds is termed a connected cluster. The basic physical question that percolation theory addresses is: Which statistical configurations of nodes and bonds produce connected paths through a system? Percolation theory is versatile and powerful, providing important understanding in diverse fields, including physics, materials science, complex network science, epidemiology, filtration, and spreading of forest fires.

We are interested in nonconserved coarsening in the two-dimensional Ising model. Spirin, Krapivsky, and Redner [7] found that a  $2d$  Ising model quenched to zero temperature reaches the ground state with probability  $\sim 2/3$ . Surprisingly, the remaining fraction of realizations become trapped in infinitely long-lived “stripe” states at zero temperature (Fig. 1.2). At some early time in the dynamics, a percolating stripe phase may form. As coarsening progresses, any percolating stripes will gradually straighten under their surface tension, but topologically they can never vanish. For a percolating stripe to disappear after a long time would require a sufficient thermal fluctuation to carve a path through the stripe, but at zero-temperature, such thermally-activated processes cannot occur.

Can percolation theory tell us anything about freezing into stripe states in two-dimensional ferromagnets? The answer is yes. However, there are some subtleties. For instance, site percolation on a square lattice is not applicable for describing coarsening. For site percolation on the square lattice, computer simulations have determined the critical density of occupied sites for the existence of a spanning cluster to be  $p_c = 0.59274605(3)$  [9]. In the limit of infinite system size, for density  $p < p_c$ , there never exists a spanning cluster, while for  $p > p_c$ , there always exists a spanning cluster. The initial densities of plus and minus spins in the Ising model at  $T = \infty$  are each equal to  $1/2$ , strictly less than the threshold

for site percolation on a square lattice. Therefore, at time  $t = 0$ , no spin clusters span the system.

Instead, imagine we have a continuous and random potential function  $V(x, y)$  on a two-dimensional lattice. The random potential will have hills and valleys, and its mean over all space is  $\mathcal{V}$ . To draw parallels with the  $2d$  Ising model, we may color regions where  $V(x, y) > 0$  in white and regions where  $V(x, y) < 0$  in black. Physically we may ask: For a given value of  $\mathcal{V}$ , do any white or black domains span the  $2d$  lattice? It turns out that for  $\mathcal{V} < 0$ , there is a black cluster that percolates with probability 1, while for  $\mathcal{V} > 0$ , there is a white cluster that percolates with probability 1. The interesting case of  $\mathcal{V} = 0$  corresponds to critical continuum percolation, where crossing probabilities of black and white clusters are strictly between 0 and 1 [10, 11, 12]. These results hold with a high degree of universality; i.e., they are correct for a broad class of random potential functions [13].

Within the last decade, it has been noticed that the  $2d$  Ising model shortly after a temperature quench visually resembles cluster patterns in *continuum* percolation [14, 15]. At supercritical initial temperature, the Ising model has zero magnetization. The magnetization remains zero during the early stages of coarsening, so a mapping of the Ising model shortly after a quench to critical continuum percolation is plausible. Over the past several years, numerical evidence in support of such a connection has mounted, and the mapping with percolation appears to be exact for a broad class of dynamical models. Crucially, once the kinetic Ising system has reached the state of critical continuum percolation, the subsequent evolution of the spin domains is essentially deterministic since the evolution is driven solely by mean curvature of the interfaces between spin domains [15].

To demonstrate the power of the percolation mapping, consider the distribution of hull-enclosed areas in the quench of a  $2d$  Ising model. A hull is defined as any closed interface of a cluster, which may or may not enclose additional smaller clusters. Aizenon *et. al.* [14] recognized that the statistics of hull-enclosed areas at a time shortly after the quench in  $2d$  nonconserved coarsening and in  $2d$  critical continuum percolation are identical. Combining results for hull-enclosed area statistics in percolation theory [16] with

curvature-driven coarsening, they predicted that the number of hulls per unit area of the system  $N_h(A, t)$  with enclosed area greater than  $A$  at time  $t$  is given by

$$N_h(A, t) = \frac{1}{4\pi\sqrt{3}(A + \lambda t)}, \quad (2.1)$$

where  $\lambda$  is a model-dependent parameter. Scaling, i.e. that the typical area  $A$  in the system scales with time  $t$ , follows naturally from this more general prediction. Numerical experiments on coarsening in the  $2d$  Ising model verified Eq. (2.1), which is quite remarkable as two-dimensional nonconserved coarsening was long believed to be beyond the reach of precise mathematical analysis [5].

## 2.2 Stripe States in Models that Exhibit Nonconserved Coarsening

In this chapter, we study coarsening in several simple two-dimensional models that have two-fold degeneracy of the ground state. Specifically, we are concerned with the long-time state after the growing domains have become commensurate with the system size.

To understand coarsening into stripe states with mathematical precision, we rely on two key observations:

1. Shortly after the temperature quench, the typical size of a domain is large compared with the lattice spacing  $a$  and is small compared with the system size  $L$ . The cluster patterns visually resemble those of critical continuum percolation.
2. Once the state of critical continuum percolation has been reached, domain walls between spin clusters are macroscopically smooth, and curvature-driven interface motion becomes deterministic.

We want to predict the probabilities for a two-dimensional ferromagnet to coarsen into a long-lived stripe state at zero temperature. If percolation theory can predict quantitative features of hull area distributions in coarsening  $2d$  ferromagnets, then can it also predict

various stripe state probabilities?

Boundary conditions play an important role in the allowed late-time cluster patterns. With free boundary conditions, there are only four allowed topologies: no spanning ( $\mathcal{F}_{\bar{h}\bar{v}}$ ), dual spanning ( $\mathcal{F}_{hv} = \mathcal{F}_{\bar{h}\bar{v}}$  by symmetry), horizontal spanning ( $\mathcal{F}_{h\bar{v}}$ ), or vertical spanning ( $\mathcal{F}_{\bar{h}v}$ ). Thus we have the normalization condition

$$2\mathcal{F}_{hv} + \mathcal{F}_{h\bar{v}} + \mathcal{F}_{\bar{h}v} = 1. \quad (2.2)$$

Beautiful expressions for crossing probabilities have been calculated using conformal field theory [10, 11, 17, 18], and some of these have been proven [19]. We have

$$\mathcal{F}_{\bar{h}v}(r) = \frac{\sqrt{3}}{2\pi} \lambda {}_3F_2 \left( 1, 1, \frac{4}{3}; \frac{5}{3}, 2; \lambda \right) \quad (2.3)$$

as the probability for vertical spanning on a rectangle with aspect ratio  $r$  (ratio of height to width). Here,  ${}_pF_q(a_1, \dots, a_p; b_1, \dots, b_q; \lambda)$  is the generalized hypergeometric function [20],  $\lambda = \lambda(r)$  is defined implicitly by

$$\lambda = \left( \frac{1-k}{1+k} \right)^2, \quad r = \frac{2K(k^2)}{K(1-k^2)},$$

and  $K(u)$  is the complete elliptic integral of the first kind [20]. Furthermore, by symmetry, we have the duality relation

$$\mathcal{F}_{h\bar{v}} \left( \frac{1}{r} \right) = \mathcal{F}_{\bar{h}v}(r).$$

The predictions for freezing into various stripe topologies were tested in Ref. [15] for different aspect ratios  $r$ , and the agreement with numerics is excellent. Consider a square lattice with free boundaries ( $r = 1$ ), so that these equations reduce to

$$2\mathcal{F}_{hv} = \frac{1}{2} + \frac{\sqrt{3}}{2\pi} \ln \left( \frac{27}{16} \right) = 0.644240\dots \quad (2.4)$$

for the probability of reaching a ground state.

For the case with periodic boundaries, we do not have a clean analytical prediction

for the probability of reaching a ground state, due to the possibility for stripes that wind multiple times in both directions around the torus. (Mathematically, there is no simple conservation law corresponding to Eq. (2.2) with finitely-many terms.) Numerically, our prediction is:

$$P_{\text{ground}} = 0.661169\dots \quad (2.5)$$

To probe new aspects of  $2d$  coarsening, we focus here on periodic boundary conditions. Consider the probability

$$\mathcal{P}_{a,b}(r) = \frac{\mathcal{Z}_{a,b}(6;r) - 2\mathcal{Z}_{a,b}(\frac{8}{3};r) + \mathcal{Z}_{a,b}(\frac{2}{3};r)}{2[\eta(e^{-2\pi r})]^2} \quad (2.6)$$

for a  $2d$  critical continuum percolating system to feature oppositely-colored spanning clusters with winding numbers  $a$  and  $b$  on a rectangle with aspect ratio  $r$  and periodic boundaries [11]. The function  $\mathcal{Z}_{a,b}(G;r)$  is the infinite sum

$$\mathcal{Z}_{a,b}(G;r) = \sqrt{\frac{G}{r}} \sum_{j=-\infty}^{\infty} \exp\left[-\pi G \left(\frac{a^2}{r} + b^2 r\right) j^2\right]. \quad (2.7)$$

These formulae for continuum percolation crossing probabilities were expanded in Ref. [15] with  $(a,b) = (1,0), (0,1)$  for various aspect ratios. The observed probabilities of freezing into horizontal ( $a = 1, b = 0$ ) and vertical ( $a = 0, b = 1$ ) stripes in  $2d$  Monte Carlo coarsening simulations for different aspect ratios was shown to agree phenomenally well with predictions [15]. This is actually quite surprising, as the continuum percolation results were derived from an equilibrium statistical ensemble, while our coarsening systems are far from equilibrium. The numerical probabilities of coarsening into stripe states reported in [15] are sufficiently close to the percolation probabilities that one wonders if the correspondence may be exact in the thermodynamic limit.

We further exploit this connection to understand coarsening into more esoteric stripe topologies. First considering just the periodic square lattice, we wish to predict the probability of coarsening into stripes with general winding numbers  $a, b$ . We use the series

representation of the Dedekind  $\eta$  function [12]

$$[\eta(\rho^{12})]^{-2} = \rho^{-1}(1 + 2\rho^{12} + 5\rho^{24} + 10\rho^{36} + \dots) \quad (2.8)$$

with  $\rho \equiv e^{-\pi/6}$  in (2.6) to obtain

$$P_0 = \sqrt{\frac{8}{3}}\rho^3(1 - \rho^{12} - \rho^{24} + 4\rho^{32} + \dots) \quad (2.9)$$

$$P_1 = \sqrt{\frac{8}{3}}\rho^7(1 + 2\rho^{12} + 2\rho^{24} + 4\rho^{36} + \dots) \quad (2.10)$$

$$P_n = \sqrt{\frac{32}{3}}\rho^{4n^2+3}(1 + 2\rho^{12} + 5\rho^{24} + 10\rho^{36} + \dots) \quad (2.11)$$

as the probabilities for coarsening into a state with horizontal or vertical stripes ( $P_0 = \mathcal{P}_{1,0} + \mathcal{P}_{0,1} = 2\mathcal{P}_{1,0}$ ), a state with diagonal stripes either in the  $(1,1)$  or  $(-1,1)$  directions ( $P_1 = \mathcal{P}_{1,1} + \mathcal{P}_{-1,1} = 2\mathcal{P}_{1,1}$ ), or a state with stripes of higher winding numbers in any of the four  $(\pm n, 1)$  or  $(\pm 1, n)$  directions ( $P_n = 4\mathcal{P}_{n,1}$ ). Figure 2.2 shows the formation of a  $(1,1)$  diagonal stripe and a  $(2,1)$  diagonal stripe on a periodic square lattice.

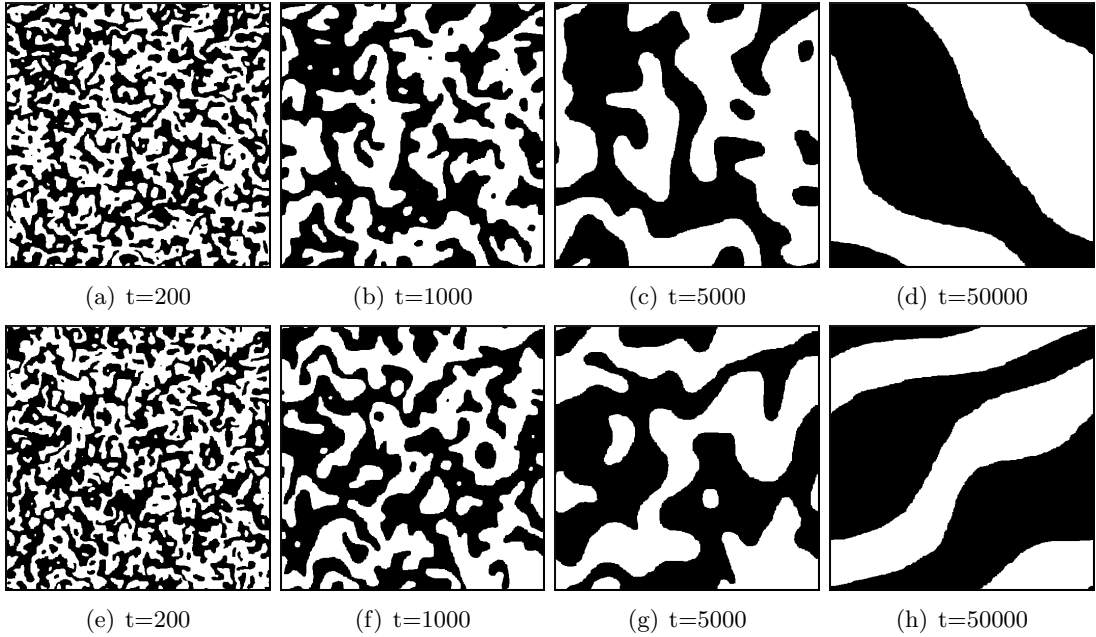


Figure 2.1: Formation of a  $(1,1)$  diagonal stripe (top) and a  $(2,1)$  diagonal stripe (bottom) in the  $2d$  Ising model quenched to zero temperature. The system size is  $L \times L$ , with  $L = 1024$ .

Secondly, we may consider the formation of stripes with winding numbers  $(\pm n, 1)$  on an  $L \times nL$  rectangle. We find that in continuum critical percolation, these diagonal stripe states on  $L \times nL$  lattices occur with probability

$$\Pi_n = \sqrt{\frac{8}{3n}} \rho^{7n} (1 + 2\rho^{12n} + 2\rho^{24n} + \dots). \quad (2.12)$$

### 2.2.1 Simulation Results

We numerically tested two basic questions: First, do the probabilities of coarsening into various stripe topologies agree for different model systems? We simulated three models: the kinetic Ising model (KIM) with homogeneous nearest-neighbor spin-spin interactions, the KIM with homogeneous nearest- and (diagonal) next-nearest-neighbor spin-spin interactions, and the TDGL equation (1.3). Second, do these probabilities agree with our predictions from critical continuum percolation?

Our simulation procedure is as follows. We initialize a square lattice with  $L^2$  spin variables with  $L^2/2$  spins in the “up” state and the remaining  $L^2/2$  spins in the “down” state. We order the up and down spins randomly on the grid, thereby mimicking a quench from infinite temperature. The working temperature is instantaneously set to zero, and we employ strictly energy-lowering Glauber dynamics [21]. We could just select a spin equiprobably from all  $L^2$  spins, check the energy change that would result from flipping the spin, flip or not flip the spin accordingly, and repeat for the desired Monte Carlo time. However, this direct simulation method is hopelessly inefficient because at late times in the zero-temperature dynamics, nearly all activity occurs on domain boundaries—a small subset of all spins in the system. Therefore, we maintain a list of spins in the system that are eligible to flip on the next attempt. We choose only spins from this list to flip, and after each move, we update the list accordingly. This is just a reorganization of standard Glauber [21] or Metropolis [22] dynamics, and the enhanced technique goes by many names, including the kinetic Monte Carlo method [23], the Gillespie algorithm [24], and the n-fold way [25].



For different values of system size  $L$ , we run many realizations. Figure 2.2 shows our data for the three models, and our predictions for each measurement are shown as red arrows. The agreement between the three models in the large- $L$  limit and the match between theory and experiment are excellent.

### 2.3 Stability of Topologies

Cooperative behavior in  $2d$  coarsening should not depend in any fundamental way on the range of spin-spin interactions as long as these interactions decay rapidly with the distance between spins. There are however important subtleties that arise. A horizontal or vertical stripe state is stable at  $T = 0$  with NN interactions (Fig. 1.2(d)). A diagonal stripe that winds once horizontally and once vertically around the torus (Fig. 2.2(top)) is unstable with only NN interactions. A staircase interface in the  $(1, 1)$  direction has equal numbers of inner and outer corners. With NN interactions, each inner and outer corner can flip equiprobably, and a staircase interface on an  $L \times L$  lattice has of order  $L$  of these height extrema. In a single time step, the interface's center of mass typically moves a distance  $\Delta y \sim \sqrt{L}/L$ , which gives an effective interface diffusivity  $D \sim (\Delta y)^2 \sim L^{-1}$ . For two domain walls to meet in a diagonal stripe state, one has to wait a time  $t \sim L^2/D \sim L^3$ . However, with NN interactions and weaker NNN interactions, the staircase in the  $(1, 1)$  direction becomes stable at  $T = 0$ . Similarly, a  $(2, 1)$  stripe state (Fig. 2.2(bottom)) is unstable for both NN interactions and for NN and weaker NNN interactions, but becomes stable with additional longer-range interactions.

The interaction range has subtle implications for the late-time behavior of the  $2d$  KIM. We introduce the survival probability  $S(t)$  as the probability that a given realization of the  $T = 0$  quench has flippable spins remaining at time  $t$ . Figure 2.3 shows  $S(t)$  for an  $L = 64$  system with only NN interactions and another  $L = 64$  system with NN and weaker NNN interactions. In both curves, notice the separation of time scales.  $S(t)$  decays exponentially as  $\exp(-t/\tau)$  with time constant  $\tau \sim L^2$  during the early-time regime. After the kink,  $S(t)$  again decays exponentially, but now with time constant  $\tau \sim L^3$ . For the KIM with only

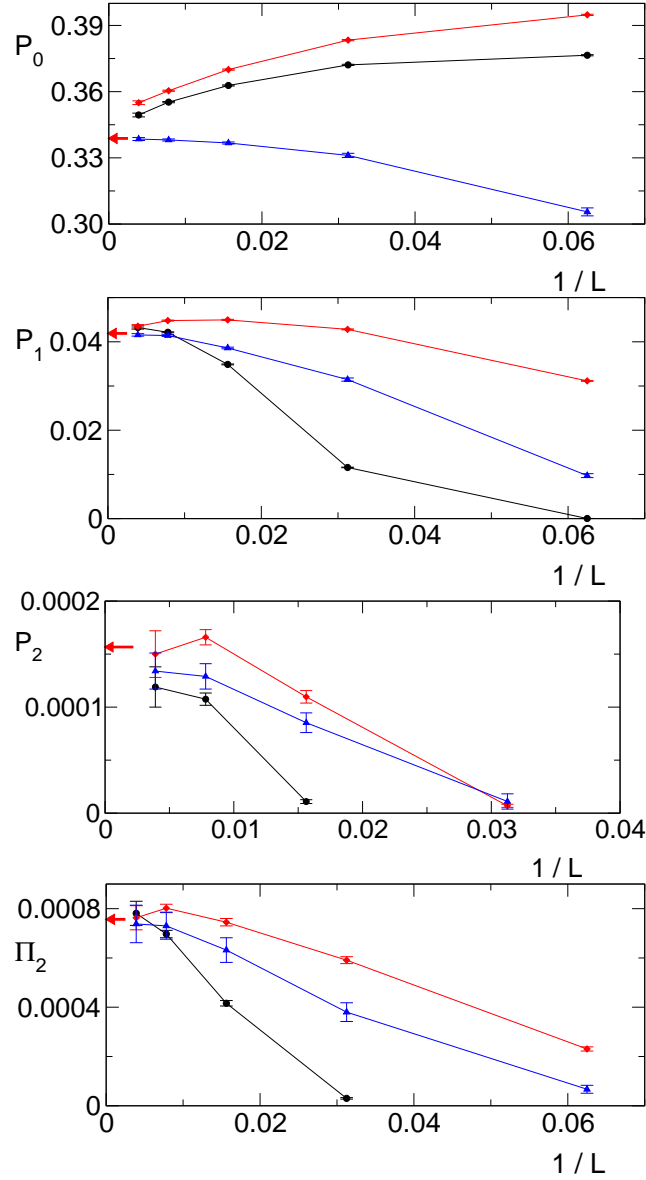


Figure 2.2: Probabilities of coarsening into a (1,0) stripe on a square, a (1,1) stripe on a square, a (2,1) stripe on a square, and a (2,1) stripe on a rectangle with aspect ratio  $r = 2$  (top to bottom). For each case, the probabilities for the Ising model with NN interactions (black circles), the Ising model with NNN interactions (red diamonds), and the TDGL equation (blue triangles) are shown. For simulations of the KIM,  $3.2 \times 10^6$  realizations were used for  $L = 16, 32, 64$ , and  $128$ , and  $3.2 \times 10^5$  realizations were used for  $L = 256$ . For simulations of the TDGL equation,  $10^6$  realizations were used for  $L = 16, 32, 64$ , and  $128$ , and  $5 \times 10^5$  realizations were used for  $L = 256$ .

NN interactions, the roughly 5% of realizations that are still active at times beyond the kink are predominantly (1, 1) stripes. For the KIM with NN and weaker NNN interactions, the fraction  $\approx 10^{-4}$  of realizations that are still active at late times are predominantly (2, 1) stripes. These numbers are remarkably close to our predictions for the probabilities of forming (1, 1) and (2, 1) stripes, 0.0419 and  $1.567 \times 10^{-4}$ , from percolation theory, providing a nice theoretical understanding of our survival probability data.

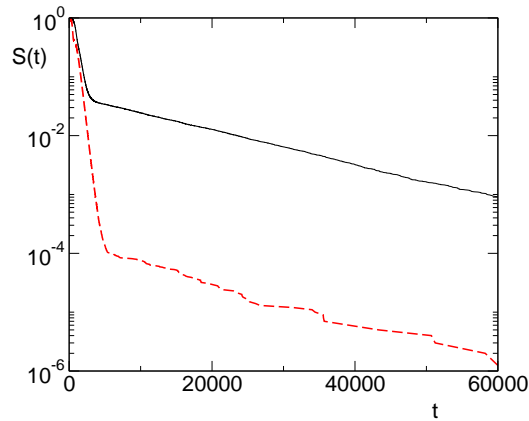


Figure 2.3: Survival probability  $S(t)$  for an  $L = 64$  KIM with only NN interactions (solid/black,  $10^5$  realizations) and for NN and NNN interactions (dashed/red,  $10^6$  realizations).

Let's assume that we have spin-spin interactions that decay rapidly with distance. What are the criteria for stability of a staircase with general winding numbers  $a$  and  $b$  on the square lattice? As a first rule, note that adjacent horizontal and vertical segments of an interface cannot both be longer than 1 without the interface being unstable. For example, a (1, 1) stripe can be composed of a sequence of horizontal and vertical segments each of width two, but this structure will evolve into a staircase with horizontal and vertical segments each of width one. We denote this latter configuration as  $\mathbf{1}^\infty$  and each individual building block as  $\mathbf{1} = [1, 1]$ . The (1, 2) stripe is composed of building blocks  $\mathbf{2} = [1, 2]$ , leading to a  $\mathbf{2}^\infty$  staircase. We see that the only stable staircase of a (1,  $n$ ) stripe is  $\mathbf{n}^\infty$ , with  $\mathbf{n} = [1, n]$ . As additional examples, the staircase  $(\mathbf{12})^\infty$  yields a stable stripe in the (2, 3) direction, the staircase  $(\mathbf{112})^\infty$  yields a stable stripe in the (3, 4) direction, and the staircase  $(\mathbf{122})^\infty$

yields a stable stripe in the  $(3, 5)$  direction.

There are an infinite number of possibilities for forming a stripe with given winding numbers  $(a, b)$ . For example, a  $(2, 3)$  stripe can have the staircase  $(\mathbf{12})^\infty$ , the staircase  $(\mathbf{1122})^\infty$ , or an infinite number of other possibilities. Yet the latter form is unstable and eventually decays into  $(\mathbf{12})^\infty$ . This suggests a second rule for constructing stripe states: Only minimal representations are stable.

We also note a connection between combining elemental building blocks for staircases and the Farey sequences and the Stern-Brocot tree [26]. For example, consider a staircase  $(\mathbf{23})^\infty$  made up of alternating  $\mathbf{2}^\infty = [1, 2]$  and  $\mathbf{3}^\infty = [1, 3]$  segments. To obtain the winding numbers of the resulting staircase, we take the mediant

$$\frac{1}{2} \oplus \frac{1}{3} = \frac{1+1}{2+3} = \frac{2}{5}.$$

This suggests that the stable staircase in the  $(2, 5)$  direction is  $(\mathbf{23})^\infty$ .

## 2.4 Discussion

This connection is surprising because it relates an equilibrium model—continuum percolation—with a far-from-equilibrium dynamical phenomenon—nonconserved coarsening. One naturally wonders what necessary characteristics a nonconserved coarsening process must possess to fall into this universality class of stripe state outcomes. Stripe states have similarly been observed in the majority vote model [27], the AB model [28], the naming game [28], and recently the confident voter model [29]. More detailed numerical work is needed on these models to accurately determine the probabilities of various coarsening outcomes. It would also be worthwhile to simulate the Toom model [30], in which each spin on a square grid interacts with only two of its neighbors along different directions (for example, a spin may interact with its neighboring spins above and to the right, but not with its neighboring spins below and to the left). Does this system also fall into our continuum critical percolation universality class?

Recent quantitative evidence from simulations linking continuum percolation models with both the early-time coarsening and the late-time outcomes of  $2d$  nonconserved coarsening is mounting. We hope that these remarkable results will ignite rigorous mathematical studies on the nature of this connection.

## Chapter 3

# Freezing in Three-Dimensional Ising Ferromagnets

Phase transitions have typically been studied in the equilibrium framework. Above a critical temperature  $T_c$ , a system shows no order, while below this critical temperature, the order parameter is nonzero. A recent interest has been in describing ordered states that arise below the critical temperature in a dynamical setting.

The prototypical model for studying phase transitions in statistical physics is the Ising model, which proved instrumental in understanding ferromagnetism. When endowed with a kinetics that does not conserve the magnetization, this becomes a Model A system in the classification of Hohenberg and Halperin [31]. In one dimension, the critical temperature is at  $T = 0$ . In two and higher dimensions, there is a finite critical temperature. In equilibrium, systems with  $T < T_c$  tend to order their spins, and a nonzero value of magnetization results. What happens if, instead, a system starting at an infinite temperature is rapidly quenched to  $T < T_c$ ? What is the final state following the quench, and what are the time scales involved in the approach to the final state?

Few answers to the above questions have been rigorously proven, with some exceptions for idealized one-dimensional models [5]. For  $d > 1$ , studies are typically based on simulations combined with approximate and heuristic arguments. Mathematical studies of spin systems generally focus on the  $T = 0$  limit where theorems can be proven. Most prior results

have supported the validity of a simple theoretical framework for understanding coarsening following a quench to zero temperature. This ‘central dogma’ of coarsening at  $T = 0$  can be summarized by the following statements:

- There exist two ground states of the system corresponding to the two possible values of the (scalar) order parameter. These ground states are the only possible final states of the evolution.
- The characteristic length scale of the coarsening domain mosaic grows in time as  $t^{1/2}$  [32, 5, 33, 4]. Thus one of the two possible final states is reached in a time that scales as  $L^2$ .
- The final states are frozen, since at  $T = 0$ , energy-raising moves are forbidden, and the system is stuck in one of the two ground states.

To test these predictions, we simulate the evolution of a kinetic Ising system when it is quenched from above to below the critical temperature. Phenomenologically, the system evolves by minimizing a coarse-grained Landau free-energy functional to determine its long-time state following a quench. However, this mean-field description represents a considerable oversimplification. Finite-range interactions in various models may support many metastable states, and the approach to equilibrium is generally not nearly as simple as any mean-field picture might suggest [34, 35].

In the one-dimensional Ising system, each pair of antialigned spins on the line represents a domain wall. The motion of domain walls is diffusive. When two domain walls meet, a larger domain forms, and the system coarsens. Thus the ultimate outcome of the dynamics for  $d = 1$  is always the ground state regardless of initial condition, so the central dogma provides an accurate description of the KIM in  $d = 1$ . For  $d > 1$ , starting from a state with excess positive (negative) magnetization, the final state after a quench to  $T = 0$  is generally believed to be the positive (negative) ground state with probability equal to one. This has been proven recently in the mean-field ( $d \rightarrow \infty$ ) limit [36].

In  $d = 2$ , the final state of the Ising system following a quench from  $T = \infty$  to  $T = 0$  however is not so simple [37, 7, 38, 39]. With probability  $\approx 1/3$ , the system gets stuck in an infinitely long-lived metastable state which consists of two (rarely more than two) stripes of opposite spin [15] (Fig. 1.2). Note that for one of the stripes to evaporate requires an energy-raising spin flip, but at  $T = 0$ , such moves are forbidden. Thus if a system coarsens into the state shown in Fig. 1.2, it becomes stuck there forever.

### 3.1 Quench of a Three-Dimensional Kinetic Ising Model to $T = 0$

In three dimensions, a quench from  $T = \infty$  to  $T = 0$  results in a bizarre final state, and the central dogma of coarsening completely fails. In stark contrast to the above predictions for coarsening at  $T = 0$ , we find:

- In the large-system limit, the probability of the system reaching one of the two ground states approaches zero. Instead, the system consists of two highly interwoven, topologically complex domains.
- While the majority of coarsening occurs in a time that scales as  $L^2$ , the relaxation time for the energy (and other observables) scales as  $\exp(L^2)$ .
- The final states are dynamic. There is always stochastic flipping of spins, even though the system has relaxed to a final state at  $T = 0$ .

We study the homogeneous, ferromagnetic Ising model defined by the Hamiltonian

$$\mathcal{H} = -J \sum_{\langle ij \rangle} \sigma_i \sigma_j$$

on a simple cubic lattice, with the interaction strength  $J$  set to 1.  $\sigma_i = \pm 1$  represents the spin at site  $i$ , and the sum is over all nearest-neighbor pairs of spins. We use periodic boundary conditions in all directions. Each realization begins with an antiferromagnetic



initial state. We experimented with both random and antiferromagnetic initial states, and while both give essentially the same results, except for minor quantitative differences in distributions of observables, the antiferromagnetic configuration is simpler. The system evolves starting at time  $t = 0$  by zero-temperature single-spin-flip dynamics, so that only energy-lowering spin flips are permitted. For computational efficiency, we employ the same kinetic Monte Carlo technique in our simulations as in Chapter 2. A single selected spin flips according to the update rule

$$\text{flipping probability} = \begin{cases} 1 & \text{if } \Delta E < 0, \\ p & \text{if } \Delta E = 0, \\ 0 & \text{if } \Delta E > 0, \end{cases}$$

with a single parameter  $p$ . Here we use  $p = 1/2$  which corresponds to zero-temperature Glauber dynamics [21], although the choice  $p = 0$ , corresponding to Metropolis dynamics [22], would have been more efficient. While the evolution is essentially the same for all  $p > 0$ , the case  $p = 0$  gives rise to a different final state with jammed configurations [40, 41]. These jammed configurations naturally arise in kinetically constrained models [42], which are used for studying glassy dynamics. Here we do not consider the case  $p = 0$ .

Starting at  $t = 0$  every spin in the lattice is flippable. We choose an eligible spin at random (a spin for which  $\Delta E \leq 0$  if that spin were to flip) and we apply the above update rule. There is initially a rapid drop in energy. After a time  $t = 5L^2$ , each realization has coarsened, and for large systems, almost all realizations are stuck in a “plumber’s nightmare” state (Fig. 3.3).

Running a realization of the  $3d$  Ising model to its final lowest-energy state following a quench to zero temperature with unbiased Glauber dynamics is prohibitively slow, even for small system sizes. For times beyond the coarsening time, which scales as  $L^2$ , the evolution is characterized by long periods of wandering through constant-energy configurations. Occasionally and at progressively later times, there are isolated energy-lowering spin-flip events (Fig. 3.1). In Figure 3.2, the average time interval between two successive energy-lowering

spin-flip events is plotted versus the average time for the  $n^{\text{th}}$  such energy-lowering spin-flip event to occur. The time between energy-lowering moves increases roughly exponentially over an appreciable time range.

To speed up the simulations, we devised an acceleration algorithm based on driving the system with a weak bias magnetic field so that the rare energy-lowering events happen more quickly. Our method is summarized as follows:

- i Glauber dynamics is applied until time  $t = 5L^2$ . This time is sufficiently beyond the coarsening time that energy-lowering events have become rare.
- ii At  $t = 5L^2$ , an infinitesimal bias magnetic field is applied. This forces zero-energy spins of one type (+ / -) to flip, while zero-energy spins of the opposite type (- / +) cannot flip.
- iii After each energy-lowering move, the sign of the bias field is reversed. This overall process allows energy-lowering moves to happen quickly.
- iv If no active spins remain while the bias field is applied in one direction, then the sign of the bias field is reversed. If, with the reversed bias field, there is again no drop in energy and no active spins remain, then the system has reached its final state.

Our acceleration algorithm drastically speeds up the zero-temperature dynamics of the  $3d$  KIM, and it accurately reproduces the final state if true Glauber dynamics had been run to the end of each simulation. For details on tests of the accuracy of our acceleration algorithm, see Appendix A.

We now describe the strange features of the plumber’s nightmare states in detail.

### 3.1.1 Final State Geometry

While it is possible that an Ising ferromagnet of size  $L^3$  quenched to  $T = 0$  reaches the ground state, this outcome is exceedingly rare as the system size  $L \rightarrow \infty$ . After the initial coarsening stage, the system almost always reaches a state with two—and only two—interpenetrating clusters of opposite spin. Two examples of typical final states are shown in

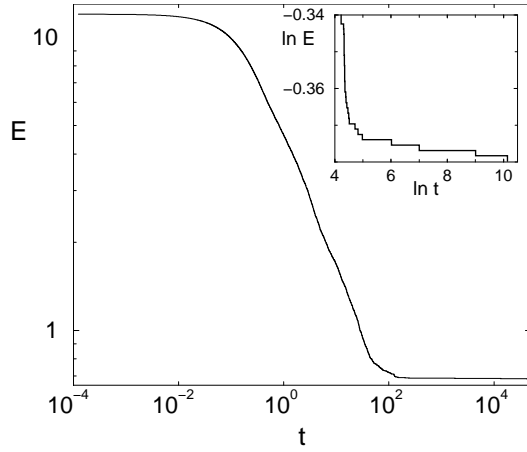


Figure 3.1: Time dependence of the energy for a single realization of an  $L = 20$  system quenched to  $T = 0$ . While the system settles into its final state at  $t \approx 41712$ , it features drops in energy at surprisingly late times (inset). Note that the abscissa of the inset is  $\ln t$ .

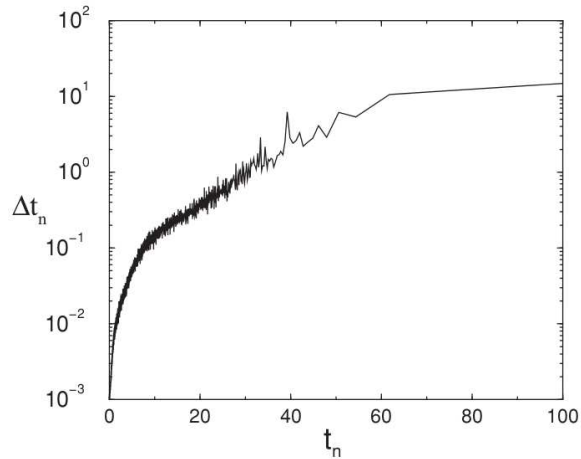


Figure 3.2: Configuration average of the time  $\Delta t_n$  between successive energy drops as a function of  $t_n$ , the average time at which the  $n^{\text{th}}$  such energy drop occurred, for 1024 realizations of a  $10 \times 10 \times 10$  system. The data are smoothed over a 100-point range.

Figure 3.3. For such a system to reach the ground state requires energy-raising spin flips, but at  $T = 0$  such moves are forbidden. Thus a system that collapses into a plumber's nightmare configuration at zero temperature is stuck there forever. (Detailed statistics on the final state are provided in Appendix B.)

Two important characteristics of the long-time state of a finite system are the energy

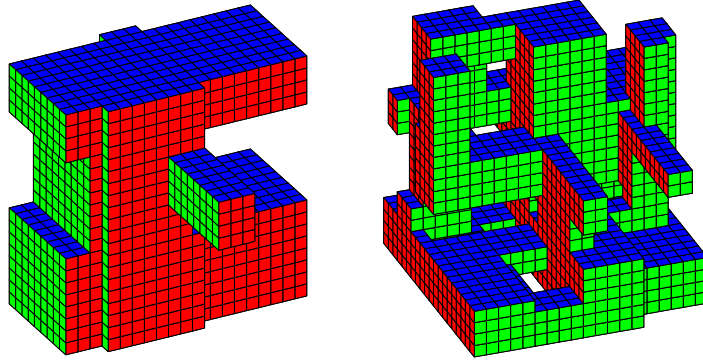


Figure 3.3: Examples of low-genus ( $g = 3$ ) and high-genus ( $g = 16$ ) domains on a  $20^3$  lattice.

and the genus. The energy  $E$  of a final state is proportional to the total number of bonds between unlike neighboring spins. (The ground state energy is set at zero.) The quantity  $E_L$  is the average energy  $E$  for a given system size  $L$ .  $E_L$  decays as a power law in  $L$ , but with substantial finite-size corrections. An extrapolation yields  $E_L \sim L^{-\epsilon}$ , with  $\epsilon \approx 1$ , in agreement with previous smaller-scale simulations [7]. This result implies that the surface area of domains in a final state of linear size  $L$  scales as  $L^2$ . The scaled energy distribution  $P(E/E_L)$  shows good data collapse (Figure 3.5(a)). It is defined by a peak that is close to being Gaussian, and a linear tail at low energies. Intriguingly, the linear tail only appears if the system begins in an antiferromagnetic initial state, and not for the random initial state. We do not have an explanation for this minor difference in final energy distributions between the two initial conditions.

In the long-time state, spin domains are topologically complex. Geometrically, the spin clusters bear a resemblance to complex geometrical structures that arise naturally in two-phase micellar systems [43]. (These topologically complex final states arising from the Ising model quench are the analogues of zero-mean-curvature surfaces in TDGL evolution [44, 45]. Subtle differences between microscopic dynamics and macroscopic (curvature-driven) flow will be presented later.) One way to characterize this complexity is through the genus  $g$  of a domain. Mathematically, the genus is the maximum number of cuts that can be made along

nonintersecting closed simple curves on the surface without disconnecting the manifold. The genus is related to the Euler characteristic  $\chi$  of a surface and can be calculated by enumerating simple features of the interface [46].

$$\chi = 2(1 - g) = \mathcal{V} - \mathcal{E} + \mathcal{F} \quad (3.1)$$

Here,  $\mathcal{V}$  is the number of vertices on the interface,  $\mathcal{E}$  is the number of edges, and  $\mathcal{F}$  is the number of faces. As elementary examples, the genus of a sphere is 0, and the genus of a donut is 1. To illustrate, consider an isolated cube. The cube has 8 vertices, 12 edges, and 6 faces, so its genus is 0. (This is expected, since a cube is topologically equivalent to a sphere.) For further example, consider a linear  $2 \times 1$  filament that wraps around a  $2^3$  lattice. A simple calculation gives  $\mathcal{V} = 8$ ,  $\mathcal{E} = 16$ , and  $\mathcal{F} = 8$ , corresponding to  $g = 1$ . Note that the length scale of the discretization does not change the value of  $g$ . Now consider Figure 3.4. The image on the left is a cluster that wraps periodically in two Cartesian directions, for which  $\mathcal{V} = 8$ ,  $\mathcal{E} = 20$ , and  $\mathcal{F} = 10$ , corresponding to  $g = 2$ . For the cluster on the right which wraps periodically in all three Cartesian directions,  $\mathcal{V} = 8$ ,  $\mathcal{E} = 24$ , and  $\mathcal{F} = 12$ , corresponding to  $g = 3$ .

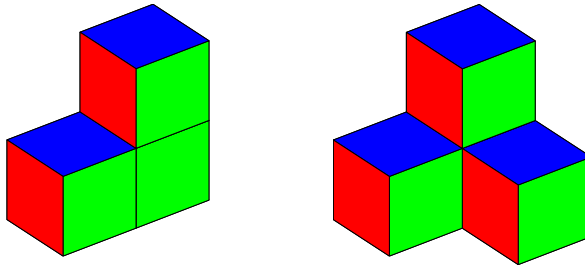


Figure 3.4: Simple examples of interfaces with genus  $g = 2$  and  $g = 3$  for a periodic  $2 \times 2 \times 2$  system.

To measure the topology of the final state, we first identify all spin clusters using a cluster multilabeling algorithm [47]. The final state almost always consists of just two interpenetrating clusters. Spin configurations with more than two clusters do occur—although

rarely—for the finite systems we studied (see Appendix B). The largest number of clusters we observed in the final state of a realization was seven. This occurred for a  $38^3$  system in which there were six narrow filaments of one phase in a background of the opposite phase. However in the  $L \rightarrow \infty$  limit, the probability of observing greater than two clusters or only one cluster in the final state approaches zero.

Once all spin domains are labeled, we enumerate the numbers of vertices, edges, and faces for each domain. The value of  $\mathcal{F}$  is easily computed from the total energy of the system, since each pair of antialigned spins represents a face. For each face, we add the numbers of vertices and edges on the face to their total counts, making sure to not overcount a vertex or edge that was already counted as part of another previously-encountered face. If the final state contains only two clusters, then the two clusters by definition share the same surface area, so they have the same genus. If there are more than two clusters, then the largest genus among all clusters is taken to be the genus of the lattice.

As for the average energy  $E_L$ , the average genus  $\langle g \rangle$  shows power-law behavior in  $L$  in the large-system limit, but with finite-size corrections. An extrapolation to  $L \rightarrow \infty$  yields  $\langle g \rangle \sim L^\gamma$ , with  $\gamma \approx 1.7$ . The final genus distribution also shows good scaling in the variable  $g/\langle g \rangle$  (Fig. 3.5(b)). The high-genus tail of the distribution decays approximately exponentially.

Through basic topological considerations, the energy and genus of a system are related. First, note that each face on a cluster is bounded by four edges, and each edge on a cluster is shared between two faces. Thus

$$\mathcal{E} = 2\mathcal{F}.$$

Similarly, each edge on a cluster is bounded by two vertices, and each vertex on a cluster is shared among three, four, five, or six edges. This leads to the inequality

$$\frac{\mathcal{E}}{3} \leq \mathcal{V} \leq \frac{2\mathcal{E}}{3}.$$

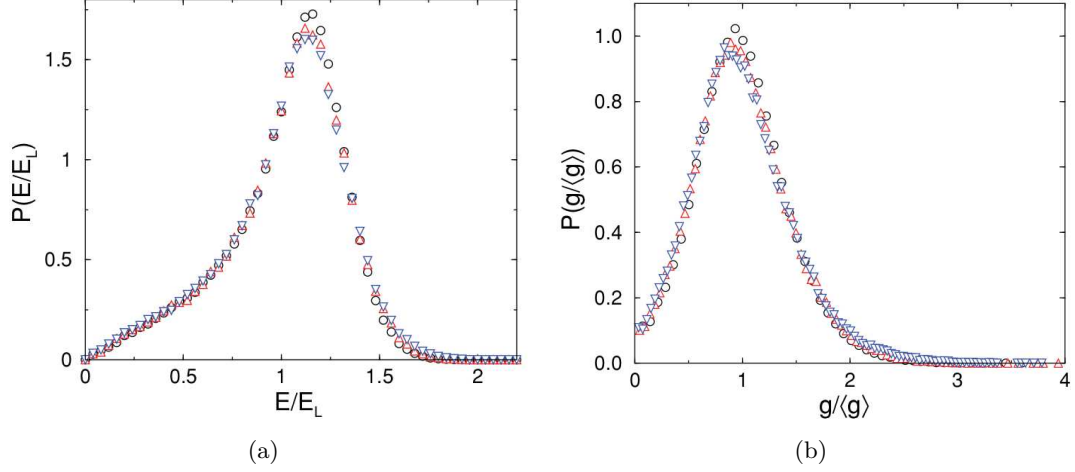


Figure 3.5: The final-state energy (a) and genus (b) distributions for  $L = 54$  ( $\circ$ ),  $L = 76$  ( $\triangle$ ), and  $L = 90$  ( $\nabla$ ).

Plugging these two relations into Eq. (3.1), we obtain

$$\frac{-\mathcal{F}}{3} \leq \chi \leq \frac{\mathcal{F}}{3}.$$

We then use the stronger upper bound  $\chi \leq 2$  to obtain

$$0 \leq g \leq \frac{\mathcal{F}}{6} + 1. \quad (3.2)$$

Note that the total number of faces  $\mathcal{F}$  is directly related to the energy, viz.  $\mathcal{F} \propto L^3 E_L$ .

Finally, assuming that the value of  $g$  for a realization is typically about halfway between its upper and lower bounds, we obtain the exponent inequality

$$\epsilon + \gamma \leq 3. \quad (3.3)$$

Our measured values  $\epsilon \approx 1$  and  $\gamma \approx 1.7$  are consistent with Eq. (3.3).

One may further relate the genus of a domain with the types of vertices on the domain's surface. Let  $\mathcal{V}_m$  denote the number of vertices of degree  $m$ , with  $m = 3, 4, 5$ , or  $6$ . As shown in Figure 3.6, the degree of a vertex equals the number of edges joining at that vertex.

The ‘defect’ of a vertex is defined to equal the difference between the sum of the angles of all faces at the vertex and  $2\pi$ . Thus, one sees that the defects of vertices of degrees 3, 4, 5, and 6 are  $\pi/2$ , 0,  $-\pi/2$ , and  $-\pi$ , respectively. Further, the discrete extension of the Gauss-Bonnet theorem states that the sum of all defects on the domain surface equals  $2\pi\chi$ . Thus we arrive at

$$\frac{\pi}{2}\mathcal{V}_3 - \frac{\pi}{2}\mathcal{V}_5 - \pi\mathcal{V}_6 = 2\pi\chi = 4\pi(1 - g),$$

so the genus of a domain can be calculated from

$$g = 1 + \frac{1}{8}(2\mathcal{V}_6 + \mathcal{V}_5 - \mathcal{V}_3).$$

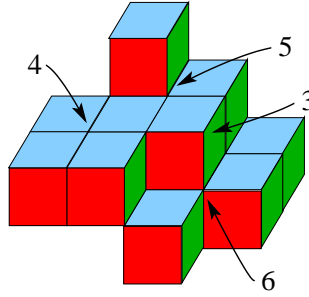


Figure 3.6: A sample portion of a domain interface showing vertices of degrees 3, 4, 5, and 6.

### 3.1.2 Blinker States

When one thinks of the long-time state of a physical system at  $T = 0$ , one generally regards all components of the system as ‘frozen’, since there are no thermal agitations from the environment. While a quench of a two-dimensional Ising ferromagnet to  $T = 0$  may result in a ‘stripe state’, such states are indeed frozen. For a  $2d$  system that has reached a stripe configuration, there are no remaining possible spin flips. The outcome of a quench to  $T = 0$  is quite different in  $d = 3$ , where the non-trivial final states that result are in general *not* static, but contain a small subset of ‘blinker’ spins. These blinker spins have three up neighbors and three down neighbors. Since each blinker spin is in a zero-energy state, it is



capable of flipping at  $T = 0$ . When one blinker spin flips, one (or more) of its neighboring spins typically become blinkers, so that even in the  $t \rightarrow \infty$  limit, these blinker spins never cease to exist.

As a visual example of a blinker state in  $3d$ , consider Figure 3.7. The three bounding slabs wrap periodically in the three coordinate directions, so their boundaries are merely visual artifacts. The zero-energy spins at inner and outer corners in the region where the three slabs join are ‘blinker spins’. In the fully-deflated state (left image), there is one spin (not colored) in the innermost corner where the slabs intersect that is capable of flipping. In the fully-inflated state (right image), the single colored spin at the corner can flip. Blinker states typically exist between these extremes so that the blinker lives in the half-inflated state (middle image). Note that, if this system is at zero temperature, there must always be at least one blinker spin in the system.

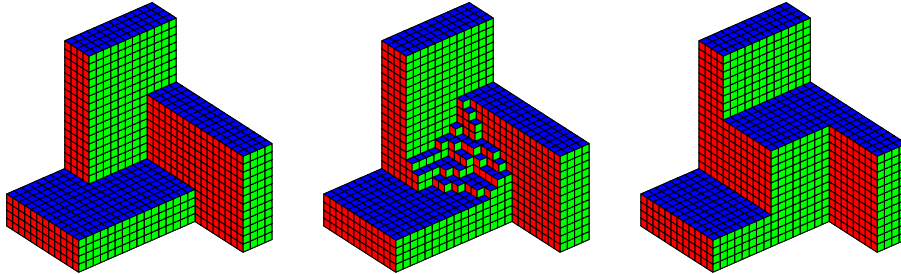


Figure 3.7: An  $8^3$  blinker on a  $20^3$  cubic lattice, showing the fully-deflated state (left), an intermediate state (middle), and the fully-inflated state (right). The bounding slabs wrap periodically in the three Cartesian directions.

While Figure 3.7 may seem idealized, blinker states are ubiquitous in Ising ferromagnets following a deep quench. The requirement for a lattice supporting blinker states is that the linear lattice size  $L \geq 5$ . As  $L$  increases, essentially *all* realizations end up with blinkers; thus the final states are in general non-static (Fig. 3.7). Figure 3.8 shows a real blinker state following a quench to zero temperature.

The fraction of total spins that are blinkers in the final state at any given time is small; typically around  $3 \times 10^{-3}$  to  $4 \times 10^{-3}$  when the system size  $L \lesssim 50$ . The number of

blinker spins fluctuates in time in any given realization, and therefore is not a meaningful characteristic. To characterize blinker states, we define a ‘blinker region’ to be a subset of spins in the lattice that are capable of being blinkers. The corresponding ‘blinker volume’ is the total percentage of the lattice that is accessible to blinker spins. Once a given realization has reached its final state, the total blinker volume for that realization is fixed in time. Consider again Figure 3.7. The left and right lattices contain only one blinker spin, while the middle lattice has many blinker spins. The  $8 \times 8 \times 8$  region bounded by the confluence of the three stationary slabs is the blinker region of this system. The blinker volume is  $8^3 = 512$  spins, although the actual number of blinker spins in the system at any given time is much smaller.

The blinker volume in Figure 3.7 can be determined visually, but we need a systematic way of numerically probing the blinker volume. Consider Figure 3.7 (middle image). For illustration, let the colored cubes indicate ‘up’ spins, while empty space corresponds to ‘down’ spins. If one applies a bias magnetic field in the ‘up’ direction, then all flippable down spins in the blinker region will flip, until the entire blinker region is filled with up spins (right image). Denote this spin configuration  $\mathcal{C}_+$ . Starting again from the middle image, if one applies a bias magnetic field in the ‘down’ direction, then all flippable up spins will flip, and one is left with the left image, whose configuration is denoted  $\mathcal{C}_-$ . Taking the difference in spin configurations  $|\mathcal{C}_+ - \mathcal{C}_-|$  (and dividing by two), one is left with the blinker volume of the system. We apply this procedure to numerically measure the blinker volume of many independent realizations following a quench. The blinker volume in the final state is typically around 9%—a macroscopic fraction of the lattice.

### 3.1.3 Ultra-Slow Relaxation

As described thus far, the evolution of a quenched three-dimensional Ising ferromagnet is far richer than one would naively expect. Two major aspects of the long-time state, namely (i) topologically-complex domains and (ii) non-static blinker configurations, are completely neglected by the Ginzburg-Landau coarse-grained description of the Ising model. We now

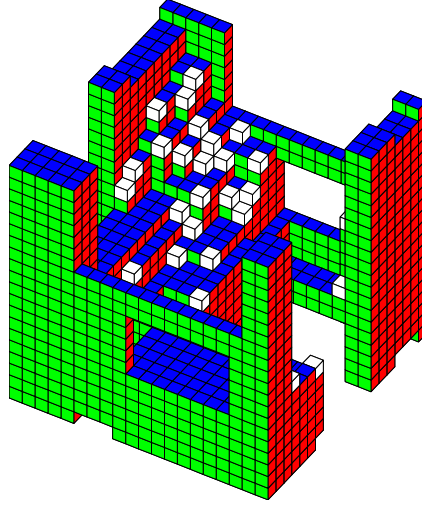


Figure 3.8: Example of a blinker state on a  $20^3$  lattice with periodic boundaries. The highlighted blocks indicate blinker spins.

describe another major counterintuitive aspect of a deep quench.

Starting from an antiferromagnetic (or random) initial spin state, one may consider how long it takes for the  $3d$  system to relax to its final configuration. By ‘final configuration’, we refer to the state of the spin system after it has reached its lowest value of energy. As shown above, systems quenched to  $T = 0$  in general do not reach the ground state, but end up being frozen in a domain configuration for which  $E > 0$ .

Specifically, we consider the ‘survival probability’  $S(t)$ , which is the probability that a given realization of the dynamics is still decreasing in energy at time  $t$  following the quench. Since energy-lowering spin-flip events occur less frequently at long times, it is not immediately obvious whether the system has reached its lowest value of energy. To measure  $S(t)$ , we devised an algorithm to test whether any additional drops in energy are possible at long times following the quench. Starting from time  $t = 0$ , we track the numbers of positive-energy and zero-energy flippable spins in the system. The former will systematically decrease as the system coarsens. When there are no remaining positive-energy flippable spins, it is possible that the system has reached its asymptotic value of energy. Let  $\mathcal{C}_0$  denote the spin configuration and  $\mathcal{T}_0$  the time at which no positive-energy

flippable spins remain. We then proceed as follows:

- i Starting from  $\mathcal{C}_0$ , an infinitesimal bias magnetic field is applied to the system. This forces only up (down) flippable spins to flip. If a drop in energy occurs in the presence of the bias field, then the system has not reached its asymptotic value of energy. The system is returned to  $\mathcal{C}_0$  and subsequently evolves by zero-temperature Glauber dynamics without a bias field until the number of positive-energy spins again reaches zero, and a new candidate final state  $\mathcal{C}_0$  and time  $\mathcal{T}_0$  are reached.
- ii If the number of flippable spins reaches zero without a drop in energy, then the sign of the infinitesimal bias field is reversed, which forces only down (up) flippable spins to flip. If a drop in energy occurs, then the system is returned to  $\mathcal{C}_0$  and subsequently evolves without a bias field until a new candidate final state  $\mathcal{C}_0$  and time  $\mathcal{T}_0$  are reached.
- iii If the bias field is applied in both directions without a drop in energy, then the system has reached its asymptotic value of energy.  $\mathcal{T}_0$  is the survival time of the system.

We calculate the survival time  $\mathcal{T}_0$  for many realizations, from which we infer the survival probability  $S(t)$  (Figure 3.9). Surprisingly, the time scale for the energy relaxation is many orders of magnitude larger than the coarsening time, even for small systems. For example, for lattices of size  $L = 10$ , 40 out of  $10^7$  realizations had not relaxed to their asymptotic energy by  $t = 10^9$ . For  $L \gtrsim 20$ ,  $S(t)$  is reasonably smooth. Plotting  $S(t)$  versus  $\ln t$  on a double logarithmic scale, the data is approximately fit by

$$S(t) \sim (\ln t)^{-\sigma}, \quad \sigma \approx 3. \quad (3.4)$$

Related aspects of slow domain coarsening in the homogeneous kinetic Ising model [48] and in the kinetic Ising model with competing ferromagnetic and antiferromagnetic interactions [49] has been found previously. Yet the extremely slow energy relaxation seen in the *zero-temperature* KIM is bizarre. The domain structure and topology form in a time that scales only as  $L^2$ . Also, at  $T = 0$ , only energy-preserving and energy-lowering spin

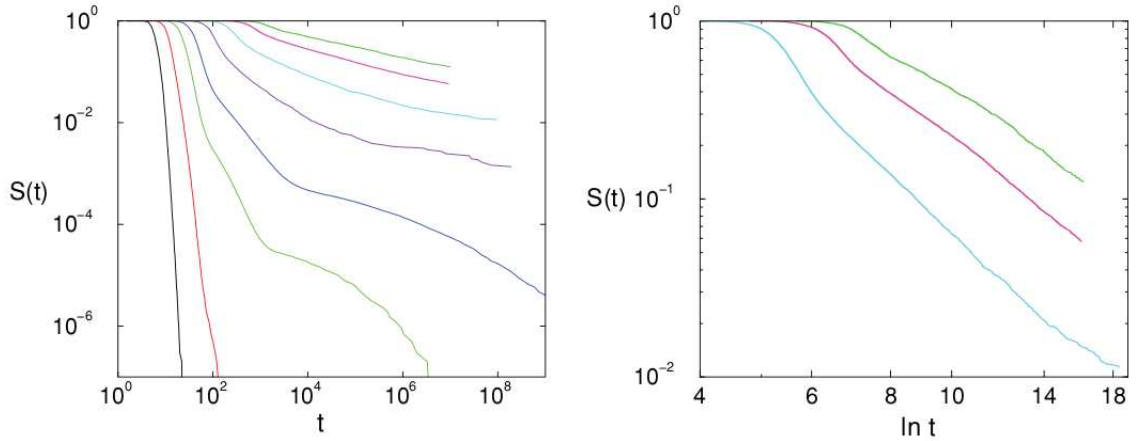


Figure 3.9: (left image) Survival probability  $S(t)$  versus time  $t$ . Data is based on  $10^7$  realizations for  $L = 4, 6, 8,$  and  $10$ , 10240 realizations for  $L = 14, 20,$  and  $30$ , and 2048 realizations for  $L = 40$  (lower left to upper right). (right image)  $S(t)$  vs.  $\ln t$  for  $L = 20, 30,$  and  $40$  (lower left to upper right) on a double logarithmic scale. The data is reasonably fit by the inverse logarithmic dependence Eq. (3.4).

flips are permitted. Thus one would expect the asymptotic value of energy to be reached quickly.

To understand the anomalously slow energy relaxation seen in  $S(t)$ , consider again the blinker state shown in Fig. 3.7. The number of blinker spins on the interface of the blinker and the types of blinker spins (inner or outer corners, i.e. up/down spins) vary with different configurations of the blinker interface. If the blinker is mostly deflated, then there are more inner corners than outer corners on the blinker interface. Thus on the next update event, it is most probable that a spin at an inner corner will flip. Similarly, a mostly-inflated blinker will have an excess of outer corners. On the next update event, it is most likely that a spin at an outer corner will flip. The mismatch in numbers of inner and outer corners (up/down spins) on the interface for different blinker configurations tends to drive the blinker interface toward the half-inflated state (middle panel of Fig. 3.7).

Now consider the  $\ell \times \ell$  two-dimensional analog of a blinker state. This is the growth model proposed in [50] except with the two edges of the interface fixed in position (Fig. 3.11). Starting from the fully-deflated state (right panel), one may ask: What is the mean first-

passage time to reach the fully-inflated state (left panel). The blinker initially fills out quickly to reach the half-inflated state (middle panel). To make it from the half-inflated state to the fully-inflated state, the blinker must work against an effective bias due to the mismatch in the numbers of inner and outer corners on the interface. Note that the typical interface velocity is given by the difference in numbers of inner and outer corners on the interface, so we estimate  $v_2 \sim N_- - N_+ = -1$  in two dimensions. The effective diffusion coefficient of the interface motion is proportional to the mean-square displacement of the interface in a single time step, which is proportional to  $\ell$ . Thus we infer  $D_2 \sim \ell$ . The interface must advance a distance of order  $\ell^2$  to reach the fully-inflated state:  $\Delta x_2 \sim \ell^2$ . With these three estimates, the dominant Arrhenius factor [51] for the time to reach the fully-inflated state is given by

$$\ln \tau_2 \sim \frac{v_2 \Delta x_2}{D_2} \sim \ell. \quad (3.5)$$

This analysis may be repeated for a real  $\ell \times \ell \times \ell$  blinker in three dimensions. The difference in numbers of up/down spins on the interface is now of order  $\ell$ , giving  $v_3 \sim N_- - N_+ \sim \ell$ . The mean-square displacement of the interface in one time unit is of order  $\ell^2$ . Also, on the order of  $\ell^3$  spins must flip for the 3D blinker to reach the fully-inflated state. Thus we estimate the time to reach the fully-inflated state in three dimensions to be given by

$$\ln \tau_3 \sim \frac{v_3 \Delta x_3}{D_3} \sim \ell^2. \quad (3.6)$$

Generally in  $d$  dimensions, the time for a  $d$ -dimensional blinker of linear size  $\ell$  to reach the fully-inflated state satisfies

$$\ln \tau_d \sim \ell^{d-1}.$$

We numerically tested our predictions for the first-passage times  $\tau_2$  and  $\tau_3$  (Fig. 3.10). For the idealized  $2d \ell \times \ell$  blinkers, we simulated blinkers with  $2 \leq \ell \leq 14$ , and the exponential fit (3.5) shows excellent agreement with data. We also simulated  $3d$  blinkers with  $2 \leq \ell \leq 5$ . The data for very small blinkers is qualitatively consistent with our prediction (3.6).

The salient point is that the time for a half-inflated blinker to reach its fully-inflated

state grows rapidly with the linear blinker size  $\ell$ . Intriguingly, it may be possible to compute the asymptotic form of the amplitudes in Eqs. (3.5) and (3.6), since there are connections between blinker states and the entropies of random tilings [52]. For example, for the two-dimensional blinkers (Fig. 3.11), the asymptotically exact evaporation time may be given by  $\ln t = aL$  with  $a = 2 \ln 2 \approx 1.386$ , which is in excellent agreement with our (limited) numerical data.

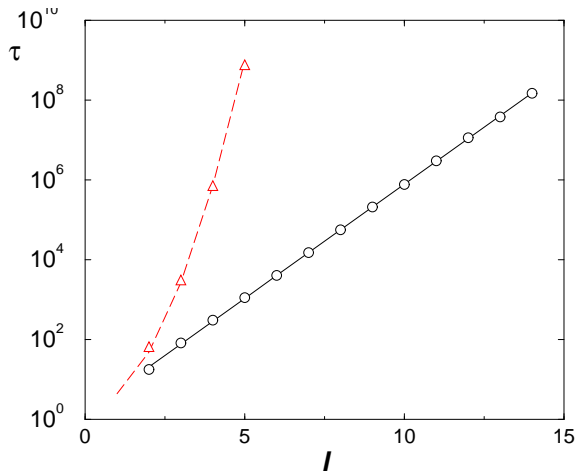


Figure 3.10: First-passage time for a fully-deflated blinker to reach the fully-inflated state in two ( $\circ$ ) and three ( $\triangle$ ) dimensions. The fit to the two-dimensional data is  $\tau_2 = 1.40 \exp(1.33 \ell)$ . The curve overlaying the three-dimensional data,  $\tau_3 = 3 \exp(0.8 \ell^2)$ , is a guide for the eye.

We have identified an extremely long time scale in the dynamics of a single blinker state in three dimensions: the typical inflation time. But all configurations of a particular blinker state have the same energy. To understand the ultra-slow energy relaxation seen in a quench to  $T = 0$ , consider two blinker states as shown in Fig. 3.7 that are oppositely oriented so that when each blinker is in its half-inflated state (middle panel), the blinkers do not touch. However, when both blinkers are in their fully-inflated states, they just overlap corner-to-corner. In the rare event that both blinkers are simultaneously inflated, there is an energy-lowering spin-flip event. The two adjacent blinkers subsequently merge. Due to the finite (though astronomically long) lifetime of such a two-blinker arrangement, we term this a ‘pseudo-blinker’ configuration. Since the average time for a single blinker to become inflated

is extraordinarily long, energy-lowering pseudo-blinker coalescence events are responsible for the remarkably slow relaxation seen in a quench of a real Ising ferromagnet. A schematic illustration of a pseudo-blinker coalescence event is shown in Fig. 3.12.

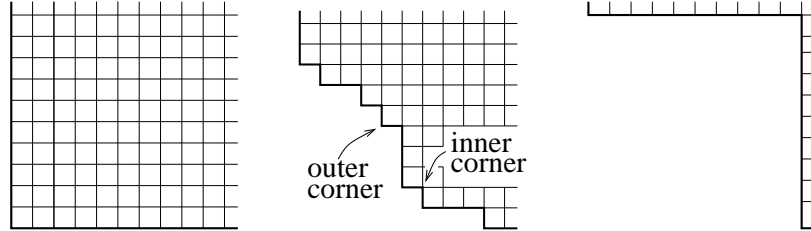


Figure 3.11: Two-dimensional analog of the blinker states in Fig. 3.7.

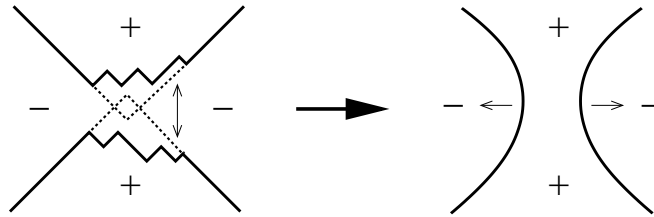


Figure 3.12: Schematic two-dimensional illustration of a blinker coalescence event.

### 3.1.4 Effects of the Initial Condition

The data presented above is for the quench of a 3D Ising ferromagnet to zero temperature starting from an antiferromagnetic initial condition. The other natural choice is to start with a random initial spin configuration, corresponding to infinite initial temperature. We emphasize that all of our central results outlined in this section also hold when starting from an infinite temperature initial state. We do however observe minor quantitative differences in distributions of observables depending on the choice of initial condition. Consider, for example, the final magnetization and energy distributions at  $T = 0$  starting from the antiferromagnetic versus random initial spin states (Figure 3.13). Note that the magnetization distribution is more strongly peaked about zero with the random initial condition, signaling that the system is more likely to become trapped in topologically-complex metastable states



when starting from infinite temperature. It is unclear why the magnetization distribution is narrower when starting from random initial condition.

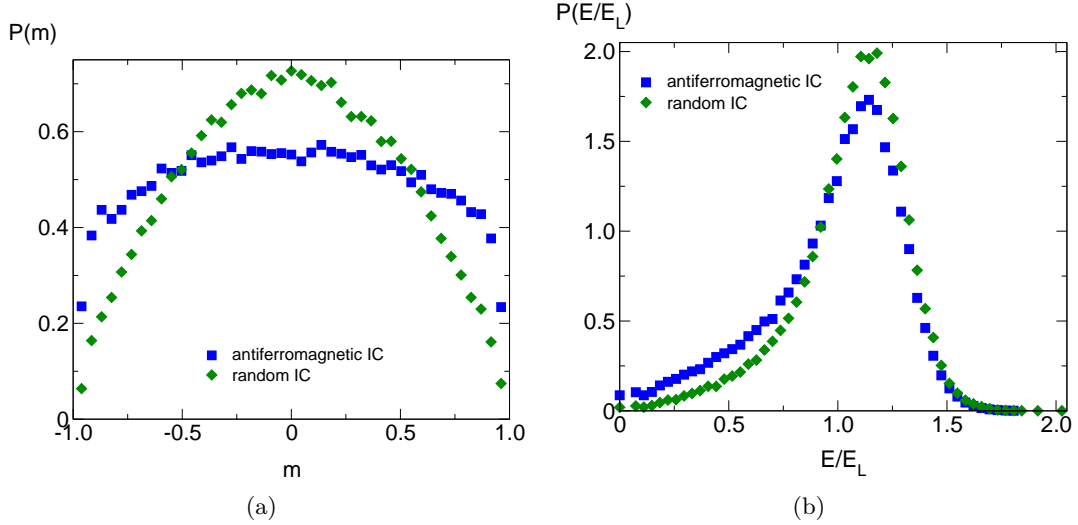


Figure 3.13: The final-state magnetization (a) and energy (b) distributions for  $L = 32$  using antiferromagnetic and random initial conditions. The two initial conditions seem to produce different distributions of observables, even in the  $L \rightarrow \infty$  limit.

### 3.1.5 Non-Cubic Geometries

What if we quench the  $3d$  KIM on a noncubic  $L \times L \times aL$  lattice? We still observe pinning of clusters at  $T = 0$ , but the number of clusters in a realization typically grows as the lattice becomes compressed in one or two directions. If  $a$  is small, then there are typically many clusters that percolate along the short axis, leading to pictures that resemble Swiss cheese (Fig. 3.14(left)). If  $a$  is large, then tiny beads form along the long axis (Fig. 3.14(right)). Clearly, clusters are able to percolate most easily along the short axes.

## 3.2 Quench of a Three-Dimensional Kinetic Ising Model to $T > 0$ : The Approach to Equilibrium

These counterintuitive results cannot be obtained from any mean-field description; they are consequences of the nearest-neighbor interactions between spins on the cubic lattice.

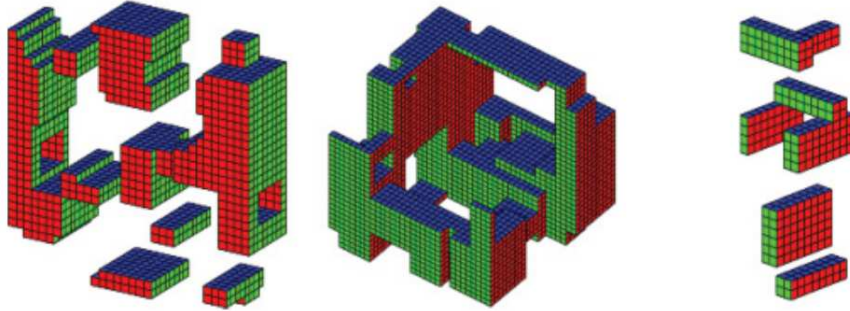


Figure 3.14: Example long-time states of a  $32 \times 32 \times 8$  system (left), a  $32 \times 32 \times 32$  system (center), and a  $32 \times 8 \times 8$  system (right).

Yet the zero-temperature Ising system is a highly idealized model of ferromagnetism and just one of many simple models featuring non-conserved order parameter coarsening. One naturally asks: Do any of the bizarre features of the zero-temperature quench of a  $3d$  Ising model also appear in other models of coarsening?

We next consider the three-dimensional KIM quenched to finite subcritical temperature. We employ a rejection-free Glauber dynamics in which each of the  $N_i$  spins in the system with energy  $E_i$  is selected to flip with relative probability  $P_i = N_i/(1 + e^{\Delta E_i/T})$ , where  $\Delta E_i$  is the energy change that would result if a spin with energy  $E_i$  is flipped. After each update, the time is incremented by  $\Delta t = 1/(\sum_i P_i)$ .

For the quench of an Ising model to  $T = 0$ , we used the antiferromagnetic initial condition for simplicity, although both antiferromagnetic and random initial conditions give essentially the same zero-temperature final state. Here we employ the random initial condition (with magnetization fixed at zero) to study the quench of an Ising ferromagnet to finite temperature. The random initial state corresponds to infinite initial temperature and adds realism to the problem.

We now ask: Starting from the random initial state, how does the system evolve at subcritical quench temperature? At zero temperature in any dimension  $d \geq 3$ , a system that is stuck in a plumber's nightmare geometry remains stuck forever with  $E > 0$ . At any positive quench temperature, the system must ultimately relax to equilibrium. Yet as we

will see, the approach to equilibrium is both nontrivial and slow, with the energy relaxation showing very different behavior at different time scales in the evolution.

As for the zero-temperature quench, the dynamics is not self-averaging, so we average our measurements over many realizations to learn of the typical approach to equilibrium. The simulations are quite messy and difficult to rigorously quantify. Furthermore, we restrict our study to quench temperatures  $T \leq T_C/2$ , which is below the roughening temperature  $T_R \approx 0.54401(1)T_C$  [53] for the  $3d$  Ising model. This ensures that the domain interfaces have finite width as the system size  $L \rightarrow \infty$ . We obtained a general picture of how the  $3d$  ferromagnet relaxes to equilibrium by defining roughly four stages in the evolution, which we now describe.

### 3.2.1 Stage I: Coarsening

Immediately following the quench, the Ising-Glauber system begins coarsening into a mosaic of oppositely-oriented spin domains. During a time interval  $t \lesssim L^2$ , domains are small and their linear scale grows in time as  $r \sim \sqrt{t}$ . By symmetry, the densities of up and down spins during the initial coarsening regime remain roughly equal.

The energy of the system decays smoothly at early times. In the absence of an external magnetic field, the total energy of a ferromagnet is proportional to the surface area between domains of up and down spins. Consider that there are  $N$  distinct spin clusters, and each cluster has surface area  $A \sim r^2 \sim t$ . For any finite-size system regardless of boundary conditions, the number of spin clusters  $N$  scales inversely with the volume  $V \sim r^3 \sim t^{3/2}$  of a typical cluster. This gives the energy of the system as [35]

$$E(t) - E_{\text{eq}} \sim NA \sim t^{-1/2}.$$

This predicted energy dependence on time agrees well with simulations at early times.

### 3.2.2 Stage II: Plumber’s Nightmare

After a time  $t \gtrsim L^2$ , the typical domain size  $r$  has reached the system size  $L$ . In general and for low enough quench temperatures ( $T \lesssim T_C/4$ ), the system is stuck in a metastable state similar to those states found in the zero-temperature quench, and the typical coarsening with smooth energy relaxation is interrupted. For any dynamical evolution rule that satisfies detailed balance, the system is driven to and transitions rapidly among the many equilibrium states, so finite-temperature plumber’s nightmare configurations are unstable. Nonetheless, gyroid phases play an observable role in the finite-temperature relaxation because they evaporate slowly, on a time scale much longer than the coarsening time. Fig. 3.15 shows a gyroid phase that developed following a quench to  $T = T_C/8$ .

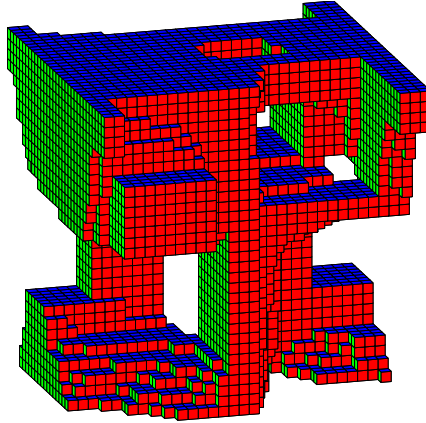


Figure 3.15: A genus  $g = 10$  sponge-like topology at time  $t = 1024$  for a quench of an  $L = 32$  system to  $T = T_C/8$ . We ran this realization until the energy first reached the numerically-measured equilibrium value of energy for this system size and temperature. This realization reached equilibrium at time  $t \approx 10^5$ —roughly two orders of magnitude longer than the coarsening time.

Of course the exact nature of these finite-temperature metastable states will depend strongly on the quench temperature. For quenches to  $T = \epsilon$  ( $\epsilon \ll T_C$ ), thermal fluctuations play a negligible role, and the characteristics of the metastable states that develop shortly after a quench (energy, genus, etc.) are essentially the same as for a zero-temperature quench. For quenches to  $T = T_R - \epsilon$ , thermal agitations are sufficiently large that systems

do not get trapped in plumber’s nightmare geometries.

Once a system reaches a finite-temperature gyroid phase, its energy begins decreasing slowly and in discrete steps (Fig. 3.16). Intuitively, the various interpenetrating “arms” that constitute the spin domains must evaporate one-at-a-time. Consider Fig. 3.17(a), which shows an  $\ell \times \ell \times L$  bar of “up” spins that joins another  $L \times \ell \times \ell$  bar of “up” spins, all in a background of “down” spins. To understand the energy relaxation shown in Fig. 3.16, note that it is energetically favorable that a spin on the edge of the bar flips before any lower-energy spin flips (Fig. 3.17(b)). The newly-created corner spins are now in a zero-energy environment and freely diffuse (Fig. 3.17(c)). It is most probable that these excitations will just recombine, and the system will quickly return to the configuration shown in Fig. 3.17(a). If a second energy-raising flip occurs on an edge (Fig. 3.17(d)), then another  $1 \times 1 \times L$  column of spins is able to diffuse. Now consider the bar after  $\ell$  independent nucleation events that occur in succession (Fig. 3.17(e)). What was formally a  $1 \times \ell \times L$  slab of spins on the front surface of the bar is now two disjoint slabs, each able to recede separately until the system reaches the new configuration with a bar of dimensions  $(\ell - 1) \times \ell \times L$  (Fig. 3.17(f)). This nucleation and subsequent rapid erosion of an arm of a plumber’s nightmare state corresponds to one of the discrete energy drops shown in Fig. 3.16.

To quantify this discrete energy relaxation, we compute three quantities: the total number  $N(t)$  of discrete energy drops that have occurred by time  $t$ , the average size  $S(t)$  of each energy drop up to time  $t$ , and the average time interval  $T(t)$  between energy drops up to time  $t$ . Our results for a quench to  $T = T_C/8$  are plotted in Fig. 3.18.

These plots reveal that: (a) the discrete energy drops shown in Fig. 3.16 become less frequent as the evolution progresses in time, and (b) the size ( $|\Delta E|$ ) of each energy drop decreases (on average) in time. Although our data plotted here are for specific values of system size and temperature, we verified that these plots look essentially the same for a range of subcritical temperature values. Perhaps most striking is that the average time between discrete energy drops versus time is described excellently by a linear fit over a wide

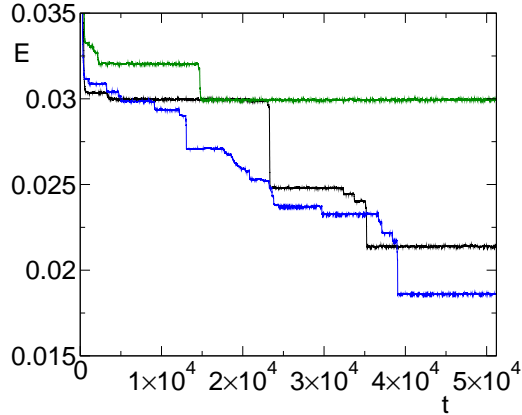


Figure 3.16: Energy versus time for three independent realizations of a quench to  $T = T_C/8$  for a  $32^3$  system. Energy is scaled so that the antiferromagnetic state energy is equal to 1, and the ground state energy is equal to 0.

range of times.

### 3.2.3 Stage III: Slab State

At long times in the evolution, a system may get trapped in a state with two coexisting phases, each domain being in local thermodynamic equilibrium and having zero mean curvature on its interface (Fig. 3.19(a)). We term such a configuration a “slab state”. These slab states are the three-dimensional analogues of the stripes seen in the quench of a two-dimensional ferromagnet. Yet  $3d$  slab states occur more rarely than their  $2d$  counterparts, with only a fraction 0.077(2) of realizations quenched from infinite temperature to  $T = T_c/2$  getting trapped in slab geometries (Fig. 3.19(b)). We were unable to accurately determine the slab state probability for quench temperatures  $T < T_c/2$  due to computational limitations. While a quench of a  $3d$  TDGL system to  $T = 0$  also gives rise to slab states, the probability of getting trapped in a slab, 0.054(2), differs significantly with that for the  $3d$  Ising-Glauber system. The salient point is that while slab states in  $3d$  resemble stripe states in  $2d$ , there is no longer universality in the probability of reaching these outcomes.

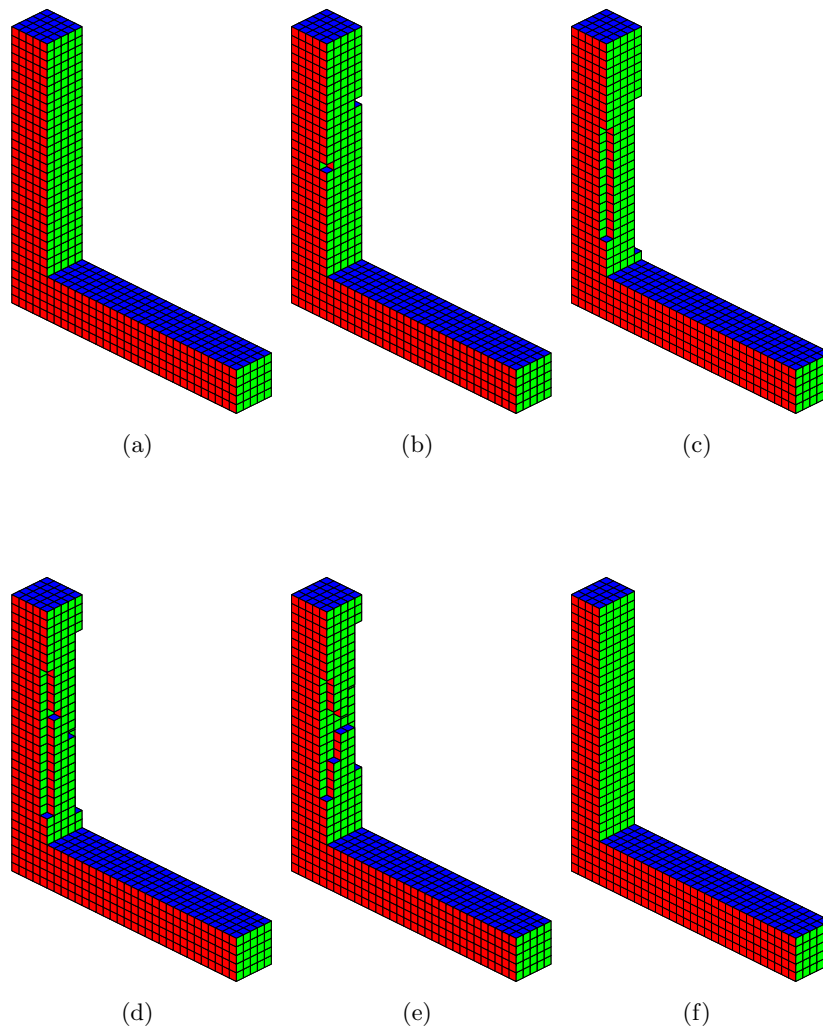


Figure 3.17: A two-arm state evaporating in the 3d KIM at finite temperature.

### 3.2.4 Stage IV: Equilibrium

With any single-spin-flip dynamics that satisfies detailed balance, at quench temperatures  $T > 0$ , equilibrium is reached. This subtle point distinguishes finite-temperature coarsening from zero-temperature coarsening. Yet for all quench temperatures  $T \lesssim T_C/2$ , the erosion of each arm of a gyroid phase seems to be driven by independent activated spin flips that must occur in succession (Fig. 3.17). Therefore, the average time to reach equilibrium appears to grow *exponentially* in the system size—a feature that is not seen in curvature-

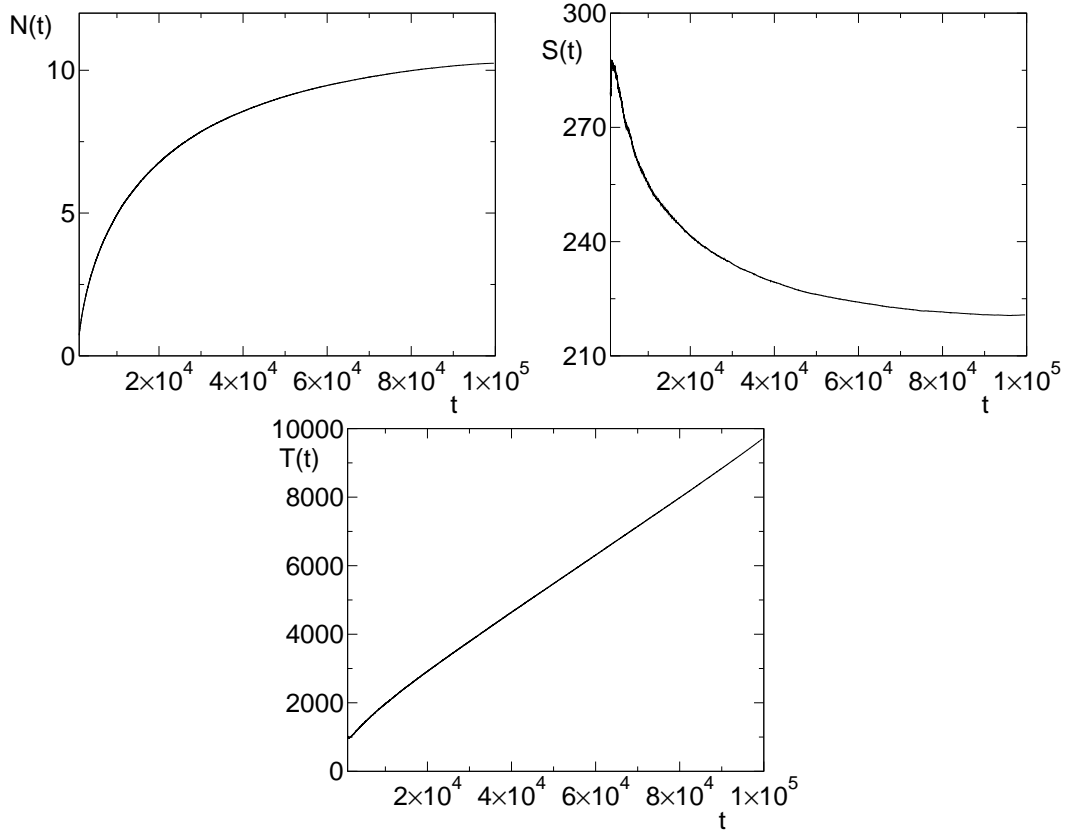


Figure 3.18:  $N(t)$ ,  $S(t)$ , and  $T(t)$  for a quench of a  $32^3$  system to  $T = T_C/8$ . The data are obtained by averaging over  $10^4$  realizations.

driven phase-ordering kinetics. This exponentially long time to equilibrium is insensitive to boundary conditions. For the range of quench temperatures that we studied ( $T \leq T_C/2$ ), the extraordinarily long time scales prevented us from obtaining quality data on time to reach equilibrium.

### 3.3 Time-Dependent Ginzburg-Landau Coarsening in Three Dimensions

We also simulated the time-dependent Ginzburg-Landau equation (1.3) in three dimensions. We employed a simple explicit scheme with centered differencing in space. The absence of a noise term in (1.3) means we are effectively working at zero temperature. For



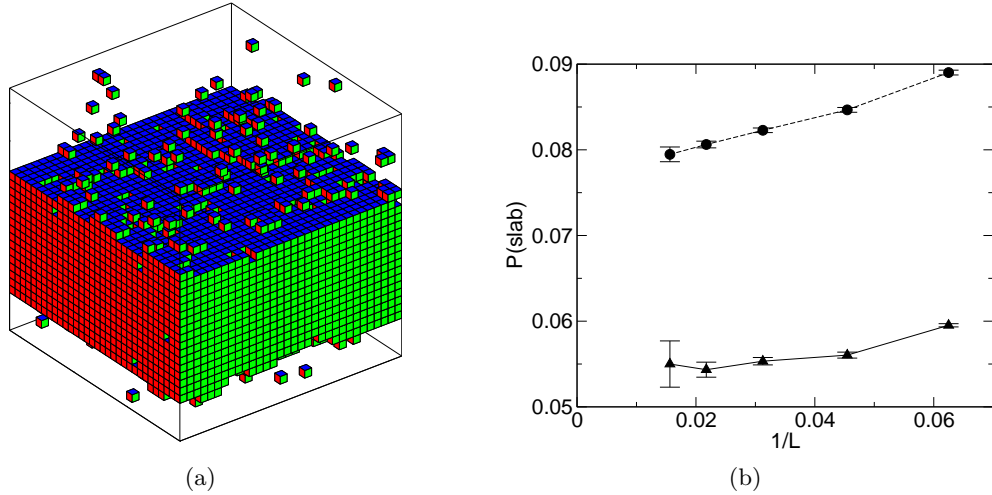


Figure 3.19: (left) Example of two roughly  $16 \times 32^2$  slabs on a  $32^3$  lattice following a quench of a KIM to  $T = T_C/8$ . (right) Probability of getting trapped in a slab state for the Ising-Glauber ( $\circ$ ) and TDGL ( $\triangle$ ) systems. The KIM data is based on  $10^6$  realizations for  $L = 16, 22$ , and  $32$ ,  $5 \times 10^5$  realizations for  $L = 46$ , and  $10^5$  realizations for  $L = 64$ . The TDGL data is based on 1576000 realizations for  $L = 16$ , 424000 realizations for  $L = 22$ , 287000 realizations for  $L = 32$ , 67000 realizations for  $L = 46$ , and 7040 realizations for  $L = 64$ .

our initial state, we draw the order parameter value at each lattice site from a uniform distribution between  $-1$  and  $+1$ , and the order parameter values at neighboring lattice sites are uncorrelated. Unlike simulations of the stochastic Ising model, the TDGL evolution is predetermined for all time once the initial condition is fixed. To get reliable statistics on the typical long-time state of a TDGL quench, we therefore average over many random initial conditions.

At early times in the  $3d$  TDGL evolution, we sometimes observe periodic saddle-type structures with approximately zero curvature on their domain walls resembling the geometries described in [43] (Fig. 3.20). However, it has been mathematically proven [54] that such triply-periodic minimal surfaces are unstable for non-volume-preserving perturbations. Therefore, these types of structures, whenever they form, disappear quickly in the TDGL simulations. Remarkably, we again observe slab states at late times. These states appear slightly less frequently in  $3d$  TDGL evolution than they do in  $3d$  kinetic Ising systems at

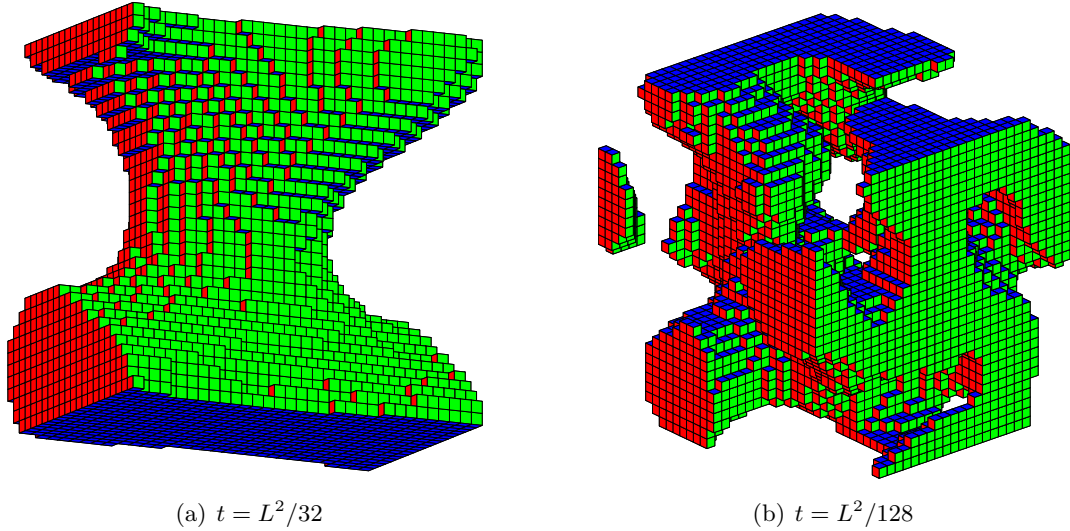


Figure 3.20: Examples of coarsening in two independent realizations of the evolution of the  $3d$  TDGL equation. In both cases, the system size is  $L = 32$ .

finite temperature (Figure 3.19(b)).

### 3.4 Discussion

The lattice structure has a crucial effect on the long-time state of any spin system following a deep quench [55]. We anticipate that a KIM on another type of even-coordinated lattice in  $3d$  will show similarly bizarre behavior [34, 35]. An Ising model on an odd-coordinated lattice will also freeze into a metastable state, but in the case of odd-coordinated lattices, this freezing is a spurious lattice-induced effect. For example, note that a honeycomb-shaped cluster of up spins in a sea of down spins on the hexagonal lattice is trivially stable (Fig. 3.21). This is because each “+” spin has more “+” neighbors than “-” neighbors, leading to purely local freezing of many small clusters. Another example of trivial freezing is the KIM with zero-temperature Kawasaki spin-exchange dynamics [4], where local defects again arise that quickly halt the overall relaxation process.

One tantalizing challenge is to realize spin systems with Glauber dynamics in an experimental setting. Recent experiments on one-dimensional spin chains have revealed rich

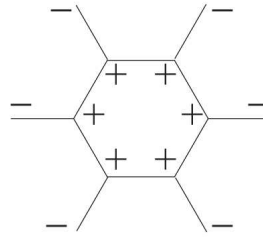


Figure 3.21: A honeycomb-shaped cluster on a hexagonal lattice that is trivially frozen at  $T = 0$ .

behavior [56]. It would likewise be intriguing to establish firm connections between the pinnings seen in the  $3d$  Ising model and structures in real condensed matter systems.

## Chapter 4

# Zero-Temperature Freezing in the Two-Dimensional Potts Model

We have thus far considered nonconserved coarsening of a scalar order parameter, both on  $2d$  and  $3d$  lattices. Two-dimensional nonconserved coarsening appears to be exactly described by a mapping with critical continuum percolation theory, and three-dimensional coarsening of Ising domains on a cubic lattice shows bizarre anomalies that are overlooked by the coarse-grained TDGL formalism. The discreteness effects in the coarsening of Ising domains in  $3d$  are not easily packaged into a clean mathematical description, so our treatment was heavily numerical.

If we now have more than two equivalent species all competing for the equilibrium state, how does the coarsening change? The outcome again depends on the initial and final temperatures, the spatial dimension  $d$ , and the dynamics. As in Chapters 2 and 3, we focus here on coarsening at zero temperature. Just as in the case of two degenerate states, we can study either microscopic stochastic dynamics or a more general TDGL-style description of multi-state coarsening. The formulation of TDGL partial differential equations with three or more competing states is new and is discussed in detail in the chapter. This continuous approach is special because it is based mainly on symmetry considerations and not on specific microscopic dynamics on a particular lattice.

We'd like to study a generalization of the Ising model with additional spin states. A

simple model system with multiple competing states is the Potts model [57] with Hamiltonian

$$\mathcal{H} = - \sum_{\langle ij \rangle} \delta(\sigma_i, \sigma_j), \quad (4.1)$$

where  $\sigma_i$  and  $\sigma_j$  are neighboring spins on a lattice, the sum  $\langle ij \rangle$  is over all nearest-neighbor pairs of spins, and  $\delta$  is the Kronecker delta function [57]. One sees that the energy of the system is lowered by maximizing the number of bonds between like spins. There are many choices for the underlying lattice, but we use the square lattice here for simplicity.

In many ways, the kinetic Potts model connects more directly with physical systems than does the kinetic Ising model. Magnetic grains in metallurgical aggregates can typically take numerous spatial orientations and are successfully modeled by the kinetic Potts model with many states [58]. Time-dependent behavior of soap froths, in which gas typically diffuses through soap films to equalize pressure differences, is also modeled well by coarsening in the many-state Potts model [59]. Connections have additionally been formed between Potts model dynamics and the physics of some cellular tissues [60].

Surprisingly, the kinetic Potts model quenched to subcritical temperature was studied already in the 1980's, much earlier than the zero-temperature Ising model [61]. Even in two dimensions, these studies revealed that the Potts model becomes trapped at low temperatures in a disordered state, even with homogeneous interactions. However, some subtleties were also found regarding the pinning of domain walls. For example, on the triangular lattice, the system coarsens at all final quench temperatures. Also, with NNN interactions between agents on the square lattice, the system coarsens at all final quench temperatures. This suggests that the pinning that was observed on the square lattice with just NN interactions is not typical in more generic models of multi-state coarsening. We will explore the nature of pinning of domain walls in multi-state coarsening in-depth in this chapter.

Just as in Chapters 2 and 3, we endow the model with single-spin-flip Glauber dynamics [21], and we again use the  $n$ -fold way in selecting spins to flip [25]. Given the state of the system at step  $n$ , we identify all possible microscopic updates that may take the system to

step  $n + 1$ . Performing Glauber dynamics on the Potts model is more tedious than on the Ising model, because a single spin may undergo many possible transitions. (For example, in a Potts model with  $q = 5$  states, a single spin with each of its four nearest neighbor spins on the square lattice in different states can flip in four different ways. Since each transition would be energy-preserving, the *total* flip rate for the spin is  $4 \times 1/2 = 2$ .) We keep lists of the different spin types according to their local environment, and we randomly pick a spin with probability proportional to its flipping rate. After flipping the spin, the spin lists are updated, and the next spin-flip event is performed.

## 4.1 Nonsymmetric Initial Condition

We have many initial conditions from which to choose. The case with equal densities of all phases corresponds to supercritical temperature with zero external magnetic field. With a magnetic field applied, some of the phases will initially occupy a larger fraction of the lattice. We consider first a 3-state Potts model with a single phase in the majority. Simulations show that the system always reaches the ground state of the majority phase as the system size  $L \rightarrow \infty$ .

Next, we prepare the system with two species occupying exactly equal numbers of lattice sites, with the third species slightly in the minority. While convergence to thermodynamic behavior is slow, it appears that this initial condition results in Ising-like behavior. To test this systematically, we measure the probability of the Potts model coarsening into a (1,0) (equivalently (0,1)) or a (1,1) stripe topology (see Chapter 2). We evolve initial states with spin densities  $1/3 + \epsilon$ ,  $1/3 + \epsilon$ , and  $1/3 - 2\epsilon$  past the coarsening regime, and we simulate different system sizes  $L$ . At time  $t = L^2$ , we stop the evolution, label all clusters in the system [47], and simultaneously identify percolating clusters [62]. As shown in Fig. 4.1, the probabilities  $\Pi_3$  appear to be approaching our predictions for the kinetic Ising model. As a visual example, Figure 4.2 shows an  $L = 768$  Potts model with red initially in the minority ( $\epsilon = 1/96$ ) coarsening into a diagonal stripe state.

More generally, we may consider a  $q$ -state Potts model with initial densities  $m_1, m_2, \dots, m_q$ .

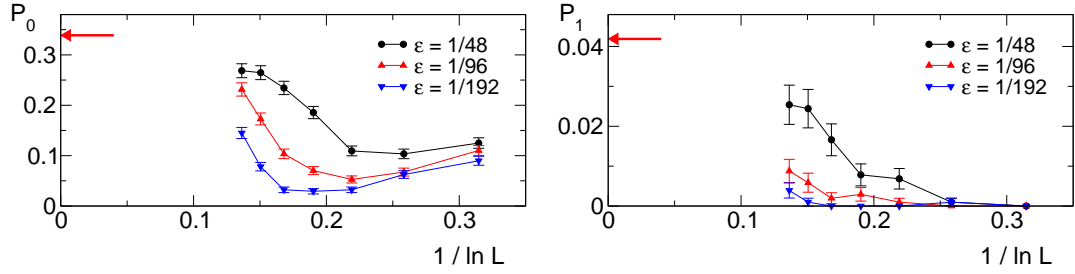


Figure 4.1: Probability for a 3-state Potts model with two species initially in the majority to coarsen into a horizontal/vertical (left) or diagonal (right) stripe topology.

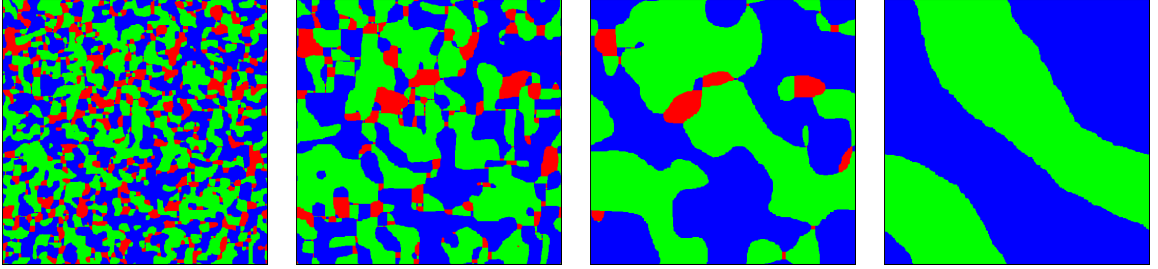


Figure 4.2: An  $L = 768$  Potts model coarsening into a blue-green stripe state with red initially slightly in the minority ( $\epsilon = 1/96$ ).

We can always relabel the densities of the  $q$  species such that  $m_1 \leq m_2 \leq \dots \leq m_q$ . For the 3-state Potts model with nonsymmetric initial condition, our data indicates that:

- $m_1 > m_2 \geq m_3$ : The system reaches the ground state of species 1.
- $m_1 = m_2 > m_3$ : The system reaches the ground state of species 1 or species 2 with combined probability given by Eq. (2.5). All remaining realizations end in stripe states of species 1 and species 2. 1-(2.5).
- $m_1 = m_2 = m_3$ : The long-time behavior is unique.

Based on our findings for the 3-state Potts model, we conjecture that the long-time state of a  $q$ -state Potts model with initial spin densities  $m_1 = \dots = m_Q > \dots \geq m_q$  is identical to the long-time state of a  $Q$ -state Potts model with all  $Q$  phases initially equal. This simple conjecture may be invalidated by local pinning effects as the number of Potts

states  $q$  becomes large [63]. We tried testing this numerically, but our computing resources were insufficient to collect reliable statistics. Nonetheless, it appears that the symmetric point with all  $q$  phases initially equal is the only point that represents unique behavior in the  $q$ -state Potts model, so we focus on the symmetric initial condition throughout the remainder of the chapter.

## 4.2 The Long-Time State

Starting from a symmetric initial condition, the Potts model evolves to a highly non-trivial long-time state. In our simulations, we always observe one of three basic outcomes:

- The system reaches one of the ground states.
- The system reaches a frozen state consisting of at least two spin clusters.
- The system reaches a non-static blinker state that is similar to the states observed in the quench of a  $3d$  Ising model (see Chapter 3).

We ask the basic question: What is the typical long-time state following the quench to  $T = 0$  in the thermodynamic limit. Intriguingly, we have not been able to answer this question definitively for any  $q \geq 3$ .

Early studies revealed that the Potts model tends to become pinned permanently at  $T = 0$  [61]. Many studies have additionally focused on behavior during the coarsening regime and on long-time thermally-activated process following a quench to positive subcritical temperature [63, 64, 65]. These works implicitly lead one to believe that the  $T = 0$  final state in the thermodynamic limit *always* consists of a patchwork of spin domains frozen in place. Indeed, we have simulated the Potts model with  $q = 3, 4, 5$ , and 6, and we typically observe beautiful domain mosaics at late times (Fig. 4.3). It is easy to see how such complex cluster patterns arise. In Fig. 4.4, three spin domains meet at right angles. On the square lattice with only nearest-neighbor spin-spin interactions, none of the four spins at the center of this T-junction can flip at zero temperature, since such a move would raise the energy.



This is a crucial distinction between the  $2d$  Ising model and the  $2d$  Potts model, since in the former system domain boundaries must always form closed loops. As the number of states  $q$  increases, it therefore seems natural that pinning of clusters should occur more readily, as shown in Fig. 4.3.

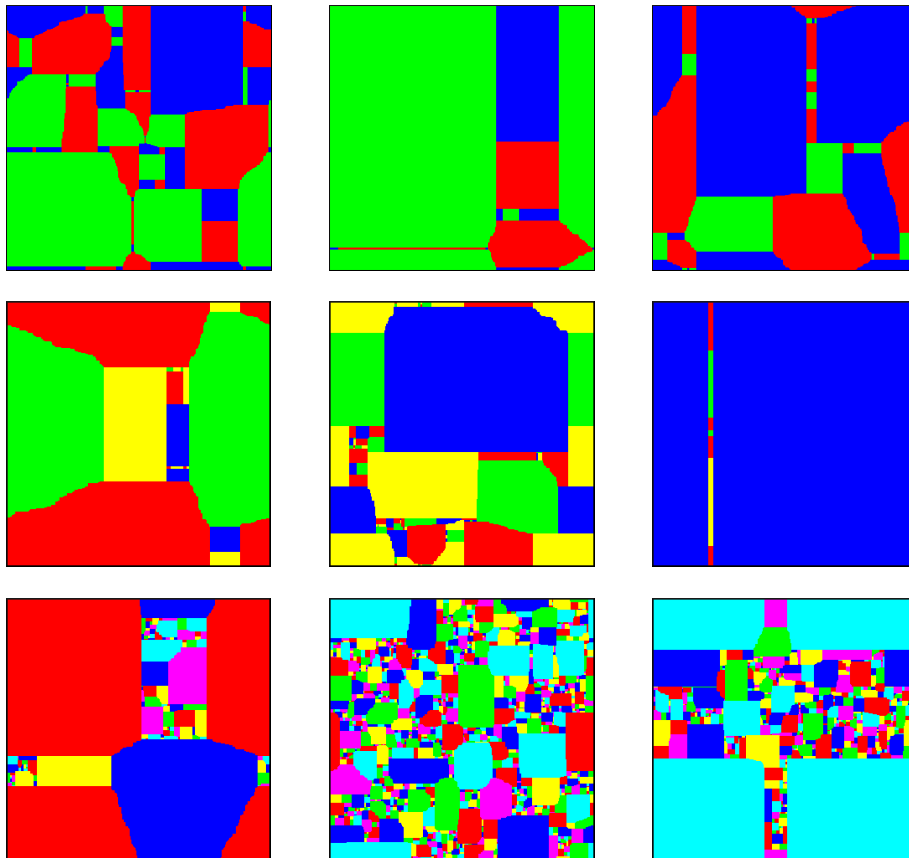


Figure 4.3: Typical outcomes for the  $q = 3$  (top),  $q = 4$  (middle), and  $q = 6$  (bottom) Potts models after being quenched to zero temperature. The number of clusters in the final state typically increases as  $q$  increases.

To begin to understand coarsening in the Potts model, consider Figure 4.5, which shows the energy (averaged over many realizations) versus time shortly after the quench. The energy decays roughly as a power law and consistently with the understanding  $E \sim L^{-1/2}$  from the theory of nonconserved coarsening [5, 35]. We see that by time  $t = L^2$ , the decay in energy has essentially stopped, but there are subtle relaxation mechanisms that will be

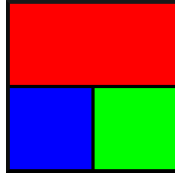


Figure 4.4: A T-junction, where three spin domains meet at right angles, is stable at zero temperature.

described in detail later.

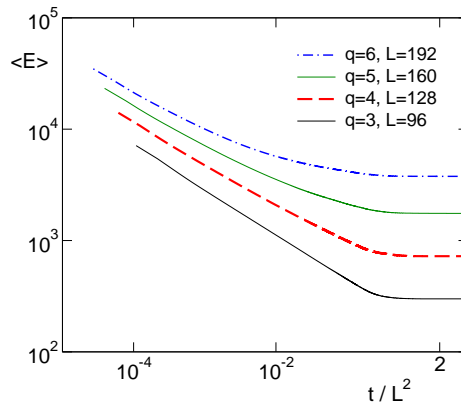


Figure 4.5: Energy versus time for  $q = 3, 4, 5,$  and  $6$ . The energy was averaged over 4096 realizations for  $q = 3$  and over 512 realizations for each  $q = 4, 5,$  and  $6$ .

We now perform a more systematic analysis. We quench 3, 4, 5, and 6-state Potts models from infinite to zero temperature. For concreteness, for each system size  $L$ , we record data at time  $t = 2L^2$ . The time  $t = 2L^2$  is sufficiently beyond the initial coarsening regime that the system consists of a cluster geometry whose global structure is essentially frozen in place.

First consider the average energy per spin,  $E/L^2$ , versus  $L$  (Fig. 4.6(a)). For  $q = 3$ , fitting this data to a power law gives this normalized energy decaying as roughly  $L^{-0.8}$ . Fitting to a power law becomes more dubious as the number of spin states is increased, yet one sees that the normalized energy decays more slowly with  $L$  as  $q$  increases. This makes sense, since for larger  $q$ , clusters at the coarsening time are smaller and the total amount of interface between domains increases.

We also measured the average number of clusters,  $N_C$ , at late times. We expect this quantity to grow as a power law in  $L$ , and for  $q = 6$ , it appears that  $N_C \sim L^2$ . This means that for  $q = 6$ , the freezing of spin clusters is purely local. Since the typical length scale of clusters is constant, the normalized energy per spin approaches a nonzero constant in the thermodynamic limit. Interestingly, in Ref. [63], the normalized energy per spin is extrapolated to the thermodynamic limit for different  $q$ , and the authors conclude that the critical number of states for which purely local pinning occurs, i.e.  $N_C \sim L^2$ , is  $q = 5$ . We did not exhaust this point in our studies because we discovered new late-time coarsening mechanisms that make it difficult to reliably predict thermodynamic behavior, even for  $q = 3$ .

Figure 4.6(c) is perhaps most interesting. In this plot, we show the probability of the system reaching one of the possible ground states. Shockingly, this probability approaches zero and then apparently begins rising sharply as  $L$  is increased for all  $q \geq 3$ . What could be causing this conspicuous non-monotonic behavior? As we shall see, the Potts model features a slew of hidden complexities that become apparent after careful examination.

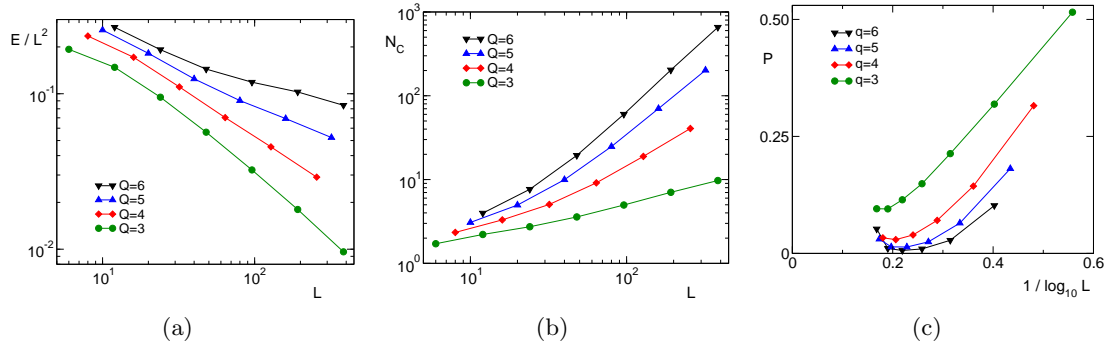


Figure 4.6: (a) The average energy per spin and (b) the average number of clusters for a  $q$ -state Potts model after a quench, with  $q = 3, 4, 5$ , and  $6$ . (c) The probability for a Potts model to reach the ground state by time  $t = 2L^2$  after a quench to zero temperature. Data are based on  $2^{14}$  realizations for the largest two values of  $L$  for  $q = 3$  and for the largest value of  $L$  for each  $q = 4, 5$ , and  $6$ . All other data points are based on  $2^{17}$  realizations. Error bars are smaller than the size of the symbols.

### 4.2.1 Blinker States

Similarly to the  $3d$  Ising model, typical long-time states in the Potts model feature either permanent or extremely long-lived blinker states. Blinker states feature many spins at any given time that are capable of changing state with no energy cost to the system. Blinkers are much easier to conceptualize in the Potts model than in the  $3d$  Ising model. In Fig. 4.7(a), we see four blinker interfaces that lie diagonally with respect to the  $x$ - and  $y$ -axes. Each of these blinker states is pinned at its two ends by T-junctions, and the spins on the blinker interfaces can flip repeatedly at zero temperature.

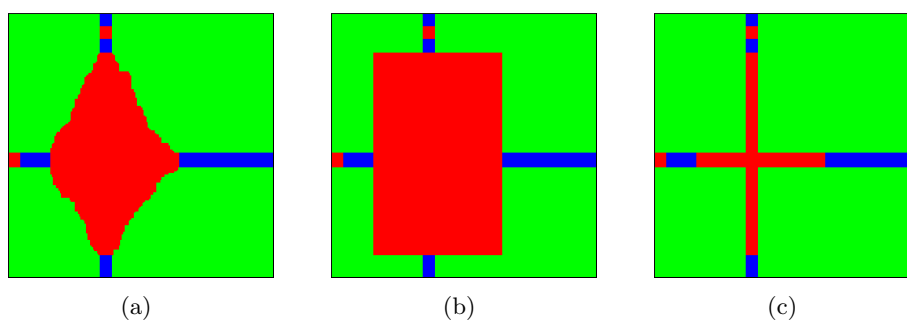


Figure 4.7: Example of a blinker state in the  $2d$  Potts model.

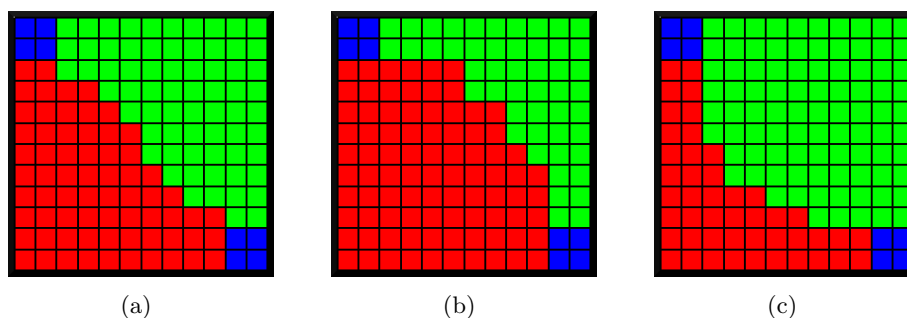


Figure 4.8: Blinkers tend to remain in their intermediate states (a), rather than in an inflated or a deflated state ((b) or (c)).

An important feature of blinker interfaces is that they tend to remain in their intermediate states. Consider Fig. 4.8(b). There are four red blinker spins on the interface and only three green blinker spins. Since each blinker spin—red or green—flips with equal

probability, the red interface will tend to recede. Now consider Fig. 4.8(c). There are four green blinker spins on the interface and only three red blinker spins, so the green interface will tend to recede. In Section 3.1.3, we determined the typical time for a  $2d$  blinker region of linear size  $\ell$  to reach its fully inflated or fully deflated state as  $\exp(\ell)$ . Therefore, the blinker interface tends to spend most of its time in an intermediate state, Fig. 4.8(a).

#### 4.2.2 Pseudo-Blinker States

Also similarly to the  $3d$  Ising model, the Potts model features pseudo-blinker states at late times that are responsible for extraordinarily slow relaxation to a fixed-energy state. A single blinker interface as shown in Fig. 4.7 or 4.8 cannot affect the energy of a system, but two oppositely-oriented blinker states (Fig. 4.9) can lead to isolated energy-lowering events at extraordinarily late times.

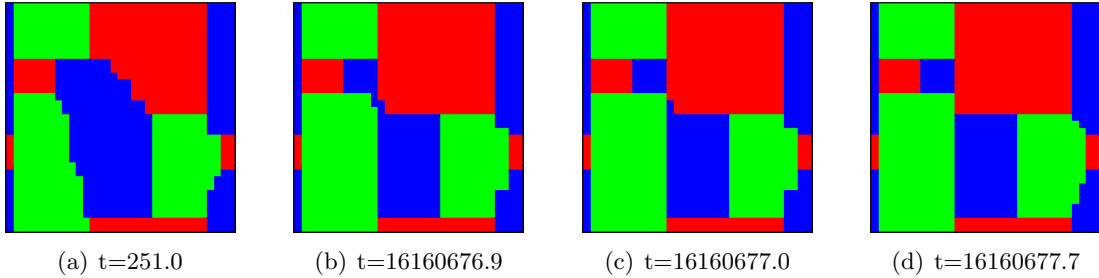


Figure 4.9: Example of a pseudo-blinker state and a late-time coalescence event in the  $2d$  Potts model. The energy drops from  $E = 188$  to  $E = 185$ .

We may ask: What is the probability  $S(t)$  that a given realization of the quench has not reached a fixed-energy state by time  $t$ . We use an algorithm similar to that for measuring the corresponding survival probability in the  $3d$  Ising model:

- i We separately track the number of flippable spins that would lower the energy on being flipped,  $N_-$ , and the number of flippable spins that would not change the energy on being flipped,  $N_0$ . When the former quantity goes to zero while the latter remains nonzero, the system could be in a fixed-energy state. We save the lattice  $\mathcal{C}_0$  and the time  $\mathcal{T}_0$ .

ii Starting at time  $\mathcal{T}_0$ , we apply an infinitesimal bias field in the -1 direction:

$$\mathcal{H} = \epsilon \sum_{\langle i \rangle} \delta(\sigma_i, 1) - \sum_{\langle ij \rangle} \delta(\sigma_i, \sigma_j) \quad (4.2)$$

This forces all blinker spins in state 1 to flip to either state 2 or 3. If there are energy-lowering moves while the bias field is applied, then the system is not in its lowest-energy configuration. The bias field is removed, the system is returned to configuration  $\mathcal{C}_0$  and time  $\mathcal{T}_0$ , and evolution continues until the next energy-lowering move occurs, at which time this test is repeated.

iii If there are no energy-lowering moves with a bias field applied in the -1 direction, then bias fields are also applied in the -2 and then the -3 directions. If no energy-lowering moves occur after application of all three bias fields, then the system's lowest-energy configuration is  $\mathcal{C}_0$ , and its survival time is  $\mathcal{T}_0$

The survival probability  $S(t)$  for both the 3- and 6-state Potts models is shown in Fig. 4.10. Similarly to the 3d Ising case, it was difficult to obtain clean data collapse. Dividing time by  $L^{2.3}$  gives reasonable collapse in the early-time coarsening regime for  $q = 3$ , but this procedure becomes more dubious for  $q = 6$ . The salient point is that pseudo-blinker states and their associated late-time relaxation play an increasingly important role as both the system size and the number of spin states increase. Even for  $q = 3$  and  $L = 48$ , there are realizations that have not yet reached a fixed-energy configuration at times a factor  $10^5$  longer than the coarsening time!

### 4.2.3 Cluster “Avalanches” at Late Times

There is a crucial difference between pseudo-blinker states in the 3d Ising model and the Potts model. In the Ising case, pseudo-blinkers are benign, each leading to a tiny drop in energy of the system at some late time. However, in the Potts model, pseudo-blinker coalescence events (Fig. 4.9) can effect drastic reorderings of the domain structure and macroscopic drops in energy, even at extraordinarily late times. To see how this happens,

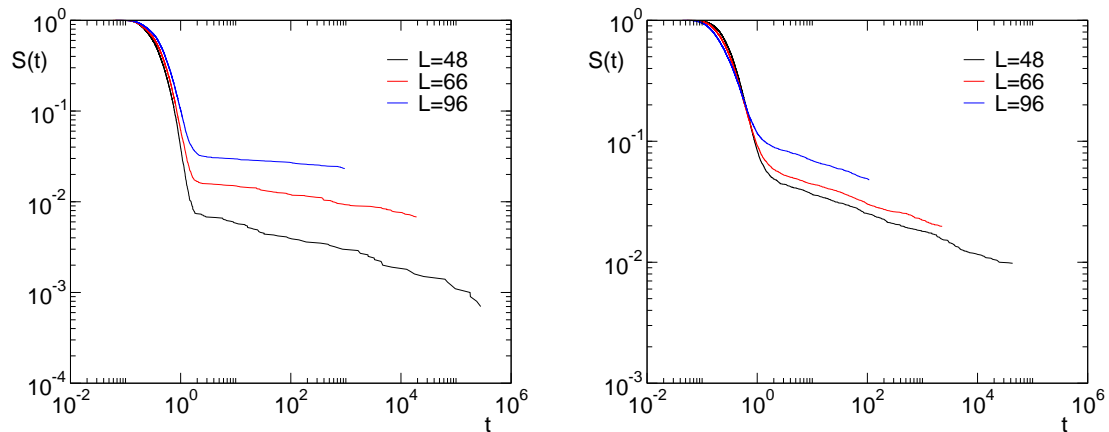


Figure 4.10: Survival probability for the 3-state (left) and 6-state (right) Potts models. The data for each curve is averaged over  $10^4$  realizations.

consider Fig. 4.11, which shows a 6-state Potts model with  $L = 192$  that reaches a pseudo-blinker state with a complex cluster geometry by roughly time  $t = L^2$ . At  $t = 630000$ , the system is still trapped in the pseudo-blinker state. By  $t = 633000$ , notice that the two yellow pseudo-blinker interfaces have merged. Remarkably, an “avalanche” ensues, whereby a newly-merged yellow cluster fills out its convex hull, eventually merging with other yellow clusters, which then fill out their convex hulls, etc. By  $t = 640000$ , this realization has reached its final fixed-energy state, and the global domain structure has changed drastically. During the avalanche, the system undergoes a nearly 50% drop in energy—from 5051 to 2849!

Notice in Figure 4.11 that the convex envelopes of the two large yellow clusters in (c) and (d) do not overlap. How is it possible for these two clusters to eventually merge? Consider Figure 4.12, which shows this merging process in detail. The key feature is that a cluster can expand beyond its original convex envelope. In Figure 4.12(h), the large yellow cluster at left expands its convex hull one unit to the right. How did this happen? In Figure 4.12(g), there is a red spin bounded by another red spin below, a yellow spin at left, and blue spins above and to the right. This red spin flips to yellow (Fig. 4.12(h)), which is an energy-preserving move. In Figures 4.12(l) and (n)), the yellow cluster expands its

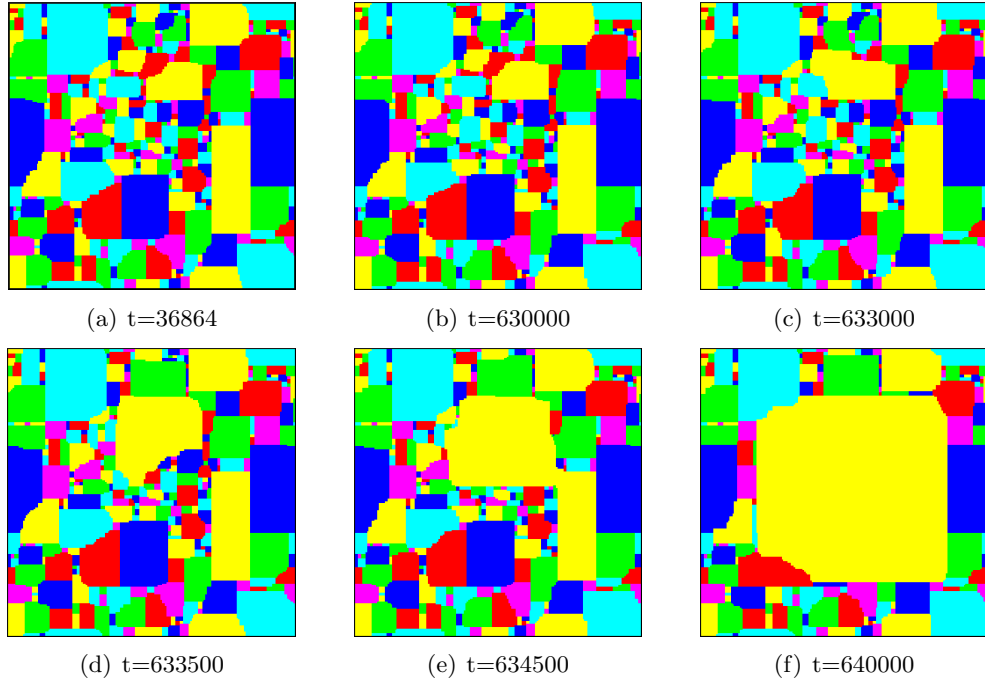


Figure 4.11: Example of a late-time cluster avalanche in the 6-state Potts model on an  $L = 192$  lattice.

convex hull again, and in Figure 4.12(n), the irreversible merging of the two large yellow clusters is complete. Figure 4.13 offers another view at how a cluster can expand beyond its original convex envelope. Notice that “2” flipping to “1” (first and second panels) is an energy-preserving move, and is thus permissible.

Equally surprising is that the long-time fixed-energy state of a Potts model is generally unpredictable, even at late times. If we take the second panel in Fig. 4.11 (shortly after the two pseudo-blinker interfaces have touched) and use this as our initial configuration, we find that the system takes markedly different paths as it descends in energy (Fig. 4.14). We ran  $10^4$  realizations of the avalanche, and the energies of the final states range from a minimum  $E = 490$  to a maximum  $E = 4383$ , with average  $\bar{E} = 2827$  and standard deviation  $\sigma_E = 1159$ . This makes it nearly impossible to infer the lowest-energy configuration following a given quench from the early-time data. The trick of applying bias fields that was used for studying the  $3d$  Ising model would influence the avalanches artificially, so this technique is



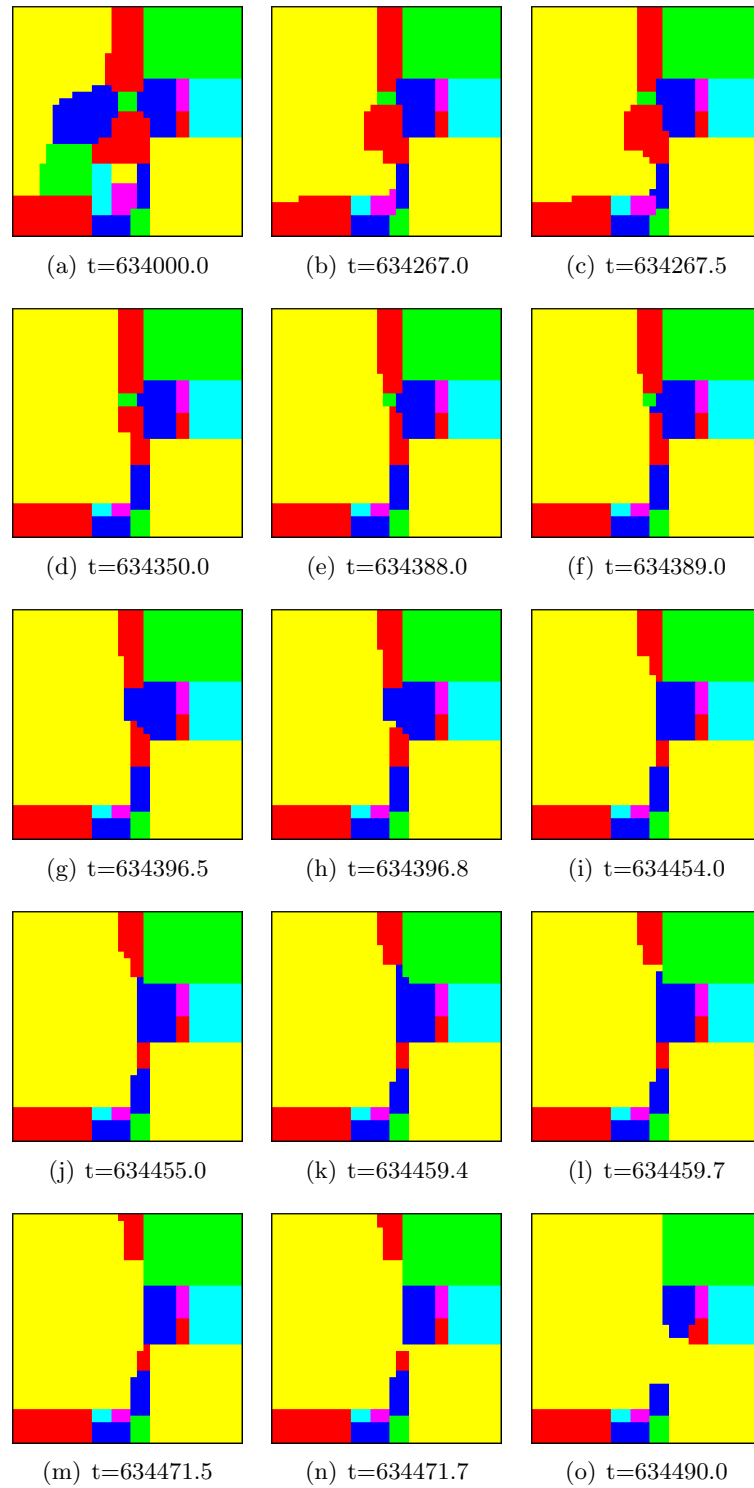


Figure 4.12: An example of a cluster expanding beyond its original convex envelope during an avalanche.

3 2 2 2 2 2	3 2 2 2 2 2	3 2 2 2 2 2	3 2 2 2 2 2
3 2 2 2 2 2	3 2 2 2 2 2	3 2 2 2 2 2	3 2 2 2 2 2
3 2 3 3 3 3	3 1 3 3 3 3	3 1 1 3 3 3	3 1 1 1 3 3
1 1 1 1 1 1	1 1 1 1 1 1	1 1 1 1 1 1	1 1 1 1 1 1

Figure 4.13: Schematic showing the upward expansion of the convex hull of the “1” domain.

not well suited for studying the Potts model.

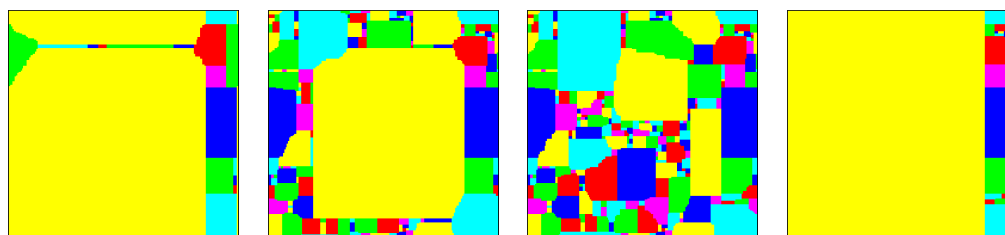


Figure 4.14: Examples of four different outcomes of the avalanche shown in Fig. 4.11.

### 4.3 Reaching the Ground State

We’d like to generically understand the final outcome of the  $2d$  Potts model quenched to  $T = 0$ . The pseudo-blinker states and the unpredictable avalanches that they generate manifest in a time that grows exponentially in the system size. While these phenomena are interesting, the nonmonotonicity in the probability to reach the ground state shortly after the initial coarsening (Fig. 4.6) is peculiar.

Shown in Fig. 4.15 are two independent realizations of the 6-state  $L = 192$  Potts model coarsening into a ground state shortly after the quench. In both realizations, it appears that the system is quickly becoming pinned into a complex domain mosaic ((a) and (e)). Focus now on the top four images. In (b), notice that two green clusters, oriented northeast-southwest, have grown in size and have just barely merged into a single cluster. This larger green cluster grows rapidly, quickly engulfing all other clusters and driving the system to the green ground state. A similar phenomenon occurs in the realization shown in the bottom row. In (f), two purple clusters oriented northwest-southeast barely merge, and this

merging again triggers a rapid expansion that ends in the purple ground state. Among the realizations that reach the ground state, the characteristic time for reaching the ground state is of the order of the coarsening time, and the distribution of times to reach the ground state is approximately exponential. We conjecture that the Potts model has a greater propensity for reaching a ground state as both the number of states  $q$  and the system size  $L$  increase, and this claim is supported by Fig. 4.6.

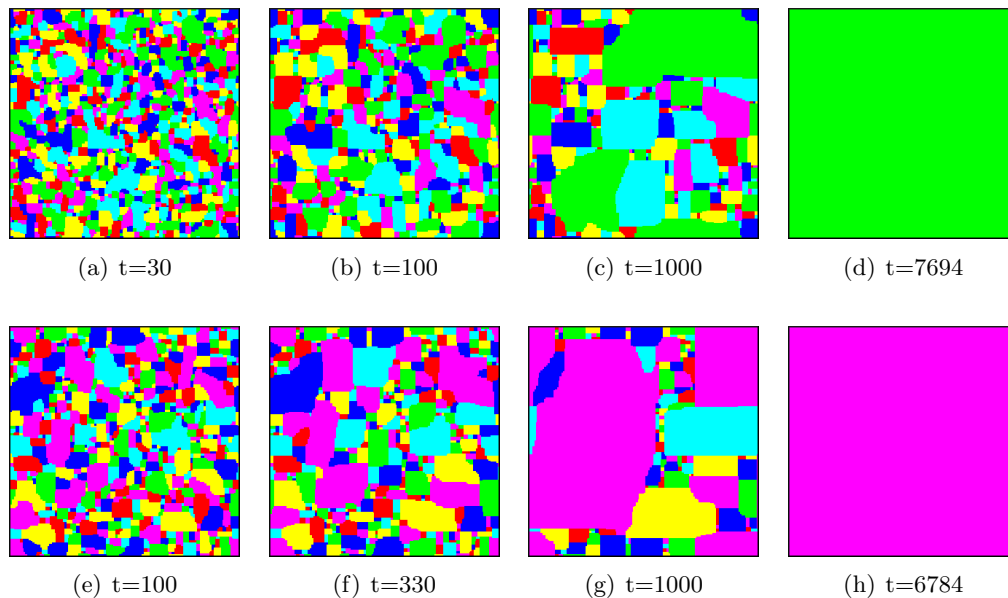


Figure 4.15: Examples of two realizations (top and bottom) of the 6-states  $L = 192$  Potts model coarsening rapidly into a ground state.

The avalanching seen in the Potts model bears strong resemblance to the phenomenon of bootstrap percolation [66, 8]. In this  $2d$  binary cellular automaton, a square lattice is initially prepared with a fraction  $p$  of its sites randomly chosen to be alive. The update rule is that a site is born if two or more of its neighbors are active, and all active sites remain alive forever. What fraction of sites need to be alive initially for all  $L^2$  cells in the system to become activated? It has been proven [67] that, as  $L \rightarrow \infty$  and  $p \rightarrow 0$ , an avalanche always ensues that results in all  $L^2$  sites being activated, although it is difficult to appreciate this asymptotic behavior from computer simulations on finite-size grids. The avalanches in the Potts model are subtly different from bootstrap percolation. In a Potts model avalanche,

recall that clusters can expand their convex envelopes, a feature absent from bootstrap percolation. Also in the Potts model, interfaces between two clusters can typically diffuse in both directions. However, the presence of additional spin states creates opportunities for irreversible spin flips during an avalanche so that growing clusters tend to fill out their convex hulls. The qualitative connections with bootstrap percolation nonetheless raise the question: Does the kinetic Potts model *always* reach one of its  $q$  ground states in the thermodynamic limit?

#### 4.4 A Time-Dependent Ginzburg-Landau Description of Multi-State Coarsening

Many possibilities arise in choosing microscopic rules for the Potts model. For example, we may simulate the 3-state Potts model on a triangular lattice rather than the square lattice. The rationale is that the coordination number of 6 for the triangular lattice is a more natural setting for 3-state coarsening. Do complex cluster geometries still arise for the 3-state Potts model on the triangular lattice? We did not simulate this system, but Grest and coworkers [61] examined this question several decades ago and did not find any pinning on the triangular lattice. For the Potts model quenched to  $T = 0$  on the triangular lattice, they found standard coarsening with the Allen-Cahn growth exponent  $1/2$ . Clearly, one must be careful in extracting generic conclusions about multi-state coarsening from simulations on any particular lattice.

In the spirit of generality, can one formulate a simple TDGL-style description of multi-state coarsening? We found several studies [68, 69, 70] that address this question, although they do not present clear results on the long-time state.

We invented a simple description of 3-state coarsening that is based on a two-component vector order parameter  $\vec{\phi}(\mathbf{x}, t) = \{\phi_1(\mathbf{x}, t), \phi_2(\mathbf{x}, t)\}$ . We propose the free-energy functional

$$F_3[\vec{\phi}] = \int \frac{1}{2} \left[ (\nabla\phi_1)^2 + (\nabla\phi_2)^2 + (\vec{\phi} - \vec{A})^2 (\vec{\phi} - \vec{B})^2 (\vec{\phi} - \vec{C})^2 \right] d^d x, \quad (4.3)$$

Notice that our potential now has three wells symmetrically distributed at the three vertices of a triangle, representing equal strength of competition between the three phases. Taking the functional derivative of (4.3), we get

$$\frac{\partial\phi_1}{\partial t} = \nabla^2\phi_1 - \frac{1}{2} \frac{\delta}{\delta\phi_1} \left[ (\vec{\phi} - \vec{A})^2 (\vec{\phi} - \vec{B})^2 (\vec{\phi} - \vec{C})^2 \right] \quad (4.4)$$

$$\frac{\partial\phi_2}{\partial t} = \nabla^2\phi_2 - \frac{1}{2} \frac{\delta}{\delta\phi_2} \left[ (\vec{\phi} - \vec{A})^2 (\vec{\phi} - \vec{B})^2 (\vec{\phi} - \vec{C})^2 \right] \quad (4.5)$$

When evolved from a disordered initial state, these two coupled equations will either take the TDGL system to one of the three ground states with equal probability, or will result in a frozen domain structure similar to the configurations seen in the square-lattice Potts model. There are several natural initial conditions to consider: an order parameter with (i) unit radius and random angular distribution, (ii) unit radius and always in one of the three symmetric wells (discrete angular distribution), (iii) unit radius and always outside of the wells, (iv) radius close to zero with random angular distribution, etc.

While most realizations of 3-state TDGL reached the ground state, we also observed non-trivial geometries (Fig. 4.16). In roughly 11% of realizations, three hexagons form. In roughly 8% of realizations we obtain configurations with two squares and two octagons. In a tiny fraction ( $< 1\%$ ) of realizations, six hexagons materialize and are pinned in place. We also observe Ising-like horizontal and vertical stripe states with roughly 10% probability. The remaining approximately 70% of realizations reach one of the three ground states (Fig. 4.17). For a given system size  $L$ , the long-time outcome appears to be most sensitive to the length of the initial order parameter vector. (Notice that for an order parameter with smaller radius, the TDGL system tends to more easily reach a ground state.)

The average number of clusters in the long-time state in TDGL coarsening (for an initial order parameter with unit radius and random angular distribution) grows only from 1.22(1) for  $L = 16$  to 1.57(3) for  $L = 128$ . (The growth in the number of clusters with  $L$  is similar or slower for different initial conditions.) Clearly, the Potts model on the square lattice becomes pinned much more readily than the isotropic TDGL system, as we may

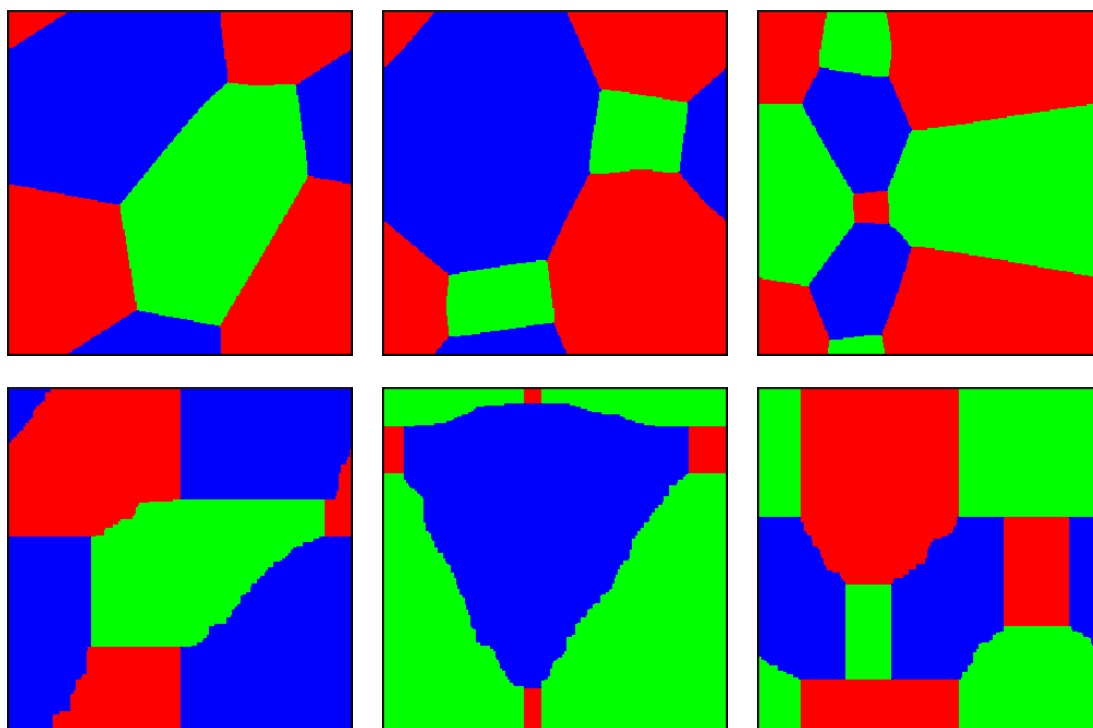


Figure 4.16: Examples of long-time states in 3-state TDGL (top) and in the 3-state Potts model (bottom).

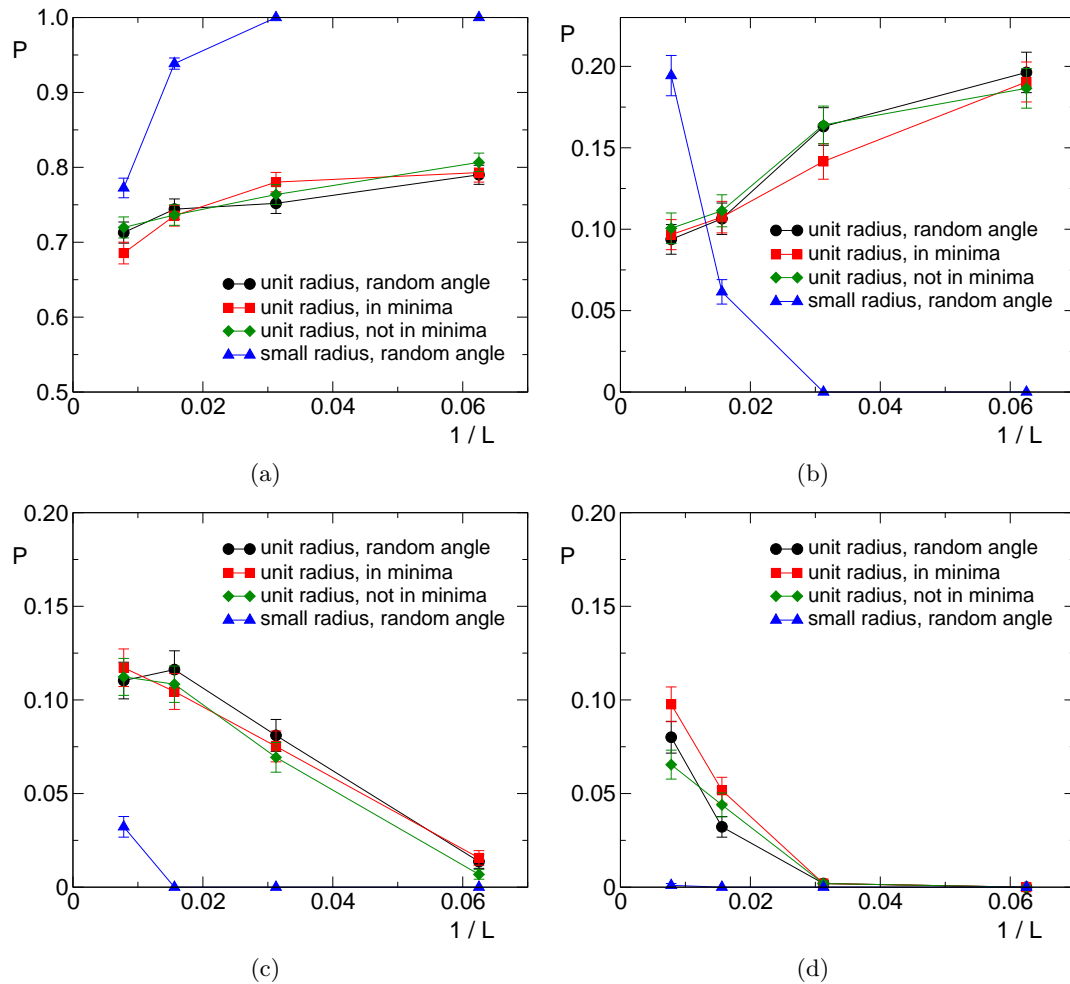


Figure 4.17: Probability for a 3-state TDGL evolution to end in one of the ground states (a), an Ising-like vertical or horizontal stripe state (b), a state with three hexagons (c), or a state with four clusters (d), as a function of  $1/L$  and for different initial conditions. The triangles represent simulations with an initial order parameter radius equal to  $1/10$ .

have suspected. Consider Fig. 4.18, which shows a multi-colored stripe state. In the Potts model, the state (a) is stable at zero temperature, but unstable in 3-state TDGL. To see why, notice that in the Potts model on the square lattice, domain boundaries always meet at right angles. In 3-state TDGL, three domain boundaries must meet at  $120^\circ$  angles. In (b), as the angles in the T-junctions begin to equalize, a curvature is generated on the domain interfaces, which tends to further shrink the multi-colored stripe (c). The final state in 3-state TDGL is just the green ground state (d). This subtle difference may explain why the

Potts model on the square lattice becomes pinned much more readily than 3-state TDGL.

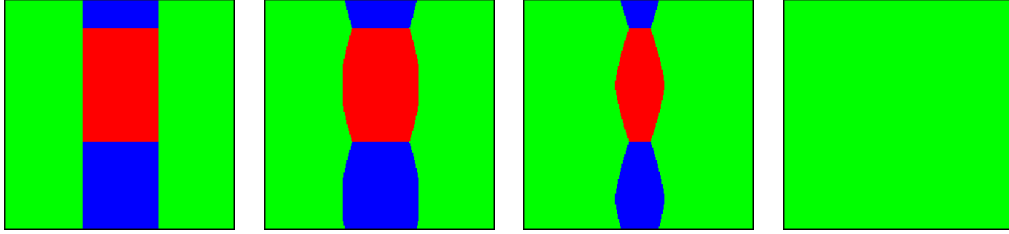


Figure 4.18: A multi-colored stripe state (a) is stable in the Potts model but is unstable in multi-state TDGL (b-d).

## 4.5 Discussion

Intriguingly, a significant fraction of realizations of the quench of the Potts model show features that are reminiscent of the  $3d$  Ising model. We typically observe freezing into a geometrically complex long-time state. Blinker interfaces that lie diagonally with respect to the  $x$ - and  $y$ -axes abound, leading to many non-static final states at  $T = 0$ . We also identify pseudo-blinker states that lead to drops in energy at extraordinarily long times in the dynamics, further enhancing the parallel with the  $3d$  Ising model.

Yet the Potts model is unique in many ways. Domain interfaces in two dimensions may terminate at T-junctions, and we attribute the intricate late-time cluster geometries to this efficient pinning of domain interfaces. Surprisingly, pseudo-blinker states introduce unforeseen complexities into the late-time relaxation. Pseudo-blinker merging events can lead to avalanches that have macroscopic effects on observables such as energy and number of clusters. Crucially, a pseudo-blinker merging event can trigger an avalanche that results in a ground state being reached. One of our main results is that the Potts model for all  $q \geq 3$  reaches a ground state with nonzero probability in the thermodynamic limit.

Our other central result is that the multi-state TDGL equations (4.4) and (4.5) also lead to nontrivial cluster patterns at late times. It would be interesting to do more careful numerical work on multi-state TDGL in an attempt to infer thermodynamic behavior. To



generically describe coarsening with  $q$  competing states, we can introduce a vector order parameter in  $(q-1)$ -dimensional space, and we can orient the potential wells symmetrically at the  $q$  corners of a simplex. This results in  $q-1$  coupled TDGL equations for the evolution of the order parameter. We have not yet simulated this TDGL system for  $q > 3$ . It would be interesting to see if this simple model reproduces the complex cluster patterns seen in the quench of a high-state Potts model on the square lattice.

## Chapter 5

# Two-Dimensional Interface Growth with Nearest-Neighbor and Longer-Range Ising Interactions

In Chapters 2, 3, and 4, I focused on the ultimate fate of a kinetic Ising or Potts ferromagnet quenched from a random, high-temperature initial state to zero temperature. Perhaps our most important result is that an intriguing and so far unexplained connection with critical continuum percolation seems to exactly predict the probabilities of freezing into various stripe topologies in two dimensions. Our conjecture of universality of two-dimensional coarsening—that many stochastic single-spin-flip systems and curvature-driven coarsening models have the same final-state statistics—is profound. While there are always open questions, our recent work tremendously enhances understanding of two-dimensional non-conserved coarsening with scalar order parameter.

In the second half of this dissertation, I examine a complementary problem. If we *begin* in a state with smooth, macroscopic domain boundaries in  $2d$ , how do the domain interfaces evolve in time? One nice feature of this problem is that equations are simple and deterministic. Recall that with random initial condition and discrete spin variables, we carefully tested the trapping probabilities for various Hamiltonians to demonstrate universality. If we test the same models against one another with smooth initial condition, do domain interfaces all evolve the same? The answer is no, as we shall see.

## 5.1 Standard Ising Interactions

Consider a two-dimensional Ising model on a square lattice with nearest-neighbor ferromagnetic interactions.

$$\mathcal{H} = - \sum_{\langle ij \rangle} \sigma_i \sigma_j \quad (5.1)$$

Rather than starting with an infinite temperature state, we begin at zero temperature with a wedge, or corner, geometry (Fig. 5.1(left)). Note that at zero temperature, all spins in the bulk and all spins on the flat domain boundary are not flippable, because flipping such a spin would raise then energy of the system. The only flippable spins at zero temperature are corner spins. Initially, there is only one eligible corner spin to flip. After the first spin flip, there are two minus spins that are eligible to flip, while the spin that flipped to plus on the previous move can flip back to minus.

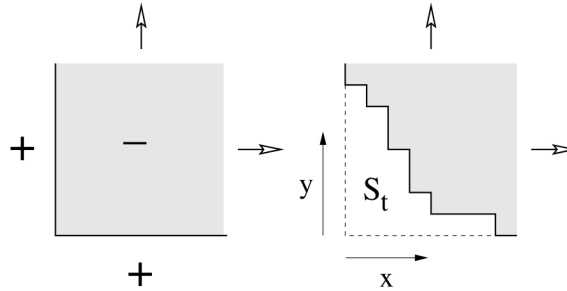


Figure 5.1: The initial interface is the boundary of a quadrant (left). At a later time  $t$ , the interface encloses an area  $S_t$  (right).

Figure 5.1(right) shows the interface between the plus and minus phases after several spin flips. Let  $N_+$  and  $N_-$  denote the numbers of inner and outer corners on the interface, respectively. In Figure 5.1(right), for example, we have 6 inner corners and 5 outer corners. As the interface grows in time, the quantities  $N_+$  and  $N_-$  naturally increase. However, the difference

$$N_+ - N_- = 1, \quad (5.2)$$

is a topological invariant in two dimensions, holding true at all times in the interface growth

process. If inner and outer corner spins flip with equal rates, corresponding to zero external bias magnetic field, then, on average, the interface will grow in time  $t$ , and the average total number of flipped spins  $S_t = t$ . After many spin flips, the interface growth becomes more deterministic. Indeed, since the interface grows diffusively, if we plot the variable  $\xi = x/\sqrt{4t}$  versus  $\eta = y/\sqrt{4t}$ , we find that the interface approaches a well-defined limiting shape as  $t \rightarrow \infty$ .

To understand this limiting shape analytically, we map the unbiased corner growth process in two-dimensions onto an effective one-dimensional particle-hopping process [71, 72, 73] (Fig. 5.2). Note that our interface has simply been rotated  $45^\circ$  counterclockwise for easy visualization. In this picture, each northwest-southeast segment of the interface maps onto a particle, while each southwest-northeast segment of the interface maps onto a vacancy. The unbiased corner growth process may now be specified completely in terms of the one-dimensional particle dynamics: A spin flipping from minus to plus corresponds to a particle hopping one unit to the right, while a spin flipping from plus to minus corresponds to a particle hopping one unit to the left. This one-dimensional particle mapping is just the simple exclusion process (SEP) introduced by Spitzer [74] and is a paradigmatic simple model in statistical mechanics [75].

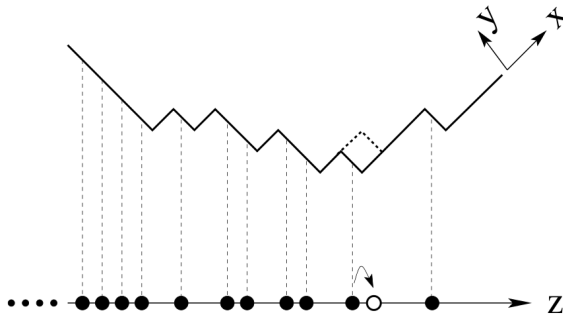


Figure 5.2: Mapping of the corner growth model onto the simple exclusion process.

While both models describe the same process, the one-dimensional simple exclusion process is more amenable to mathematical analysis. We need a suitable hydrodynamic description of the SEP. Let us define the average density  $\rho(z, t)$  of particles in a small region

on the line. The region of interest must be large relative to the lattice spacing but small compared with the overall extent of the nontrivial density profile. In our hydrodynamic description of the SEP, we use the diffusion equation

$$\frac{\partial \rho}{\partial t} = \frac{\partial}{\partial z} \left( D(\rho) \frac{\partial \rho}{\partial z} \right) \quad (5.3)$$

with, in general, a density-dependent diffusion coefficient  $D(\rho)$ , and the initial condition

$$\rho(z, t = 0) = \begin{cases} 1, & \text{if } z < 0 \\ 0, & \text{if } z > 0 \end{cases} \quad (5.4)$$

corresponding to the wedge geometry in the original  $2d$  corner problem. For the symmetric SEP, the diffusion coefficient is independent of density:  $D(\rho) = 1$ . The Green's function for our diffusion equation for the density profile is a Gaussian, and convolving with the step initial condition gives a complementary error function

$$\rho(z, t) = \frac{1}{2} \operatorname{erfc} \left( \frac{z}{\sqrt{4t}} \right) \quad (5.5)$$

for the average particle density profile.

To determine the limiting shape of the Ising corner, we use the implicit integral equation

$$y = \int_{x-y}^{\infty} \rho(z, t) dz \quad (5.6)$$

to obtain

$$\eta = \frac{1}{\sqrt{\pi}} \int_{\xi-\eta}^{\infty} du \int_u^{\infty} dv e^{-v^2}, \quad (5.7)$$

where we have used the properly scaled variables  $\xi = x/\sqrt{4t}$  and  $\eta = y/\sqrt{4t}$ .

## 5.2 Long-Range Ising Interactions

We would now like to extend our treatment to an Ising corner geometry with next-nearest-neighbor spin-spin interactions. Is the limiting shape (5.7) universal? Generally, we consider

a class of Ising Hamiltonians

$$\mathcal{H}_k = - \sum_{n=1}^k \sum_{|\mathbf{i}-\mathbf{j}|=n} J_n \sigma_i \sigma_j \quad (5.8)$$

with the Manhattan metric  $|\mathbf{i}-\mathbf{j}| = |i_1 - j_1| + |i_2 - j_2|$ .  $k$  is the interaction range. With  $k = 1$ , Eq. (5.8) reduces to Eq. (5.1), while with  $k = 2$ , Eq. (5.8) describes an Ising model with NN and (diagonal and weaker) NNN spin-spin interactions. Spins separated by a Manhattan distance greater than  $k$  simply do not interact. All couplings  $J_n$  are ferromagnetic and rapidly decreasing with  $n$ , so at zero temperature, only the interaction range  $k$  matters.

Formally, our treatment for next-nearest-neighbor (NNN) interactions is similar to our analysis for nearest-neighbor (NN) interactions. We employ the particle mapping in the  $45^\circ$ -rotated frame, and our task is to again solve the hydrodynamic equation of motion (5.3), but now with a nontrivial density-dependent diffusion coefficient. To fix ideas, we would like to develop an intuitive feel for how NNN Ising interactions influence the particle dynamics. For both NN and NNN interactions, we start with the half-filled line

$$\dots \bullet \bullet \bullet \bullet \bullet \circ \circ \circ \circ \circ \dots$$

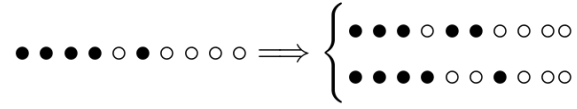
and the first move is the hopping of the rightmost particle one unit to the right

$$\dots \bullet \bullet \bullet \bullet \bullet \circ \circ \circ \circ \circ \dots \implies \dots \bullet \bullet \bullet \bullet \bullet \circ \bullet \circ \circ \circ \circ \dots$$

On the second move, the particle hopping possibilities are different depending on the range of the Ising interactions. With only NN interactions ( $k = 1$ ), the allowed moves are

$$\bullet \bullet \bullet \bullet \circ \bullet \circ \circ \circ \circ \implies \left\{ \begin{array}{l} \bullet \bullet \bullet \bullet \bullet \circ \circ \circ \circ \\ \bullet \bullet \bullet \circ \bullet \bullet \circ \circ \circ \\ \bullet \bullet \bullet \bullet \circ \circ \bullet \circ \circ \end{array} \right.$$

but with NN and NNN interactions ( $k = 2$ ), the allowed moves are



Note that with NNN Ising interactions, the rightmost particle cannot hop backward to its starting position, since doing so would raise the energy. The general rule for NNN Ising interactions is that a particle hop is allowed only if the move would not increase the number of nearest-neighbor pairs of particles.

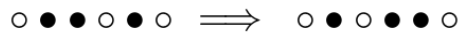
By a lengthy formal derivation [76], the density-dependent diffusion coefficient in the particle mapping of the NNN corner problem is

$$D(\rho) = \begin{cases} (1 - \rho)^{-2}, & \text{if } 0 < \rho < \frac{1}{2} \\ \rho^{-2}, & \text{if } \frac{1}{2} < \rho < 1. \end{cases} \quad (5.9)$$

Notice that the diffusivity of the lattice gas is maximal ( $D = 4$ ) where the density  $\rho = 1/2$ . To get an intuitive feel for this result, first note that where  $\rho \approx 0$  ( $\rho \approx 1$ ), a single particle (vacancy) can diffuse freely, giving  $D = 1$ . For the case  $\rho = 1/2$ , consider a particle configuration with a single defect:



The single eligible move in this configuration is



Thus a single particle hopping event by one lattice site in the case  $\rho = 1/2$  generates a disturbance that propagates by two lattice sites. Since  $D \sim (\Delta x)^2$ , we infer  $D = 4$  when  $\rho = 1/2$ , which is consistent with (5.9).

Substituting (5.9) into (5.3), and using the scaling form

$$\rho(z, t) = f(\zeta), \quad \zeta = \frac{z}{\sqrt{4t}}, \quad (5.10)$$

we arrive at the ordinary differential equation

$$\frac{d}{d\zeta} \left[ (1-f)^{-2} \frac{df}{d\zeta} \right] + 2\zeta \frac{df}{d\zeta} = 0 \quad (5.11)$$

for the scaled interface profile. By symmetry, we need to only consider the half-line  $\zeta \geq 0$  with boundary conditions

$$f(\zeta) = \begin{cases} \frac{1}{2} & \text{if } \zeta = 0 \\ 0 & \text{as } \zeta \rightarrow \infty. \end{cases} \quad (5.12)$$

We solved this boundary value problem numerically and obtained the corner interface shape shown in Figure 5.3.

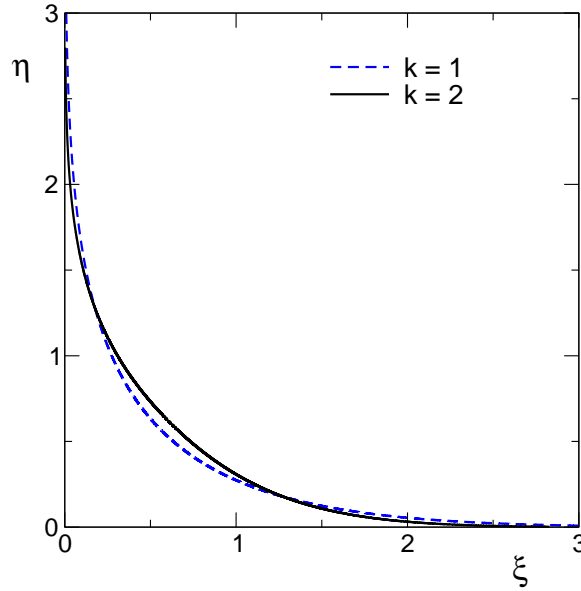


Figure 5.3: Plot of the two-dimensional corner interface with nearest-neighbor ( $k = 1$ ) and nearest- and next-nearest-neighbor ( $k = 2$ ) Ising interactions. (Note that the curves have been scaled to each have unit area.)

Clearly, universality does not hold for two-dimensional interface motion with varying interaction range between Ising spins. As a simple quantitative comparison, consider the growth of the  $2d$  Ising interface along the diagonal. That is, we are considering the inter-



section of the interface with the ray  $x = y$ . A simple integration of Eq. (5.7) gives

$$\frac{x_{\text{diag}}}{\sqrt{t}} = \frac{y_{\text{diag}}}{\sqrt{t}} = \frac{1}{\sqrt{\pi}} \approx 0.5642 \quad (5.13)$$

at the middle point for NN interactions. For NNN interactions, we can solve numerically for the middle point:

$$\frac{x_{\text{diag}}}{\sqrt{t}} = \frac{y_{\text{diag}}}{\sqrt{t}} \approx 0.8655. \quad (5.14)$$

The locations of the middle points on the interface in the two models differ substantially. As a second demonstration of lack of universality, we may consider the total number of spins that have flipped from initially down to up by time  $t$ . This is just the total area  $A$  under the nontrivial part of the interface. In the model with NN interactions, the relation is simple:  $A = t$ . This equality is exact in the infinite-time limit and follows directly from Eq. (5.2); since inner corners always exceed outer corners by exactly one, the interface grows at rate 1. With NNN interactions, the relation is equally simple:  $A = 2t$ . This formula is easy to explain. At late times, the interface near the diagonal point, for an increasingly large fraction of time, consists of an alternating sequence of particles and holes. On the section of the interface below the diagonal, the number of flippable inner corner spins exceeds the number of flippable outer corner spins by exactly one, and similarly for the section of the interface above the diagonal. So for the entire interface at late times, when the lattice spacing is small compared with the total size of the growing interface, the number of eligible inner corner spins exceeds the number of eligible outer corner spins by 2, from which  $A = 2t$  intuitively follows.

### 5.3 Biased Motion

Let's now consider the growing corner interface in the presence of an external bias magnetic field. The external magnetic field is infinitesimal and favors the majority phase, so that spins at inner corners can flip, but spins at outer corners cannot flip. A theoretical analysis of biased corner growth is simpler than that of the unbiased growth of the previous section.

Consider first the growth of an Ising corner with a bias magnetic field and NN spin-spin interactions. This biased growth process maps perfectly onto the asymmetric simple exclusion process (ASEP) [4]. In ASEP, particles may only hop to the right; moves to the left are forbidden. Just as in the symmetric case, exclusion demands that no two particles may occupy the same lattice site at the same time.

Mathematically, in the hydrodynamic mapping, our task is to solve the continuity equation

$$\frac{\partial \rho}{\partial t} + \frac{\partial J}{\partial z} = 0 \quad (5.15)$$

where  $J(z)$  is the particle current. For ASEP, it has been proven mathematically that

$$J = \rho(1 - \rho) \quad (5.16)$$

Miraculously, the dependence of the particle current  $J$  on particle density  $\rho$  is essentially mean-field. A particle hopping event occurs if site  $i$  is occupied and site  $i + 1$  is vacant, and since ASEP has stationary product measure, the pair correlation function factorizes to give (5.16). After substitution, the resulting hydrodynamic equation

$$\frac{\partial \rho}{\partial t} + \frac{\partial[\rho(1 - \rho)]}{\partial z} = 0 \quad (5.17)$$

is just the inviscid Burgers equation and can be solved using standard techniques. In terms of the variable  $z = x - y$ , the particle density is

$$\rho = \frac{1}{2} \left( 1 - \frac{z}{t} \right). \quad (5.18)$$

Using the geometrical mapping between the density  $\rho$  in the ASEP mapping and the Cartesian coordinates  $x$  and  $y$ ,

$$\rho = \frac{\frac{\partial y}{\partial x}}{\frac{\partial y}{\partial x} - 1}, \quad (5.19)$$

we arrive at the scaled limiting shape

$$\sqrt{\frac{x}{t}} + \sqrt{\frac{y}{t}} = 1 \quad (5.20)$$

for the two-dimensional corner growth process with biased dynamics and NN interactions [77].

What if we consider instead biased corner growth with NN and NNN spin-spin interactions? How does the limiting interface shape change?

With NNN spin-spin interactions, it is again possible to map the interface profile onto a particle exclusion process with longer-range interactions [78]. To find the limiting shape for NNN spin-spin interactions, it is instructive to consider more carefully our analytical results outlined above for NN interactions. By differentiating (5.20), the corner growth process with only NN interactions may be alternatively understood in terms of the interface growth velocity

$$y_t = \frac{y_x}{y_x - 1}, \quad (5.21)$$

where we use the standard PDE notation  $y_t$  and  $y_x$  to denote  $\partial y / \partial t$  and  $\partial y / \partial x$ , respectively. A striking feature is that the corner interface growth velocity at any point is independent of the curvature  $y_{xx}$  of the interface. Since all higher-order spatial derivatives beyond  $y_x$  are negligible, for simplicity, let's focus on a small segment of the interface that is essentially flat. Our region of interest is small compared with the overall scale of the growing curved interface but large compared with the lattice spacing. In the ASEP mapping, we compute the particle current at this point on the interface via the pair correlation function

$$J = \langle p_i (1 - p_{i+1}) \rangle, \quad (5.22)$$

where  $p_i$  is the probability, at any given instant, that site  $i$  in the ASEP particle mapping is occupied. As mentioned above, this quantity factorizes in ASEP, so our equation for  $J$  simplifies to

$$J = \langle p_i \rangle (1 - \langle p_{i+1} \rangle) = \langle p \rangle (1 - \langle p \rangle). \quad (5.23)$$

Now let's connect (5.23) with the interface geometry. On our small segment of the interface, each particle corresponds to a tiny geometrical line segment  $\delta y$ , and each vacancy corresponds to a tiny geometrical line segment  $\delta x$ . The total number of particles in the ASEP mapping on this section of interface is just  $\Delta y = \sum \delta y$ , and the total number of vacancies is just  $\Delta x = \sum \delta x$ . Next, note that the rate that each tiny horizontal line segment  $\delta x$  increases its position vertically in time is equal to the particle current  $J$  divided by the density of vacancies ( $1 - \langle p \rangle$ ), and this quantity is just the growth velocity  $y_t$ . Combining these pieces, we obtain our already-known result

$$y_t = \frac{J}{1 - \langle p \rangle} = \langle p \rangle = \left| \frac{\Delta y}{\Delta y + \Delta x} \right| = \frac{y_x}{y_x - 1} \quad (5.24)$$

with minimal effort. (Note that the minus sign arises because the slope  $y_x$  is negative.)

This simple geometrical route to obtaining the growth equation (5.21) is powerful for helping us understand  $2d$  corner growth with NNN spin-spin interactions. Let's consider the portion of the interface below the diagonal. Note that holes are always separated by at least one particle. Below the diagonal, we can perform a second particle mapping: Each particle-hole pair is mapped onto an "A" particle, and all remaining holes are each mapped onto "B" particles. Notice that with the particle hopping rules outlined above for NNN Ising interactions with a bias field, in the second particle mapping, the "A" and "B" particles and their dynamics form another asymmetric simple exclusion process in which an "A" particle hops one unit to the right if its neighbor to the right is a "B" particle.

Now just as with NN interactions, let's connect the "AB" particle dynamics with the geometry of the growing corner interface. Each "A" particle corresponds to a vertical segment of the interface next to a horizontal segment of the interface ( $\delta y$ ). Each remaining "B" particle corresponds to one of the horizontal line segments that was not already counted as part of an "A" particle ( $\delta x - \delta y$ ). If we denote by  $N_A$  and  $N_B$  the numbers of A and B particles on a small segment of the interface, then, repeating the analysis above for NN

biased interactions, we obtain for the NNN dynamics:

$$x_t = \frac{J}{\langle N_A \rangle} = \langle N_B \rangle = \frac{N_B}{N_A + N_B} = \left| \frac{\Delta x - \Delta y}{\Delta y + (\Delta x - \Delta y)} \right| = 1 - \frac{1}{|x_y|}. \quad (5.25)$$

By symmetry, it follows that for points above the diagonal ( $y > x$ ),  $y_t = 1 - 1/|y_x|$ . Using the simple relation  $y_t = -y_x x_t$  for points below the diagonal ( $y < x$ ), we obtain the interface growth velocity with biased NNN interactions:

$$y_t = \begin{cases} 1 + \frac{1}{y_x}, & \text{if } y \geq x \\ -y_x(1 + y_x), & \text{if } y < x. \end{cases} \quad (5.26)$$

Using elementary techniques, we solve the growth equations for interface points above and below the diagonal, and we obtain for the limiting shape of the corner with NN and NNN interactions:

$$\frac{y}{t} = \begin{cases} 1 - 2\sqrt{\frac{x}{t}}, & \text{if } y \geq x \\ \frac{1}{4} \left[ 1 - 2\frac{x}{t} + \left(\frac{x}{t}\right)^2 \right], & \text{if } y < x. \end{cases} \quad (5.27)$$

The limiting shapes for NN and NNN Ising spin-spin interactions with biased dynamics are shown in Figure 5.4. Notice that a point on the interface with slope  $y_x = -1$  would have zero growth velocity. This seems paradoxical since the interface is forever growing in time: How can the middle point be stationary? To solve this dilemma, the growing NNN corner interface with biased dynamics forms a kink at the point  $x = y$ , so that the slope  $y_x$  there is undefined. This intriguing kink at the center of the growing interface with biased dynamics remains as the interaction range increases beyond next-nearest-neighbor spins [79].

Let's now derive the interface shape for NNN Ising interactions more formally. The average current  $J(\rho)$  has been computed [76]

$$J(\rho) = \begin{cases} \frac{\rho(1-2\rho)}{1-\rho}, & \text{if } 0 < \rho < \frac{1}{2} \\ \frac{(1-\rho)(2\rho-1)}{\rho}, & \text{if } \frac{1}{2} < \rho < 1. \end{cases} \quad (5.28)$$

This form for the current appears in a number of models [78]. The maximal current  $J_{\max} = J(\rho^*) = J(\rho_*) = 3 - 2\sqrt{2}$  occurs for the densities  $\rho^* = \frac{1}{\sqrt{2}}$  and  $\rho_* = 1 - \frac{1}{\sqrt{2}}$ .

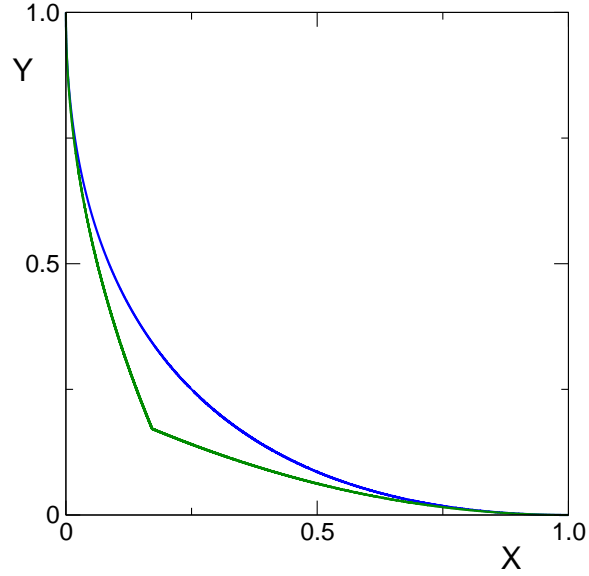


Figure 5.4: The corner interface in the presence of a bias magnetic field and for  $k = 1$  (upper curve) and  $k = 2$  (lower curve).

Again, note that the density admits a scaling form

$$\rho(z, t) = R(Z), \quad Z = \frac{z}{t}. \quad (5.29)$$

Plugging this form into Eq. (5.29), we obtain a rarefaction wave

$$R(Z) = \begin{cases} 1, & \text{if } Z < -1 \\ (2 + Z)^{-1/2}, & \text{if } -1 < Z < 0 \\ 1 - (2 - Z)^{-1/2}, & \text{if } 0 < Z < 1 \\ 0, & \text{if } Z > 1 \end{cases} \quad (5.30)$$

for the initial condition given by (5.4). After an elementary integration (5.6), we recover Eq. (5.27) for the scaled limiting shape.

## 5.4 Discussion

Amusingly, the statistically more complex problem of two-dimensional nonconserved coarsening (Chapter 2) shows universal behavior, while the analytically simpler corner growth process of this chapter depends strongly on microscopic details. This chapter focused on developing simple, intuitive understanding of interfacial growth equations and limiting shapes in two-dimensional corner growth. Analogous growth models in  $3d$  are substantially more resistive to theoretical methods. The next chapter focuses on one such three-dimensional corner growth process.

## Chapter 6

# Three-Dimensional Interface Growth Inside a Corner

### 6.1 The Model

The study of growing interfaces has attracted much interest among statistical physicists. Many growth processes on one-dimensional substrates are thoroughly understood with regards to stochastic height fluctuations and limiting shapes. Surface growth on two-dimensional substrates is considerably more difficult, and few exact results have been proven [80]. The models studied typically involve flat two-dimensional substrates and therefore flat (on average) interfaces, considerably simplifying the analysis.

Here, our goal is to describe the limiting shape of a large crystal growing inside an infinite corner. As our model for crystal growth, consider a single octant of 3-space that is initially empty. Elemental  $1 \times 1 \times 1$  unit cubes are stochastically deposited into available ‘inner’ corners (Fig. 6.1). Initially at  $t = 0$ , there is only one inner corner and thus one place where the first cube will fit. After the first deposition event, there are three available inner corners where the next cube can be adsorbed. The stochastic deposition of cubes into inner corners continues until the interface approaches a deterministic limiting shape.

This growth model may alternately be viewed as the erosion of a three-dimensional crystal that initially occupies an infinite corner. In this picture, each elemental cube can also be interpreted as an ‘up’ spin in a  $3d$  Ising model, while the surrounding empty space



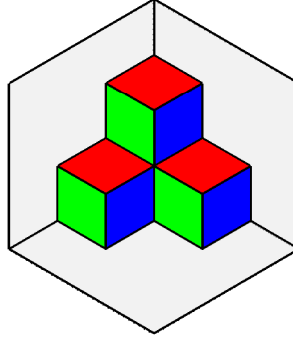


Figure 6.1: 3d crystal of volume 4. The next elemental cube can be deposited equiprobably at any one of the 6 inner corners.

is filled with ‘down’ spins. Then the problem is equivalent to the motion of the domain wall between two ordered phases. This growth model can also be viewed as the tiling of a hexagonal coordinate system with three distinct types of rhombi, and a deposition event corresponds to the cyclic rearrangement of three adjacent elemental rhombi. This system bears similarities with a recently proposed “zigzag model” [81], which is an infinite set of coupled exclusion processes in the plane. Here for simplicity we keep the picture of deposition of elemental cubes into available inner corners.

Much is known on the statistical properties of similar growth models in two dimensions. There are three natural settings to consider: (i) uniform measure, (ii) Ising dynamics, and (iii) growth dynamics. For the uniform measure, the interface has the shape of an irregular staircase and is nonincreasing from left to right. Such interfaces are known as Young diagrams in mathematics. Each interface configuration of total area  $N$  is given weight  $1/p(N)$ , where  $p(N)$  is the number of distinct diagrams with area  $N$ . In two dimensions, the limiting shape is given by  $e^{-\xi} + e^{-\eta} = 1$ , with  $\xi = \pi x/(6\sqrt{N})$  and  $\eta = \pi y/(6\sqrt{N})$  [82]. The uniform measure in three dimensions has also been solved parametrically [83]. The counting of the numbers of Young diagrams in dimensions greater than 3 remains unsolved.

In the Ising dynamics, cubes are equiprobably added to ‘inner’ corners or removed from ‘outer’ corners. In Figure 6.1, for example, there are six inner corners and three outer corners. When desorption of elemental cubes is allowed, the linear scale of the interface

grows diffusively as  $\sqrt{t}$ . In the long-time limit, fluctuations become small, and a limiting shape is reached, although in two dimensions this shape has no simple explicit form (see Chapter 5).

In this chapter, we focus on the growth dynamics. Thus, we consider only the case in which elemental cubes are added to available inner corners. The limiting shape of the corner growth model in  $2d$  was first studied and solved by Rost [77]. In the long-time limit, the interface grows and approaches a deterministic limiting shape in which fluctuations become small. The equation governing the motion of the interface was presented in Chapter 5 [84]:

$$y_t = \frac{y_x}{y_x - 1}. \quad (6.1)$$

It can easily be shown that

$$\sqrt{x} + \sqrt{y} = \sqrt{t} \quad (6.2)$$

is a solution to the above PDE and is the correct limiting shape for the growth dynamics in two dimensions. This result can also be obtained by mapping the two-dimensional growth model onto the totally asymmetric simple exclusion process. Interface height fluctuations in the  $2d$  corner growth model are also well understood [85, 86].

## 6.2 Conjectural Governing Equation for Growth in Three Dimensions

For the corner growth problem in three dimensions, we have not succeeded in deriving a governing PDE from the underlying stochastic dynamics. We expect such an equation to have a form similar to Eq. (6.1), i.e.,

$$z_t = f(z_x, z_y). \quad (6.3)$$

To make progress, we make educated guesses for the form of  $f(z_x, z_y)$ . In particular, note the following:

- The equation (6.3) must reduce to (6.1) on the boundaries of the interface where  $x = 0$  ( $z_x = -\infty$ ) and where  $y = 0$  ( $z_y = -\infty$ ).
- The equation (6.3) must be invariant under the exchange of any pair of coordinates.

These conditions severely constrain the forms of possible equations. As a first guess, it is natural to try  $z_t = [z_x/(z_x - 1)][z_y/(z_y - 1)]$ , which is a simple product form of the exact governing equations on the  $x = 0$  and  $y = 0$  planes. Note that when  $z_x = -\infty$ , we recover the exact governing equation on the plane  $x = 0$  (and similarly for  $y$ ). However, this form is not invariant under the exchange of  $z$  and  $x$  or  $z$  and  $y$ , so it is incorrect. We proceed by assuming the following form for  $z_t$ :

$$z_t = \frac{z_x}{z_x - 1} \frac{z_y}{z_y - 1} A(z_x, z_y) \quad (6.4)$$

and the challenge is to guess a form for  $A(z_x, z_y)$  that makes Eq. (6.4) invariant. We have found two valid forms for  $A(z_x, z_y)$  that satisfy this requirement. Also, by combining these two forms for  $A(z_x, z_y)$  we have found infinitely many valid governing equations of the form (6.4), although these equations are more complex.

To guess the correct form for  $A(z_x, z_y)$ , we use a clue from simulation data. Note that the form (6.3) implies that the local velocity of a point on the interface depends only on the local slopes  $z_x$  and  $z_y$ . Although this is not proven in  $3d$ , physical intuition suggests that higher-order derivatives are asymptotically negligible. Our idea is to simulate a *flat* interface with periodic boundaries. (This growth model is known as the ‘hypercube stacking model’ and was introduced by Forrest and Tang [87] to study interface height fluctuations.) This model evolves by the same stochastic dynamics of depositing elemental cubes into available inner corners. However, the periodic boundaries bring a huge simplification to the analysis. One simply allows the flat plane to evolve, measures the total vertical distance it moved, and divides by the total time elapsed to obtain an average velocity. We simulated the flat plane with slopes  $z_x = z_y = -1$ . For the (average) vertical velocity of this plane,

we measure

$$v_{\text{flat plane}} \approx 0.378.$$

Note that 0.378 is very close to the rational number  $3/8 = 0.375$ . We conjecture that the interface velocity for the hypercube stacking model and  $z_t$  for the corner interface at the point  $x = y = z$  are identical, which requires that Eq. (6.4) reduces to exactly  $3/8$  in the limit  $t \rightarrow \infty$ , viz.

$$z_t|_{z_x, z_y = -1} = \left(\frac{1}{2}\right) \left(\frac{1}{2}\right) A(z_x, z_y)|_{z_x, z_y = -1} = \frac{3}{8}.$$

which obviously implies

$$A(z_x, z_y)|_{z_x, z_y = -1} = \frac{3}{2}.$$

Note that the form  $A(z_x, z_y) = 1 - 1/(z_x + z_y)$  reduces to  $3/2$  with  $z_x = z_y = -1$ , so we conjecture that the correct governing equation in  $3d$  is

$$z_t = \frac{z_x}{z_x - 1} \frac{z_y}{z_y - 1} \left(1 - \frac{1}{z_x + z_y}\right). \quad (6.5)$$

This equation satisfies all theoretical requirements for describing  $3d$  corner growth. We have numerically tested this equation on flat planes with different values of the slopes  $z_x$  and  $z_y$ , and in all cases we have found our prediction (6.5) and the measured velocity to agree within roughly 1%.

### 6.2.1 Simulation Results

We proceed by solving our conjectural governing equation (6.5) for the case of an initially empty corner. As this is a first-order PDE, it is amenable to the method of characteristics. However, our equation is fully non-linear, which complicates the analysis. For illustration of the method, consider the corresponding two-dimensional (exact) governing equation

$$z_t = \frac{z_x}{z_x - 1}.$$

We would like to solve this equation for the case of an initially empty corner using the method of characteristics. Following the standard procedure for a fully non-linear equation, we write the governing equation in the form

$$F(z, t, x, p, q) = p - \frac{q}{q-1} = 0,$$

where we have set  $p = z_t$ ,  $q = z_x$ . The characteristics equations are

$$\begin{aligned} \frac{dt}{ds} &= F_p = 1 \\ \frac{dx}{ds} &= F_q = \frac{1}{(q-1)^2} \\ \frac{dz}{ds} &= pF_p + qF_q = \frac{q^2}{(q-1)^2} \\ \frac{dp}{ds} &= -F_t - pF_z = 0 \\ \frac{dq}{ds} &= -F_x - qF_z = 0 \end{aligned}$$

Thus along the characteristics, we immediately read off  $t = s$ , while the interface velocity  $p$  and slope  $q$  are both constant. This allows us to write, for  $-\infty < q < 0$ ,

$$\frac{x}{t} = \frac{1}{(q-1)^2}, \quad \frac{z}{t} = \frac{q^2}{(q-1)^2} \quad (6.6)$$

Eliminating the single parameter  $q$  from (6.6), we recover the known result  $\sqrt{x} + \sqrt{z} = \sqrt{t}$  for the intersection of the 3d interface with the  $y = 0$  plane.

For the general hyperbolic partial differential equation

$$F(z, t, x, y, p, q, r) = 0,$$

the characteristics equations are

$$\begin{aligned}\frac{dt}{ds} &= F_p \\ \frac{dx}{ds} &= F_q \\ \frac{dy}{ds} &= F_r \\ \frac{dz}{ds} &= pF_p + qF_q + rF_r \\ \frac{dp}{ds} &= -F_t - pF_z \\ \frac{dq}{ds} &= -F_x - qF_z \\ \frac{dr}{ds} &= -F_y - rF_z\end{aligned}$$

Rewriting the governing equation as

$$F = p - \frac{q}{q-1} \frac{r}{r-1} \left( 1 - \frac{1}{q+r} \right) = 0,$$

we find  $t = s$ , and the interface velocity  $p$  as well as the two spatial derivatives  $q$  and  $r$  are all constant along the characteristics. Physically, the characteristics are rays emanating from the origin defined by

$$ax = by = z = ct$$

Thus for any choice  $a$  and  $b$ , the interface recedes at constant velocity  $dz/dt = c$ , and the slopes  $q$  and  $r$  are constant in time. Thus, the characteristics equations further reduce to

$$\frac{x}{t} = A(q, r), \quad \frac{y}{t} = B(q, r), \quad \frac{z}{t} = C(q, r) \quad (6.7)$$

where

$$\begin{aligned}
 A &= \frac{1}{(q-1)^2} \frac{r}{r-1} \left[ 1 - \frac{1}{q+r} \right] - \frac{q}{q-1} \frac{r}{r-1} \frac{1}{(q+r)^2} \\
 B &= \frac{q}{q-1} \frac{1}{(r-1)^2} \left[ 1 - \frac{1}{q+r} \right] - \frac{q}{q-1} \frac{r}{r-1} \frac{1}{(q+r)^2} \\
 C &= \frac{q}{q-1} \frac{r}{r-1} \left[ 1 - \frac{1}{q+r} \right] \left[ 1 + \frac{1}{q-1} + \frac{1}{r-1} \right] \\
 &\quad - \frac{q}{q-1} \frac{r}{r-1} \frac{1}{q+r}
 \end{aligned}$$

and the parameters  $q = z_x$  and  $r = z_y$  vary on the interval  $-\infty < q, r \leq 0$ . This is a full parametric solution of the 3d governing equation (6.5) for the interface shape for an initially empty corner.

As a check of consistency, note that for  $r = -\infty$ , we have  $x/t = (q-1)^{-2}$ ,  $y/t = 0$ ,  $z/t = q^2(q-1)^{-2}$ . Eliminating  $q$  we get  $\sqrt{x} + \sqrt{z} = \sqrt{t}$ , so we recover Eq. (6.2) for the intersection of the interface (6.7) with the  $y = 0$  plane. The simulated interface is shown in Fig. 6.2(left), and Eq. (6.7) is presented for comparison (Fig. 6.2(right)).

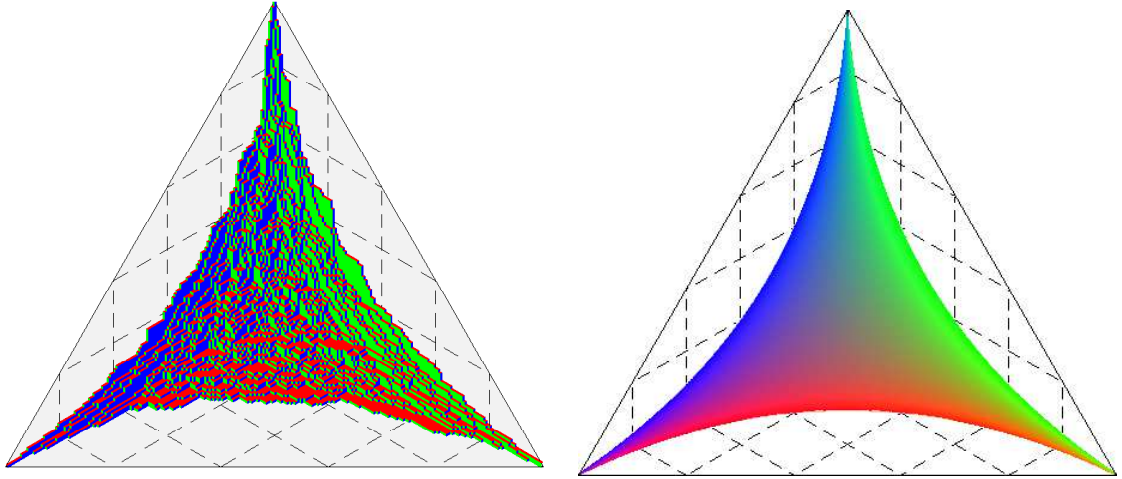


Figure 6.2: (left) The growth process at time  $t = 140$ . (right) The interface (6.7).

We now quantitatively compare our predicted interface shape (6.7) with simulation results. Consider first the position of the middle point on the interface, where  $x = y = z$ .

This point recedes from the origin at a constant velocity  $w$ ,

$$x = y = z = wt.$$

Note that the motion of the middle point is governed by

$$\frac{dz}{dt} = z_t + \frac{dx}{dt}z_x + \frac{dy}{dt}z_y,$$

but at the middle point,  $dx/dt = dy/dt = dz/dt$ . Also, by symmetry,  $z_x = z_y = -1$ , so

$$\frac{dz}{dt} = \frac{z_t}{3}.$$

Using our conjectured form (6.5) for  $z_t$  and substituting  $z_x = z_y = -1$ , we obtain the prediction

$$w = \frac{1}{8} = 0.125.$$

(This can also be obtained directly from Eq. (6.7) by setting  $q = r = -1$ .) Numerically, we measure  $w \approx 0.1261(2)$ , which agrees with our prediction within 0.9%.

As a second test, consider the total crystal volume (i.e., the total number of deposited cubes) after time  $t$ . Since the linear scale of the interface grows ballistically, it follows that  $V = vt^3$ , and we must determine the amplitude  $v$ . Using (6.7) and changing from the physical variables  $(x, y)$  to the parametric coordinates  $(q, r)$ , we obtain

$$v = \int_{-\infty}^0 \int_{-\infty}^0 dq dr C(q, r) \frac{\partial(A, B)}{\partial(q, r)}.$$

This is an elementary but cumbersome integral. We compute the Jacobian  $\frac{\partial(A, B)}{\partial(q, r)}$  and the integral using *Mathematica* to find

$$v = \frac{3\pi^2}{2^{11}} \approx 0.014457.$$

Numerically, we measure  $v \approx 0.01472(3)$ , which agrees with our prediction within 1.8%.

It seems difficult to eliminate the parameters  $q$  and  $r$  from Eq. (6.7) and obtain an



explicit expression for the interface shape in terms of  $(x, y, z)$ . Nonetheless, some lines on the surface may be explicitly solved for. Consider the intersection of the 3d interface with the diagonal plane where  $x = y$ . On this plane,  $q = r$  by symmetry, so Eq. (6.7) reduces to

$$\frac{x}{t} = \frac{1}{2} \frac{z}{t} - \frac{3}{4} \left( \frac{z}{t} \right)^{2/3} + \frac{1}{4}. \quad (6.8)$$

This prediction is an excellent match to simulation data (Fig. 6.3).

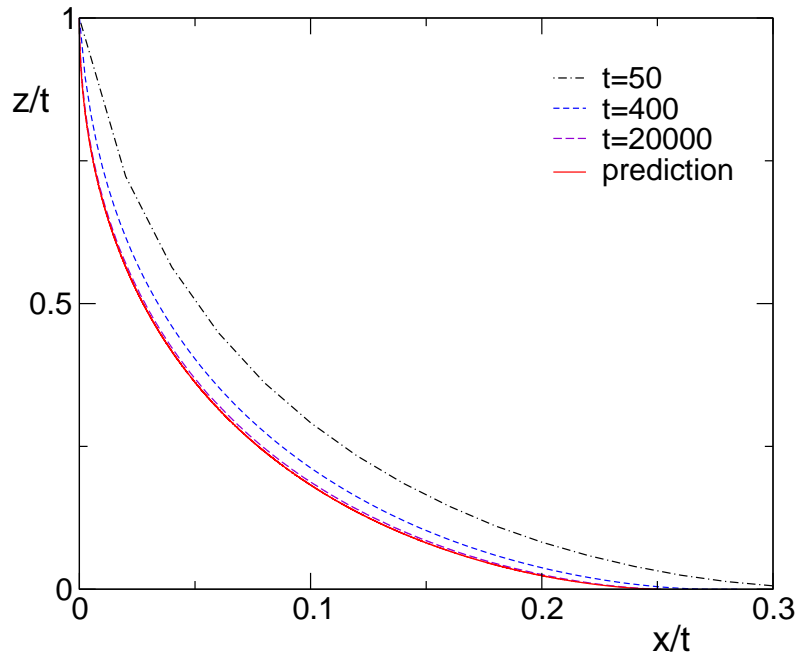


Figure 6.3: The intersection of the interface with the plane  $x = y$ . The simulated curves are shown for  $t = 50, 400,$  and  $20000$ , and the theoretical curve (6.8) is also plotted.

A major challenge is in determining if experimental predictions match the simulational data exactly, or as a highly accurate approximation. The maximum time we ran any simulation to was  $t = 20000$ , and we are still contending with significant finite-size and finite-time effects. In the simulations, the values of the coefficients  $w$  and  $v$  are slightly but significantly larger than their corresponding predicted values.

To treat finite-time effects systematically, we assume that  $w$  and  $v$  are given at finite

times by

$$w(t) = w + w_* t^{-w_\beta}$$

$$v(t) = v + v_* t^{-v_\beta}$$

with the correction exponents  $w_\beta > 0$  and  $v_\beta > 0$  so that in the limit  $t \rightarrow \infty$  the asymptotic values  $w$  and  $v$  are recovered. Our  $3d$  corner growth model is believed to belong to the  $(2+1)$ -dimensional Kardar-Parisi-Zhang (KPZ) universality class of kinetic interface fluctuations [88, 89, 80]. According to the theory of KPZ scaling, the height at the center of the interface (where all spatial coordinates are equal) obeys

$$h(t) = ht + \xi t^\beta$$

where  $\beta$  is the universal KPZ growth exponent and  $\xi$  is a stationary random variable with  $\langle \xi \rangle > 0$ . Dividing by  $t$  and averaging the noise gives

$$w(t) = h(t)/t = w + w_* t^{\beta-1}, \quad (6.9)$$

which suggests that the correction exponent  $w_\beta = -\beta + 1$ .

To find the correction exponent  $v_\beta$ , note that for  $d$ -dimensional corner growth, fluctuations in volume occur over a  $(d-1)$ -dimensional surface area and have width  $t^\beta$ :

$$V(t) = V t^d + \xi t^{d-1+\beta}$$

Again, dividing by  $t^d$  and averaging the noise, we get

$$v(t) = V(t)/t^d = v + v_* t^{\beta-1}, \quad (6.10)$$

so we find  $v_\beta = -\beta + 1$ .

Eq. (6.9) was proven for some growing one-dimensional interfaces in [90], while our growing surface is two-dimensional. Yet we anticipate (6.9) and (6.10) to hold in our model as well. The values of the KPZ growth exponents  $\beta_1$  and  $\beta_2$  for 1- and 2-dimensional

surfaces are  $1/3$  and  $\approx 0.23$ , respectively [75, 90, 91, 92]. Thus we anticipate  $w_\beta$  to equal  $2/3$  and  $\approx 0.77$  for two- and three-dimensional corner growth, respectively.

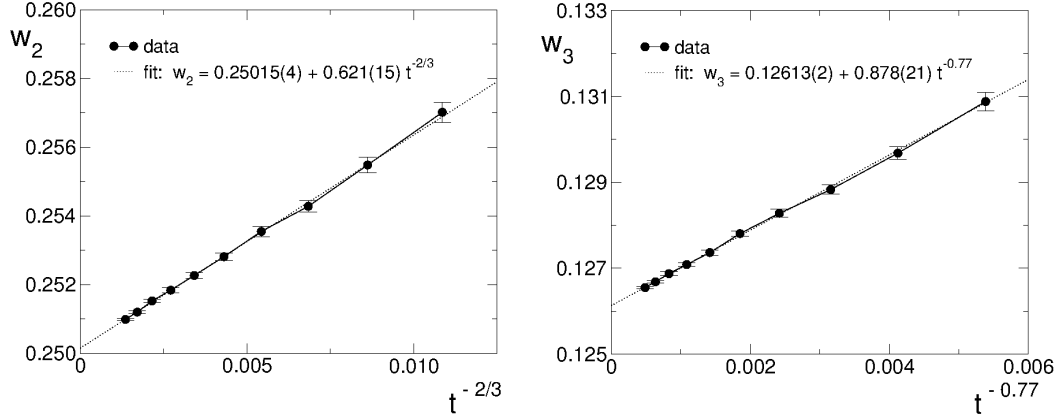


Figure 6.4: (left) The coefficient  $w_2(t)$ . (right) The coefficient  $w_3(t)$ .

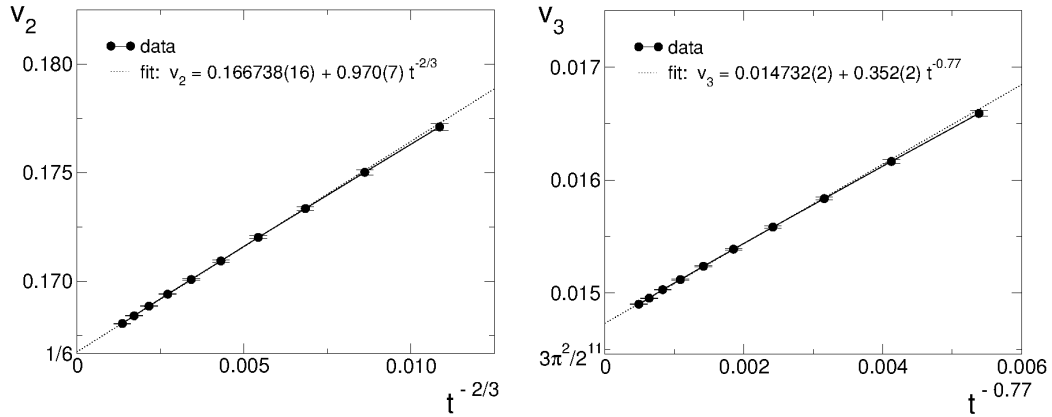


Figure 6.5: (left) The coefficient  $v_2(t)$ . (right) The coefficient  $v_3(t)$ .

The data for the coefficients  $w(t)$  and  $v(t)$  show high linear correlation in each case ( $r > 0.999$ ); also the data is over a fairly narrow time range ( $t = 884$  to  $t = 20000$ ). The asymptotic values  $w$  and  $v$  in  $2d$  are  $1/4$  and  $1/6$ , respectively. Note that the errors in the extrapolated values of  $w$  and  $v$  are roughly an order of magnitude larger in  $3d$ , making it doubtful that our predictions are exact results. (The errors quoted in this section were obtained by a direct weighted linear regression, so they are likely too small. Multiplying these errors by a factor of ten makes the  $2d$  extrapolations agree well with their theoretically

exact values, so the  $3d$  extrapolated errors may be safely multiplied by a factor of ten.) The highest linear correlation  $r$  for the three-dimensional coefficients  $w(t)$  and  $v(t)$  was obtained by plotting  $w(t)$  versus  $t^{-0.742}$  ( $r = 0.9996$ ) and by plotting  $v(t)$  versus  $t^{-0.732}$  ( $r = 0.99998$ ). These correction exponents are strikingly close to the estimate  $v_\beta = 0.77$  obtained from KPZ theory, and the resulting extrapolated values  $w = 0.12609(2)$  and  $v = 0.014709(3)$  still differ significantly from theoretical predictions.

### 6.3 Alternate Evolution Equations and Extensions to Higher Dimensions

While it is conceivable that some slow decorrelation effect is making the approach to the asymptotic state unexpectedly slow [93, 94], it seems more plausible that our theory is an excellent approximation. We made a highly educated guess to arrive at Eq. (6.5), using limiting behavior, symmetry constraints, and a single well-chosen measurement as clues. Deriving this equation from the stochastic dynamics, even as an approximation (if it is an approximation), is a tall order. In lieu of a derivation, we proceed by establishing some theoretical justification for our evolution equation.

Consider the one-parameter family of equations

$$z_t = \frac{z_x}{z_x - 1} \frac{z_y}{z_y - 1} \frac{z_x + z_y + \lambda}{z_x + z_y}. \quad (6.11)$$

If (6.11) is to describe corner growth, then this equation must imply

$$x_t = \frac{x_y}{x_y - 1} \frac{x_z}{x_z - 1} \frac{x_y + x_z + \lambda}{x_y + x_z}. \quad (6.12)$$

Applying the relations  $z_x = 1/x_z$ ,  $z_y = -z_x x_y$ , and  $z_t = -z_x x_t$ , (6.11) becomes

$$x_t = \frac{x_y}{x_y - 1} \frac{x_z}{x_z - 1} \frac{x_y - \lambda x_z - 1}{x_y + x_z}. \quad (6.13)$$

We see that the choice  $\lambda = -1$  is required by symmetry constraints, and we arrive at our

original guess (6.5).

Taking this analysis further, consider the infinite-parameter family of evolution equations

$$z_t = \frac{z_x}{z_x - 1} \frac{z_y}{z_y - 1} \sum_{n=-\infty}^{\infty} \frac{\lambda_n}{(z_x + z_y)^n}. \quad (6.14)$$

Note that the evolution equation must be analytic on the boundaries of the interface, where  $z_x = -\infty$  (for  $x = 0$ ) and  $z_y = -\infty$  (for  $y = 0$ ). This forces all  $\lambda_{n < 0} = 0$ . The requirement that (6.14) reduces to the two-dimensional form  $z_x/(z_x - 1)$  and  $z_y/(z_y - 1)$  on the boundaries fixes  $\lambda_0 = 1$ . Also, for (6.14) to obey the symmetry constraints, we must have  $\lambda_1 = -1$  and  $\lambda_{n > 1} = 0$ . Thus our original educated guess, Eq. (6.5), is the only equation in the class of equations (6.14) that is appropriate for describing corner growth.

Nonetheless, Eq. (6.5) is not the only properly invariant evolution equation suitable for describing hypercube stacking. Consider the following equation:

$$z_t = \frac{z_x}{z_x - 1} \frac{z_y}{z_y - 1} \left[ 1 + \frac{1}{z_x z_y - z_x - z_y} \right]. \quad (6.15)$$

Although this form looks more complicated than (6.5), it can be written in a simpler form by replacing derivatives with their reciprocals:

$$\frac{1}{z_t} = 1 - \frac{1}{z_x} - \frac{1}{z_y}. \quad (6.16)$$

This is an alternate evolution equation in  $3d$  that satisfies all theoretical requirements for describing the corner growth process. Surprisingly, the solution to this equation is a straightforward generalization of the limiting shape for two-dimensional corner growth:

$$\sqrt{x} + \sqrt{y} + \sqrt{z} = \sqrt{t}. \quad (6.17)$$

The corresponding predictions based on this surface profile,  $w_3 = 1/9$  and  $v_3 = 1/90$ , substantially disagree with simulation results, suggesting that (6.15) is wrong.

It is difficult to find any other simple evolution equations that satisfy all theoretical

constraints. We may further conjecture two composite forms for the evolution equation: an additive family

$$z_t = \frac{z_x}{z_x - 1} \frac{z_y}{z_y - 1} \left[ 1 - \frac{1 + c_a}{z_x + z_y} - \frac{c_a}{z_x z_y - z_x - z_y} \right]$$

and a multiplicative family

$$z_t = \left[ \frac{1 - \frac{1}{z_x + z_y}}{\left(1 - \frac{1}{z_x}\right) \left(1 - \frac{1}{z_y}\right)} \right]^{1+c_m} \left[ 1 - \frac{1}{z_x} - \frac{1}{z_y} \right]^{c_m}.$$

These are valid evolution equations in  $3d$ . The best fit to the measured value of  $v_3$  is provided by choosing  $c_a = 0.079$  for the additive family of equations, and by choosing  $c_m = 0.074$  for the multiplicative family of equations. However, such anomalously small values for the parameters  $c_a$  and  $c_m$  suggest that these conjectured composite forms are highly accurate approximations rather than exact results.

We have found even more esoteric equations that satisfy all requirements for describing corner growth in three dimensions. For example, consider the equation

$$z_t = \left[ \frac{1 - \frac{1}{z_x + z_y}}{\left(1 - \frac{1}{z_x}\right) \left(1 - \frac{1}{z_y}\right)} \right]^{1+c_1} \left[ 1 - \frac{1}{z_x} - \frac{1}{z_y} \right]^{c_1} \left[ \frac{(1 - z_x - z_y)^n}{1 + (-z_x)^n + (-z_y)^n} \right]^{c_2}$$

with two fitting parameters  $c_1$  and  $c_2$ . Consider also the equation

$$z_t = \left[ \frac{1 - \frac{1}{z_x + z_y}}{\left(1 - \frac{1}{z_x}\right) \left(1 - \frac{1}{z_y}\right)} \right]^{1+c_3} \left[ 1 - \frac{1}{z_x} - \frac{1}{z_y} \right]^{c_3} \left[ \frac{(1 - z_x - z_y)^n + c_5(z_x z_y)^{n/3}}{1 + (-z_x)^n + (-z_y)^n + c_6(z_x z_y)^{n/3}} \right]^{c_4}$$

with fitting parameters  $c_3$ ,  $c_4$ ,  $c_5$ , and  $c_6$ . Both of these equations also satisfy all theoretical symmetry requirements and reduce to the correct limits.

One finds that there are infinitely many valid evolution equations. One can, in principle, construct an arbitrarily complex equation and tune fitting parameters to obtain agreement with simulation data to the desired accuracy.

Perhaps the hypercube stacking problem for three- and higher-dimensional interfaces cannot be described by a simple function of  $z_x$  and  $z_y$ . The corner growth problem in  $d = 2$

is solvable because the underlying exclusion process has stationary product measure—a non-generic feature of  $1d$  ASEP. In  $d = 3$ , corner growth can be mapped onto a  $2d$  hexagonal lattice covered with three distinct types of rhombi. The deposition of an elemental cube corresponds in this picture to a cyclic rearrangement of three adjacent rhombi, and the problem of mathematically deriving an equation of motion from these stochastic dynamics seems intractable. If indeed there is no closed-form exact governing equation for the interface profile, then the aesthetically simple and highly accurate guess, Eq. (6.5), is quite intriguing.

Mathematically, one may consider stacking of  $d$ -dimensional hypercubes inside an initially-empty  $d$ -dimensional corner in any spatial dimension  $d$ . Such an extension of the  $2d$  and  $3d$  models is rather abstract without any obvious connection to physics. Nonetheless, the mathematical problem of generalizing our three-dimensional governing equations to higher dimensions naturally presents itself.

Similarly to the three-dimensional corner growth problem, we have not made any formal derivations from the stochastic dynamics. To make progress, we begin by writing Eq. (6.5) in the somewhat suggestive form

$$z_t = \frac{1 - \frac{1}{z_x + z_y}}{\left(1 - \frac{1}{z_x}\right) \left(1 - \frac{1}{z_y}\right)}.$$

Note that the right-hand side of this equation contains factors of the form  $(1 - 1/X)$ , where  $X$  represents a sum of partial derivatives. With the clue that the  $4d$  governing equation must be manifestly symmetric in three of the four spatial coordinates ( $x$ ,  $y$ ,  $z$ , and  $h$ ), we conjecture the form

$$h_t = \frac{\left(1 - \frac{1}{h_x + h_y}\right) \left(1 - \frac{1}{h_y + h_z}\right) \left(1 - \frac{1}{h_z + h_x}\right)}{\left(1 - \frac{1}{h_x}\right) \left(1 - \frac{1}{h_y}\right) \left(1 - \frac{1}{h_z}\right)} A(h_x, h_y, h_z),$$

which contains an unknown function  $A(h_x, h_y, h_z)$ . However, intuition suggests that the

unknown factor should be equal to

$$A(h_x, h_y, h_z) = \frac{1}{1 - \frac{1}{h_x + h_y + h_z}},$$

and we arrive at the following guess for the  $4d$  evolution equation:

$$h_t = \frac{\left(1 - \frac{1}{h_x + h_y}\right) \left(1 - \frac{1}{h_y + h_z}\right) \left(1 - \frac{1}{h_z + h_x}\right)}{\left(1 - \frac{1}{h_x}\right) \left(1 - \frac{1}{h_y}\right) \left(1 - \frac{1}{h_z}\right) \left(1 - \frac{1}{h_x + h_y + h_z}\right)}. \quad (6.18)$$

It is simple to verify that Eq. (6.18) satisfies all theoretical requirements for describing hypercube stacking in four dimensions.

Generally in  $d$  dimensions, the same line of reasoning suggests that the height  $h(x_1, \dots, x_{d-1}; t)$  obeys

$$h_t = \prod_{1 \leq i_1 < \dots < i_p \leq d-1} \left(1 - \frac{1}{h_{i_1} + \dots + h_{i_p}}\right)^{(-1)^p} \quad (6.19)$$

For  $4d$  corner growth, we measure the middle of the interface at  $w \approx 0.084$ , which is roughly 6% greater than our prediction  $3^4/4^5$  based on Eq. (6.18). However, our measurements on  $4d$  corner growth are not as systematic as our measurements in three dimensions. We have not done numerical tests on corner growth in dimensions  $d > 4$ , and we leave these equations as conjectures. It is possible that the higher-dimensional equations become progressively worse approximations for describing hypercube stacking as the spatial dimension  $d$  is increased. A generalization of Eq. (6.16) to  $d$  dimensions is straightforward:

$$\frac{1}{h_t} = 1 - \sum_{i=1}^{d-1} \frac{1}{h_i} \quad (6.20)$$

Using (6.19) and (6.20), we may construct an additive family

$$h_t = (1 + c) \left[ \prod_{1 \leq i_1 < \dots < i_p \leq d-1} \left(1 - \frac{1}{h_{i_1} + \dots + h_{i_p}}\right)^{(-1)^p} \right] - c \left[ 1 - \sum_{i=1}^{d-1} \frac{1}{h_i} \right]^{-1}$$



and a multiplicative family

$$h_t = \left[ \prod_{1 \leq i_1 < \dots < i_p \leq d-1} \left( 1 - \frac{1}{h_{i_1} + \dots + h_{i_p}} \right)^{(-1)^p} \right]^{1+c} \left[ 1 - \sum_{i=1}^{d-1} \frac{1}{h_i} \right]^c$$

of evolution equations for describing corner growth in  $d$  dimensions.

## 6.4 Geometrical Characteristics of the Interface

We briefly discuss the total numbers of inner and outer corners on the interface. By definition, cubes are added to inner corners and desorbed from outer corners. In Figure 6.1, for example, there are six inner corners and three outer corners. Let  $N_+$  and  $N_-$  denote the numbers of inner and outer corners, respectively. There are four simple cases to consider: pure growth dynamics and Ising dynamics, each in both the two- and three-dimensional settings.

We first consider the growth dynamics. By definition,  $N_+ = dV_d/dt$ , which gives

$$N_+ = dv_d t^{d-1}$$

as the leading asymptotic behavior. In  $2d$ , the conservation law

$$N_+ - N_- = 1 \quad (2d).$$

holds at all times in the evolution. In greater than two dimensions, however, we can say nothing analytically about  $N_-$ . One may anticipate that  $N_+ > N_-$  in  $3d$ , since the interface is macroscopically concave. While our data suggests that  $N_+$  and  $N_-$  both grow as  $t^2$  to leading order, we surprisingly find that the difference  $N_+ - N_- < 0$  and diverges as  $t \rightarrow \infty$ .

We find

$$\langle N_+ \rangle = C_+ t^2, \quad C_+ = 0.0442(2)$$

$$\langle N_- \rangle = C_- t^2, \quad C_- = 0.0459(2)$$

In Figure 6.6, we see that  $N_-/N_+$  converges to a value greater than 1 in the long-time limit.

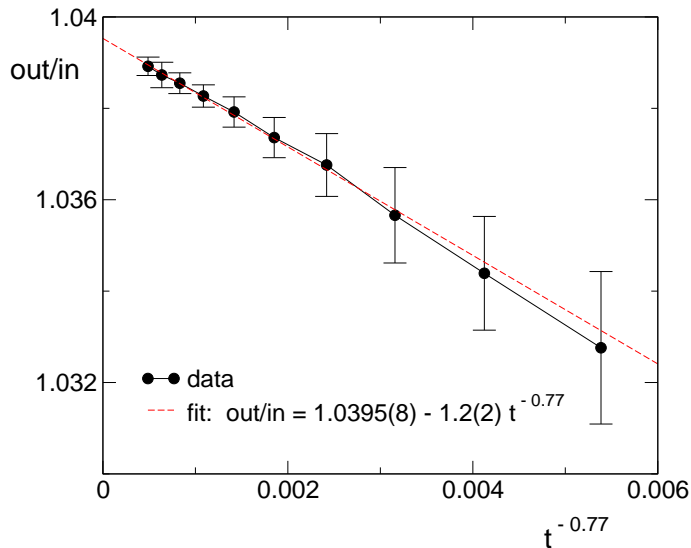


Figure 6.6: The ratio  $N_-/N_+$  versus  $t^{-0.77}$ . This quantity appears to exceed 1 as  $t \rightarrow \infty$ .

This result seems paradoxical: How can the number of outer corners on the interface exceed the number of inner corners if the interface is globally concave? Figure 6.7 aids in our understanding. In the image at left, we have a flat plane that extends to infinity in all directions with exactly equal numbers of inner and outer corners. In this case,  $N_+ = N_-$  seems like an intuitively obvious result. Now consider the image at right. We've made a small dimple at each outer corner on the infinite plane, so that now  $N_-/N_+ = 3/2$ . Even though  $N_- > N_+$ , the plane is still macroscopically flat! This illustration shows that, in general, the statistics of inner and outer corners on an interface cannot be directly inferred from the interface's macroscopic geometry.

## 6.5 Discussion

The accurate description of the  $3d$  corner growth model with simple mathematics highlights the power of using limits, symmetries, and well-chosen numerical clues to tackle otherwise intractable problems. While our equations probably form an approximate description of

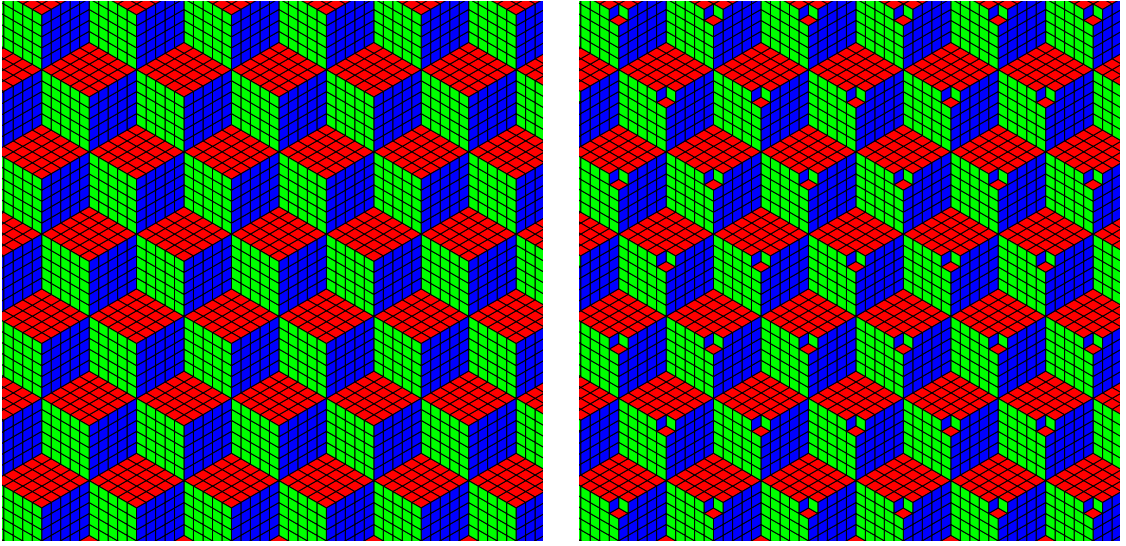


Figure 6.7: Illustration showing how the numbers of inner and outer corners can be unequal for a flat plane. (left) A flat interface with equal numbers of inner and outer corners. (right) A flat interface with three outer corners for every two inner corners.

higher-dimensional corner growth, the agreement between theory and simulation is outstanding. From an experimental context, can our equations accurately describe crystal growth phenomena? If one constructed a concave corner substrate and introduced some deposition process, would the limiting shape of a physical growing cubic crystal mimic the idealized shape we see from simulations? We can also consider the dual interpretation of the interface growth process: Beginning with a perfect macroscopic cubic crystal in three dimensions, and introducing some mechanism for erosion, the corner will gradually smooth. How closely is an eroding cubic crystal corner mathematically described by our  $3d$  interface growth equations (Figure 6.8)?

The understanding of Kardar-Parisi-Zhang interfacial fluctuations in  $3d$  growth models is in its nascent stages. Aside from elementary relations between scaling exponents for statistics of interface observables [88, 95, 96, 97, 91], almost nothing is known analytically about the  $(2+1)$ -dimensional KPZ universality class [80, 98]. Incidentally, our equations of motion provide a highly accurate approximation for the characteristic directions of  $3d$  corner growth. Do temporal correlations [99, 100] in interface height statistics decay differently

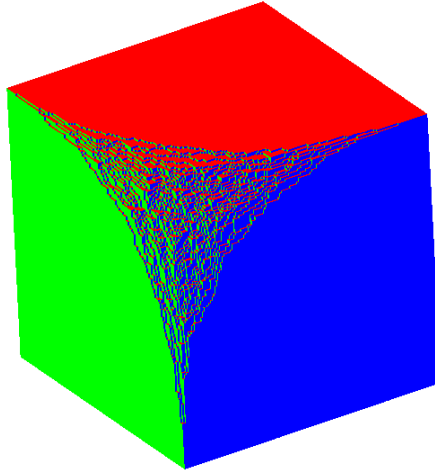


Figure 6.8: A 3d cubic crystal eroding from a corner.

along the characteristic directions predicted by our growth equations? How rapidly do temporal correlations in height fluctuations decay in time as the interface grows? Our phenomenological theory may help shed light on these issues.

One wonders if similarly nonrigorous approaches will yield conjecturally exact predictions for other theoretical growth models in higher dimensions. Recall the corner growth process in two dimensions with unbiased dynamics (Equation (5.7)). More physically, the equation of motion in this case is

$$y_t = \frac{y_{xx}}{(y_x - 1)^2}.$$

Can a similar equation be found for unbiased corner growth in three dimensions? A recent conjecture by Krapivsky for the 3d corner growth process in which elemental cubic crystals may be both adsorbed and desorbed is based on similar phenomenology [73]:

$$z_t = \frac{\left(1 - \frac{1}{z_x + z_y}\right)^2}{\left(1 - \frac{1}{z_x}\right)^2 \left(1 - \frac{1}{z_y}\right)^2} \left[ \frac{z_{xx}}{z_x^2} + \frac{z_{yy}}{z_y^2} - \frac{z_{xy}}{z_x z_y} \right].$$

This equation was constructed so that the interface growth rate is linear in the local curvature of the interface, just as in the two-dimensional unbiased corner growth process. The

factor in front is not unique. For example, we could just as well write

$$z_t = \frac{1}{\left(1 - \frac{1}{z_x} - \frac{1}{z_y}\right)^2} \left[ \frac{z_{xx}}{z_x^2} + \frac{z_{yy}}{z_y^2} - \frac{z_{xy}}{z_x z_y} \right],$$

which also satisfies all theoretical requirements of unbiased corner growth. We have had trouble extracting clean predictions from these equations, however, so they remain numerically untested. The description of the equilibrium crystal [83], in which the rate of desorption from the interface slightly exceeds the rate of adsorption, remains a tantalizing unsolved problem in greater than three spatial dimensions.

## Chapter 7

### Concluding Remarks

A central theme of this dissertation is the existence of a vast number of metastable states into which a zero-temperature kinetic spin system can freeze. A  $3d$  Ising model quenched to zero temperature always features two highly intertwined clusters that produce a sponge-like final state. The gyroid phases are nonstatic, having blinker spins on domain interfaces that flip forever stochastically and with no energy cost. These blinker states additionally generate a mechanism for extremely slow relaxation. In a typical quench, we observe isolated drops in energy at extraordinarily late times, well after the global domain structure has been established. The paradigmatic Ising model in its original form continues to wonderfully surprise us nearly a century after its conception.

Can results from percolation theory help us understand the inevitable freezing that occurs when a large  $3d$  ferromagnet is quenched to  $T = 0$ ? While analytical results for continuum percolation in  $d > 2$  are lacking, the critical percolation density has numerically been observed to be less than  $1/2$ . In a supercritical initial state, where both phases occupy equal fractions of the system, percolation of both phases shortly after a deep quench is guaranteed. (Even at time  $t = 0$ , a supercritical state is guaranteed to have percolating clusters because the threshold for site percolation on a cubic lattice is less than  $1/2$ .) This may help to explain why the  $3d$  Ising model at  $T = 0$  freezes into a complex domain structure with probability one as  $L \rightarrow \infty$ . What if the  $3d$  Ising model is prepared in an initial state with unequal densities of the two phases? Our simulations suggest that for

any tiny difference in densities of the plus and minus phases, the system will quickly reach the ground state of the phase that is initially in the majority. Curvature-driven flow in three dimensions likely makes any metastable cluster pattern with uneven initial condition unstable. This may shed light on why the ground state in the thermodynamic limit is apparently always reached.

One wonders why a  $T = 0$  TDGL system in  $3d$ , quenched from a disordered state with equal densities of the two phases, always reaches one of the two ground states. Shortly after the quench, the system consists of two complex and interconnected domains that span the system in all three directions, as would be predicted from percolation theory in  $3d$ . However, in  $3d$  curvature-driven TDGL coarsening, topologically-complex domains are unstable with respect to non-volume-preserving perturbations [54]. While the states of both a  $3d$  Ising model and a  $3d$  TDGL system may be statistically similar shortly after a zero-temperature quench, it is precisely the discrete, nearest-neighbor spin-spin interactions that cause the  $3d$  Ising system to freeze. Fortuitously, in  $2d$  TDGL evolution, spanning clusters at early times in the evolution are stable to perturbations, so the topology at a time shortly after the quench determines the ultimate zero-temperature fate of the system.

Our studies of nonconserved coarsening in the  $2d$  Potts model similarly reveal a cornucopia of intricate metastable states. We also observe an unexpected phenomenon: A ground state of one of the multiple phases is reached with nonzero probability in the thermodynamic limit. The apparent freezing into a complex cluster mosaic that occurs for small system sizes has been an enigma in prior studies of the kinetic Potts model. However, we've revealed an avalanching mechanism that qualitatively resembles bootstrap percolation. It would be interesting to see if the Potts model on the square lattice reaches a ground state with probability one in the thermodynamic limit.

Indeed, the universality in the special case of  $2d$  nonconservative coarsening with a doubly-degenerate ground state is quite remarkable. For years, it was generally accepted that coarsening of a scalar order parameter in two dimensions is too complex to admit a tractable analytical understanding. We now appear to have an exact mapping between

nonconserved two-state coarsening in  $2d$  and critical continuum percolation, but the precise nature of the connection between these systems is unresolved. Mathematical physicists have shown that, for a broad class of random potentials, crossing probabilities in continuum percolation models are universal [13]. This universality of continuum critical percolation statistics for different random fields may help explain the universality of nonconserved  $2d$  coarsening.

Open questions in  $2d$  scalar coarsening remain. How broad is its universality class? To what extent can we modify model parameters without observing different cluster size statistics and/or stripe state probabilities? More fundamentally, can any aspect of coarsening with a conserved order parameter be understood from percolation theory? Conserved coarsening at late times is driven by diffusion of the order parameter—not simply by domain wall curvature—and therefore the domain topology at early times in the kinetics is not necessarily invariant [14].

We also examined interface growth starting from smooth, deterministic initial conditions. We derived exact equations of motion for growth in  $2d$  with NN and NNN spin interactions via mapping onto a simple exclusion process. We also constructed beautifully symmetric equations as approximations for interface growth in  $3d$ , and we presented generalizations of our equations to higher spatial dimensions.

Open problems abound in the field of interface shapes and statistics. As an example, finding the limiting shape of an equilibrium crystal in greater than three spatial dimensions is a tantalizing mathematical question. Our extensive analytical massaging and educated guesswork delivered an outstanding approximation for three-dimensional interface growth inside a corner. Will anyone succeed in finding the exact formula for counting multi-dimensional Young diagrams? Does such a formula even exist? If so, can the limiting shape of an equilibrium crystal be analytically computed in higher dimensions? One wonders if a similarly sophisticated consideration of limiting behavior, symmetry constraints, and a small number of well-chosen numerical clues will help deliver answers to these questions.



# Appendices

# Appendix A

## Acceleration Algorithm for the Zero-Temperature $3d$ KIM

To test our acceleration algorithm, we evolve the system with unbiased Glauber dynamics until a cutoff time  $\tau$ . We then apply an infinitesimal bias magnetic field that drives the system so that drops in energy occur more quickly. The bias magnetic field reverses direction after each energy drop until the system reaches its lowest-energy configuration. Table A.1 gives the average final energy  $E_L$  as a function of cutoff time  $\tau$ . The final energy depends extremely weakly on cutoff time, which indicates the accuracy of our acceleration algorithm. The data for  $L = 10, 20,$  and  $100$  are based on  $10^7, 10240,$  and  $128$  realizations, respectively. The last column  $R$  gives the ratio of the computing time needed to run a system to  $t = \tau$  before applying the bias field over the computing time needed to run a system to  $t = 5L^2$  before applying the bias field. For instance, it took 67 times longer to run a  $L = 100$  system to  $t = 10^7$  and apply the bias field than it took to run a  $L = 100$  system to  $t = 5L^2$  and apply the bias field. The relative difference in energies for these two protocols is  $5 \times 10^{-5}$ . This weak dependence of the the final energy on cutoff time  $\tau$  is our justification for use of the acceleration algorithm.

$L$	$\tau$	$E_L$	$R$
10	500	.4245900960	
	$10^9$	.4245901020	34
	$10^{10}$	.4245901020	60
20	2000	.283285352	
	$10^5$	.283287939	1.4
	$10^6$	.283287939	5.2
	$10^7$	.283287939	39
	$10^8$	.283288232	378
100	$5 \times 10^4$	.083666469	
	$10^5$	.083663406	1.2
	$5 \times 10^5$	.083662656	4.7
	$10^6$	.083662594	7.2
	$10^7$	.083662531	67

Table A.1: Average final energies  $E_L$  for different cutoff times  $\tau$  and system sizes  $L$ .

## Appendix B

### The 3d KIM: Small Systems, Number of Clusters, Blinker States

The  $L = 2$  system with antiferromagnetic initial state helps to illustrate the complexities of much larger systems. For  $L = 2$ , we have enumerated all 9 possible paths to the final state—either the ferromagnetic state (F) or a metastable slab state (M) (Table B.1). The latter state consists of a square of four spins of one sign adjacent to a square of four spins of the opposite sign. The average survival time of the  $L = 2$  system is  $221/120 = 1.841666\dots$ , and the probability of reaching the F final state is  $11/14$ .

Direct enumerations for larger systems are not feasible, but our data strongly suggests that all realizations end in blinker states as  $L \rightarrow \infty$  (Table B.2). Amazingly, the smallest value of  $L$  that supports blinker states is  $L = 5$  (though this system has an odd number of spins, so an initial state with exactly zero magnetization is not possible). Table B.3 shows the probabilities of coarsening into states with different numbers of clusters for different  $L$ . It appears that, while blinker states are always reached in the thermodynamic limit, these blinker states are supported by only two highly entangled clusters that each span the lattice.

Path	# of Flips	Time	Probability	Final State
1	4	43/56	2/21	M
2	4	143/168	1/14	M
3	6	341/280	1/21	M
4	4	85/56	3/14	F
5	6	1583/840	1/35	F
6	6	1793/840	4/35	F
7	6	127/56	4/21	F
8	6	395/168	1/7	F
9	8	761/280	2/21	F

Table B.1: The nine possible paths to the final state for an  $L = 2$  system, starting from the antiferromagnetic state.

$L$	$P_g$	$P_f$	$P_b$
2	11/14	3/14	0
4	0.6814(1)	0.3186(1)	0
6	0.3523(2)	0.6353(2)	0.01246(4)
8	0.1842(1)	0.7373(1)	0.07853(9)
10	0.1045(1)	0.7170(1)	0.1785(1)
20	0.01377(4)	0.3059(1)	0.6803(1)
32	0.00322(8)	0.1091(4)	0.8877(4)
54	0.00066(6)	0.0406(4)	0.9587(4)
76	0.00040(6)	0.0250(5)	0.9746(5)
90	0.00039(6)	0.0199(4)	0.9797(4)

Table B.2: Probability of reaching a ground state  $P_g$ , a frozen state  $P_f$ , or a blinker state  $P_b$  versus  $L$  following a quench from the antiferromagnetic initial state.

$L$	$P(1)$	$P(2)$	$P(3)$	$P(> 3)$
2	11/14	3/14	0	0
4	0.6814(1)	0.3186(1)	0	<0.0000001
6	0.3523(2)	0.6475(2)	0.000245(5)	<0.0000001
8	0.1842(1)	0.8128(1)	0.00303(2)	0.0000004(2)
10	0.1045(1)	0.8866(1)	0.00893(3)	0.000015(1)
20	0.01377(4)	0.96052(6)	0.02475(5)	0.00096(1)
32	0.00322(8)	0.9720(2)	0.0230(2)	0.00180(6)
54	0.00066(6)	0.9802(3)	0.0171(3)	0.0020(1)
76	0.00040(6)	0.9824(4)	0.0150(4)	0.0022(1)
90	0.00039(6)	0.9839(4)	0.0133(4)	0.0024(2)

Table B.3: Probability of reaching a state with one cluster, two clusters, three clusters, or greater than three clusters versus  $L$  following a quench from the antiferromagnetic initial state.

# Bibliography

- [1] E. Ising. Beitrag zur theorie des ferromagnetismus [Contribution to the theory of ferromagnetism] (in German). *Zeitschrift fur Physik*, 31(1):253, 1925.
- [2] R. Peierls. On Ising's Model of Ferromagnetism. *Proceedings of the Cambridge Philosophical Society*, 32(3):477, 1936.
- [3] L. Onsager. Crystal Statistics. I. A Two-Dimensional Model with an Order-Disorder Transition. *Physical Review*, 65:117, 1944.
- [4] P. L. Krapivsky, S. Redner, and E. Ben-Naim. *A Kinetic View of Statistical Physics*. Cambridge University Press, Cambridge, 2010.
- [5] A. J. Bray. Theory of phase-ordering kinetics. *Advances in Physics*, 43:357, 1994.
- [6] S. M. Allen and J. W. Cahn. A Microscopic Theory for Antiphase Boundary Motion and Its Application to Antiphase Domain Coarsening. *Acta Metallurgica*, 27:1085, 1979.
- [7] V. Spirin, P. L. Krapivsky, and S. Redner. Fate of zero-temperature Ising ferromagnets. *Physical Review E*, 63:036118, 2001.  
  
V. Spirin, P. L. Krapivsky, and S. Redner. Freezing in Ising ferromagnets. *Physical Review E*, 65:016119, 2001.
- [8] D. Stauffer and A. Aharony. *Introduction to Percolation Theory*. Taylor and Francis, London, 1992.

- [9] X. Feng, Y. Deng, and H. W. J. Blote. Percolation transitions in two dimensions. *Physical Review E*, 78:031136, 2008.
- [10] J. L. Cardy. Critical percolation in finite geometries. *Journal of Physics A*, 25:L201, 1992.
- [11] H. T. Pinson. Critical percolation on the torus. *Journal of Statistical Physics*, 75:1167, 1994.
- [12] G. Pruessner and N. R. Moloney. Numerical results for crossing, spanning, and wrapping in two-dimensional percolation. *Journal of Statistical Physics*, 115:839, 2004.
- [13] R. Zallen and H. Scher. Percolation on a Continuum and the Localization-Delocalization Transition in Amorphous Semiconductors. *Physical Review B*, 4:4471, 1971.
- [14] J. J. Arenzon, A. J. Bray, L. F. Cugliandolo, and A. Sicilia. Exact Results for Curvature-Driven Coarsening in Two Dimensions. *Physical Review Letters*, 98:145701, 2007.
- [15] K. Barros, P. L. Krapivsky, and S. Redner. Freezing into stripe states in two-dimensional ferromagnets and crossing probabilities in critical percolation. *Physical Review E*, 80:040101(R), 2009.
- [16] J. Cardy and R. M. Ziff. Exact Results for the Universal Area Distribution of Clusters in Percolation, Ising, and Potts Models. *Journal of Statistical Physics*, 110:1, 2003.
- [17] G. M. T. Watts. A crossing probability for critical percolation in two dimensions. *Journal of Physics A*, 29:L363, 1996.
- [18] J. J. H. Simmons, P. Kleban, and R. M. Ziff. Percolation crossing formulae and conformal field theory. *Journal of Physics A*, 40:F771, 2007.
- [19] S. Smirnov. Critical percolation in the plane: conformal invariance, Cardy's formula, scaling limits. *Comptes Rendus de l'Academie des Sciences*, 333:239, 2001.

- O. Schramm. A Percolation Formula. *Electronic Communications in Probability*, 6:115, 2001.
- J. Dubedat. Excursion decompositions for SLE and Watts' crossing formula. *Probability Theory and Related Fields*, 134:435, 2006.
- [20] M. Abramowitz and I. A. Stegun. *Handbook of Mathematical Functions*. Dover, New York, 1972.
- [21] R. J. Glauber. Time-Dependent Statistics of the Ising Model. *Journal of Mathematical Physics*, 4:294, 1963.
- [22] N. Metropolis, A. W. Rosenbluth, M. N. Rosenbluth, A. H. Teller, and E. Teller. Equation of State Calculations by Fast Computing Machines. *Journal of Chemical Physics*, 21:1087, 1953.
- [23] D. R. Cox and H. D. Miller. *The theory of stochastic processes*. 1965.
- W. M. Young and E. W. Elcock. Monte Carlo studies of vacancy migration in binary ordered alloys: I. *Proceedings of the Physical Society*, 89:735, 1966.
- [24] D. T. Gillespie. A General Method for Numerically Simulating the Stochastic Time Evolution of Coupled Chemical Reactions. *Journal of Computational Physics*, 22:403, 1976.
- [25] A. B. Bortz, M. H. Kalos, and J. L. Lebowitz. A New Algorithm for Monte Carlo Simulation of Ising Spin Systems. *Journal of Computational Physics*, 17:10, 1975.
- [26] R. L. Graham, D. E. Knuth, and O. Patashnik. *Concrete Mathematics: A Foundation for Computer Science, 2nd ed.* Addison-Wesley, Boston, 1989.
- [27] P. Chen and S. Redner. Majority rule in finite dimensions. *Physical Review E*, 71:036101, 2005.
- [28] X. Castello, A. Baronchelli, and V. Loreto. Consensus and ordering in language dynamics. *European Physical Journal B*, 71:557, 2009.



- [29] D. Volovik and S. Redner. Dynamics of confident voting. *Journal of Statistical Mechanics*, page P04003, 2012.
- [30] A. L. Toom. *Multicomponent Random Systems*. Dekker, New York, 1980.
- [31] P. C. Hohenberg and B. I. Halperin. Theory of dynamic critical phenomena. *Reviews of Modern Physics*, 49:435, 1977.
- [32] J. D. Gunton, M. San Miguel, and P. S. Sahni. *Phase Transitions and Critical Phenomena*, volume 8. Academic Press, New York, 1983.
- [33] E. T. Gawłinski, M. Grant, J. D. Gunton, and K. Kaski. Growth of unstable domains in the two-dimensional Ising model. *Physical Review B*, 31:281, 1985.
- J. Vinals and M. Grant. Role of activated processes and boundary conditions in the domain growth of the Potts model. *Physical Review B*, 36:7036, 1987.
- [34] J. Kurchan and L. Laloux. Phase space geometry and slow dynamics. *Journal of Physics A*, 29:1929, 1996.
- [35] D. S. Fisher. Dynamics and domain walls: Is the “Landscape Paradigm” instructive? *Physica D*, 107:204, 1997.
- [36] R. Morris. Zero-temperature Glauber dynamics on  $Z^d$ . *Probability Theory and Related Fields*, 149:417, 2011.
- [37] D. Stauffer. Ising spinodal decomposition at  $T = 0$  in one to five dimensions. *Journal of Physics A*, 27:5029, 1994.
- [38] P. Sundaramurthy and D. L. Stein. Zero-temperature dynamics of 2D and 3D Ising ferromagnets. *Journal of Physics A*, 38:349, 2005.
- [39] P. M. C. de Oliveira, C. M. Newman, V. Sidoravicius, and D. L. Stein. Ising ferromagnet: zero-temperature dynamic evolution. *Journal of Physics A*, 39:6841, 2006.

- [40] S. Nanda, C. M. Newman, and D. L. Stein. *On Dobrushin's Way (From Probability Theory to Statistical Physics)*. American Mathematical Society, Providence, RI, 2000.
- [41] C. Godreche and J. M. Luck. Metastability in zero-temperature dynamics: statistics of attractors. *Journal of Physics: Condensed Matter*, 17:S2573, 2005.
- [42] F. Ritort and P. Sollich. Glassy dynamics of kinetically constrained models. *Advances in Physics*, 52:219, 2003.
- [43] S. Leibler. *Statistical Mechanics of Membranes and Surfaces*, page 45. World Scientific, Teaneck, NJ, 1989.
- D. M. Anderson and P. Storm. *Polymer Association Structures: Microemulsions and Liquid Crystals*, page 204. ACS Symposium Series No. 384, American Chemical Society, Washington, DC, 1989.
- A. C. Finnefrock, R. Ulrich, G. E. S. Toombes, S. M. Gruner, and U. Wiesner. The Plumber's Nightmare: A New Morphology in Block Copolymer-Ceramic Nanocomposites and Mesoporous Aluminosilicates. *Journal of the American Chemical Society*, 125:13084, 2003.
- M. W. Anderson, C. C. Egger, G. J. T. Tiddy, J. L. Casci, and K. A. Brakke. A New Minimal Surface and the Structure of Mesoporous Silicas. *Angewandte Chemie International Edition*, 44:2, 2005.
- [44] H. A. Schwarz. *Gesammelte Mathematische Abhandlungen*, volume 1. Julius Springer, Berlin, 1890.
- [45] A. H. Schoen. A Fifth Intersection-Free Infinite Periodic Minimal Surface of Cubic Symmetry. *Notices of the American Mathematical Society*, 16:519, 1969.
- A. H. Schoen. Infinite Periodic Minimal Surfaces without Self-Intersections. *NASA Technical Note TN D-5541*, 1970.

- [46] K. Ueno, K. Shiga, and S. Morita. *A Mathematical Gift: The Interplay Between Topology, Functions, Geometry, and Algebra*. American Mathematical Society, Providence, RI, 2003.
- [47] J. Hoshen and R. Kopelman. Percolation and cluster distribution. I. Cluster multiple labeling technique and critical concentration algorithm. *Physical Review B*, 14:3438, 1976.
- [48] A. Lipowski. Anomalous phase-ordering kinetics in the Ising model. *Physica A*, 268:6, 1999.
- [49] J. D. Shore, M. Holzer, and J. P. Sethna. Logarithmically slow domain growth in nonrandomly frustrated systems: Ising models with competing interactions. *Physical Review B*, 46:11376, 1992.
- [50] M. Plischke, Z. Racz, and D. Liu. Time-reversal invariance and universality of two-dimensional growth models. *Physical Review E*, 35:3485, 1987.
- [51] S. Redner. *A Guide to First-Passage Processes*. Cambridge University Press, New York, 2001.
- [52] N. Destainville (private communication).
- N. Destainville. Entropy and boundary conditions in random rhombus tilings. *Journal of Physics A*, 31:6123, 1998.
- V. Elser. Solution of the dimer problem on a hexagonal lattice with boundary. *Journal of Physics A*, 17:1509, 1984.
- [53] M. Hasenbusch and K. Pinn. Computing the roughening transition of Ising and solid-on-solid models by BCSOS model matching. *Journal of Physics A*, 30:63, 1997.
- [54] M. Ross. Schwarz' P and D surfaces are stable. *Differential Geometry and Its Applications*, 2:179, 1992.

- [55] C. M. Newman and D. L. Stein. Blocking and Persistence in the Zero-Temperature Dynamics of Homogeneous and Disordered Ising Models. *Physical Review Letters*, 82:3944, 1999.
- C. M. Newman and D. L. Stein. Zero-temperature dynamics of Ising spin systems following a deep quench: results and open problems. *Physica A*, 279:159, 2000.
- [56] P. Gambardella et. al. Ferromagnetism in one-dimensional monatomic metal chains. *Nature*, 416:301, 2002.
- A. Caneschi et. al. Glauber slow dynamics of the magnetization in a molecular Ising chain. *Europhysics Letters*, 58:771, 2002.
- A. Vindigni et. al. Fast switching of bistable magnetic nanowires through collective spin reversal. *Applied Physics Letters*, 87:073102, 2005.
- H. Miyasaka, M. Julve, M. Yamashita, and R. Clerac. Slow Dynamics of the Magnetization in One-Dimensional Coordination Polymers: Single-Chain Magnets. *Inorganic Chemistry*, 48:3420, 2009.
- [57] R. B. Potts. Some generalized order-disorder transformations. *Proceedings of the Cambridge Philosophical Society*, 48:106, 1952.
- [58] D. Raabe. Scaling Monte Carlo Kinetics of the Potts Model Using Rate Theory. *Acta Materialia*, 48:1617, 2000.
- Q. Yu, M. Nosonovsky, and S. K. Esche. On the accuracy of Monte Carlo Potts models for grain growth. *Journal of Computational Methods in Sciences and Engineering*, 8:227, 2008.
- D. Zollner. A Potts model for junction limited grain growth. *Computational Materials Science*, 50:2712, 2011.
- [59] J. A. Glazier, M. P. Anderson, and G. S. Grest. Coarsening in the two-dimensional soap froth and the large- $Q$  Potts model: A detailed comparison. *Philosophical Magazine B*, 62:615, 1990.

- G. L. Thomas, R. M. C. de Almeida, and F. Graner. Coarsening of three-dimensional grains in crystals, or bubbles in dry foams, tends towards a universal, statistically scale-invariant regime. *Physical Review E*, 74:021407, 2006.
- D. Weaire and N. Rivier. Soap, Cells and Statistics—Random Patterns in Two Dimensions. *Contemporary Physics*, 50(1):199, 2009.
- [60] J. C. M. Mombach, M. A. Z. Vasconcellos, and R. M. C. de Almeida. Arrangement of cells in vegetable tissues. *Journal of Physics D*, 23:600, 1990.
- [61] S. A. Safran, P. S. Sahni, and G. S. Grest. Kinetics of ordering in two dimensions. I. Model systems. *Physical Review B*, 28:2693, 1983.
- P. S. Sahni, D. J. Srolovitz, G. S. Grest, M. P. Anderson, and S. A. Safran. Kinetics of ordering in two dimensions. II. Quenched systems. *Physical Review B*, 28:2705, 1983.
- G. S. Grest, M. P. Anderson, and D. J. Srolovitz. Domain growth kinetics for the  $Q$ -state Potts model in two and three dimensions. *Physical Review B*, 38:4752, 1988.
- E. A. Holm, J. A. Glazier, D. J. Srolovitz, and G. S. Grest. Effects of lattice anisotropy and temperature on domain growth in the two-dimensional Potts model. *Physical Review A*, 43:2662, 1991.
- [62] M. E. J. Newman and R. M. Ziff. Efficient Monte Carlo Algorithm and High-Precision Results for Percolation. *Physical Review Letters*, 85:4104, 2000.
- [63] M. J. de Oliveira, A. Petri, and T. Tome. Glassy states in lattice models with many coexisting crystalline phases. *Europhysics Letters*, 65:20, 2004.
- [64] E. E. Ferrero and S. A. Cannas. Long-term ordering kinetics of the two-dimensional  $q$ -state Potts model. *Physical Review E*, 76:031108, 2007.
- [65] M. J. de Oliveira. Glassy states in the stochastic Potts model. *Computer Physics Communications*, 180:480, 2009.

- [66] J. Chalupa, P. L. Leath, and G. Reich. Bootstrap percolation on a Bethe lattice. *Journal of Physics C: Solid State Physics*, 12:L31, 1979.
- P. M. Kogut and P. L. Leath. High-density site percolation on real lattices. *Journal of Physics C*, 15:4225, 1982.
- J. Adler. Bootstrap percolation. *Physica A*, 171:453, 1991.
- [67] A. E. Holroyd. Sharp metastability threshold for two-dimensional bootstrap percolation. *Probability Theory and Related Fields*, 125:195, 2003.
- [68] R. K. P. Zia and D. J. Wallace. Critical behaviour of the continuous  $n$ -component Potts model. *Journal of Physics A*, 8:1495, 1975.
- [69] M. Lau, C. Dasgupta, and O. T. Valls. Domain growth in the field-theoretic version of the Potts model. *Physical Review B*, 38:9024, 1988.
- [70] L.-Q. Chen and W. Yang. Computer simulation of the domain dynamics of a quenched system with a large number of nonconserved order parameters: The grain-growth kinetics. *Physical Review B*, 50:15752, 1994.
- [71] D. Kandel and E. Domany. Rigorous Derivation of Domain Growth Kinetics without Conservation Laws. *Journal of Statistical Physics*, 58:685, 1990.
- [72] M. Barma. Dynamics of field-driven interfaces in the two-dimensional Ising model. *Journal of Physics A*, 25:L693, 1992.
- [73] P. L. Krapivsky. Limiting shapes of Ising droplets, Ising fingers, and Ising solitons. *Physical Review E*, 85:011152, 2012.
- [74] F. Spitzer. Interaction of Markov processes. *Advances in Mathematics*, 5:246, 1970.
- [75] T. Kriecherbauer and J. Krug. A pedestrian's view on interacting particle systems, KPZ universality and random matrices. *Journal of Physics A*, 43:403001, 2010.
- [76] P. L. Krapivsky. Dynamics of repulsion processes. *arXiv:1303.3641*.

- [77] H. Rost. Non-Equilibrium Behaviour of a Many-Particle Process: Density Profile and Local Equilibria. *Probability Theory and Related Fields*, 58:41, 1981.
- [78] T. Antal and G. M. Schutz. Asymmetric exclusion process with next-nearest-neighbor interaction: Some comments on traffic flow and a nonequilibrium reentrance transition. *Physical Review E*, 62:83, 2000.
- U. Basu and P. K. Mohanty. Active-absorbing-state phase transition beyond directed percolation: A class of exactly solvable models. *Physical Review E*, 79:041143, 2009.
- A. Gabel, P. L. Krapivsky, and S. Redner. Facilitated Asymmetric Exclusion. *Physical Review Letters*, 105:210603, 2010.
- [79] P. L. Krapivsky and J. Olejarz. Limiting shapes in two-dimensional Ising ferromagnets. *arXiv:1303.5128*.
- [80] I. Corwin. The Kardar-Parisi-Zhang Equation and Universality Class. *Random Matrices: Theory and Applications*, 1:1130001, 2012.
- [81] M. Tamm, S. Nechaev, and S. N. Majumdar. Statistics of layered zigzags: a two-dimensional generalization of TASEP. *Journal of Physics A*, 44:012002, 2011.
- [82] H. N. V. Temperley. Statistical mechanics and the partition of numbers. II. The form of crystal surfaces. *Proceedings of the Cambridge Philosophical Society*, 48:683, 1952.
- A. M. Vershik and S. V. Kerov. Asymptotics of maximal and typical dimensions of irreducible representations of a symmetric group. *Functional Analysis and Its Applications*, 19:21, 1985.
- J.-P. Marchand and Ph. A. Martin. Exclusion Process and Droplet Shape. *Journal of Statistical Physics*, 44:491, 1986.
- [83] R. Cerf and R. Kenyon. The Low-Temperature Expansion of the Wulff Crystal in the 3d Ising Model. *Communications in Mathematical Physics*, 222:147, 2001.

- A. Okounkov and N. Reshetikhin. Correlation function of Schur process with application to local geometry of a random 3-dimensional Young diagram. *Journal of the American Mathematical Society*, 16:581, 2003.
- [84] T. M. Liggett. *Interacting Particle Systems*. Springer, New York, 1985.
- H. Spohn. *Large Scale Dynamics of Interacting Particles*. Springer, Berlin, 1991.
- A. Karma and A. E. Lobkovsky. Low-temperature dynamics of kinks on Ising interfaces. *Physical Review E*, 71:036114, 2005.
- [85] J. Baik, P. Deift, and K. Johansson. On the distribution of the length of the longest increasing subsequence of random permutations. *Journal of the American Mathematical Society*, 12:1119, 1999.
- [86] K. Johansson. Shape Fluctuations and Random Matrices. *Communications in Mathematical Physics*, 209:437, 2000.
- [87] B. M. Forrest and L.-H. Tang. Surface Roughening in a Hypercube-Stacking Model. *Physical Review Letters*, 64:1405, 1990.
- B. M. Forrest and L.-H. Tang. Hypercube Stacking: A Potts-Spin Model for Surface Growth. *Journal of Statistical Physics*, 60:181, 1990.
- [88] M. Kardar, G. Parisi, and Y.-C. Zhang. Dynamic Scaling of Growing Interfaces. *Physical Review Letters*, 56:889, 1986.
- [89] T. Halpin-Healy and Y.-C. Zhang. Kinetic roughening phenomena, stochastic growth, directed polymers and all that. Aspects of multidisciplinary statistical mechanics. *Physics Reports*, 254:215, 1995.
- [90] J. Krug and P. Meakin. Universal finite-size effects in the rate of growth processes. *Journal of Physics A*, 23:L987, 1990.
- [91] F. D. A. Aarao Reis. Universality in two-dimensional Kardar-Parisi-Zhang growth. *Physical Review E*, 69:021610, 2004.



- [92] G. Odor, B. Liedke, and K.-H. Heinig. Mapping of (2+1)-dimensional Kardar-Parisi-Zhang growth onto a driven lattice gas model of dimers. *Physical Review E*, 79:021125, 2009.
- [93] B. Farnudi and D. D. Vvedensky. Large-scale simulations of ballistic deposition: The approach to asymptotic scaling. *Physical Review E*, 83:020103(R), 2011.
- [94] P. L. Ferrari and R. Frings. Finite Time Corrections in KPZ Growth Models. *Journal of Statistical Physics*, 144:1123, 2011.
- [95] J. M. Kim and J. M. Kosterlitz. Growth in a Restricted Solid-on-Solid Model. *Physical Review Letters*, 62:2289, 1989.
- [96] A.-L. Barabasi and H. E. Stanley. *Fractal Concepts in Surface Growth*. Cambridge University Press, New York, 1995.
- [97] J. Krug. Origins of scale invariance in growth processes. *Advances in Physics*, 46:139, 1997.
- [98] T. Halpin-Healy. (2+1)-Dimensional Directed Polymer in a Random Medium: Scaling Phenomena and Universal Distributions. *Physical Review Letters*, 109:170602, 2012.
- [99] P. L. Ferrari. Slow decorrelations in KPZ growth. *Journal of Statistical Mechanics*, page P07022, 2008.
- [100] I. Corwin, P. L. Ferrari, and S. Peche. Universality of slow decorrelation in KPZ growth. *Annales de l'Institut Henri Poincare*, 48:134, 2012.

# Curriculum Vitae

## Jason William Olejarz

### CONTACT INFORMATION

Physics Department  
Boston University  
590 Commonwealth Avenue  
Boston, Massachusetts 02215 USA  
jasonolejarz@gmail.com

### DATE AND PLACE OF BIRTH

April 27, 1986, New Bedford, MA

### EDUCATION

- Ph.D. in Physics, Boston University (2013)  
Advisor: Sidney Redner  
Thesis: *Domain Coarsening and Interface Kinetics in the Ising Model*
- M.A. in Physics, Boston University (2011)
- B.S. in Physics, University of Massachusetts at Dartmouth (2008)

### AWARDS

- Alvaro Rocco Memorial Award, Boston University (2012)

**PUBLICATIONS**

9. J. Olejarz and P. L. Krapivsky, arXiv:1306.4720 (submitted).
8. J. Olejarz, P. L. Krapivsky, and S. Redner, Journal of Statistical Mechanics (2013) P06018.
7. P. L. Krapivsky and J. Olejarz, Physical Review E **87**, 062111 (2013).
6. J. Olejarz, P. L. Krapivsky, S. Redner, and K. Mallick, Physical Review Letters **109**, 259602 (2012).
5. J. Olejarz, P. L. Krapivsky, and S. Redner, Physical Review Letters **109**, 195702 (2012).
4. J. Olejarz, P. L. Krapivsky, S. Redner, and K. Mallick, Physical Review Letters **108**, 016102 (2012).
3. J. Olejarz, P. L. Krapivsky, and S. Redner, Physical Review E **83**, 051104 (2011).
2. J. Olejarz, P. L. Krapivsky, and S. Redner, Physical Review E **83**, 030104 (2011).
1. D. Beesley, J. Olejarz, A. Tandon, and J. Marshall, Oceanography **21(2)**, 72 (2008).